SVEUČILIŠTE U ZAGREBU

PRIRODOSLOVNO-MATEMATIČKI FAKULTET
POSLIJEDIPLOMSKI STUDIJ PRIRODNIH ZNANOSTI
FIZIKA

Antonio Šiber

Teorija raspršenja termalnih atoma He na uređenim adsorbiranim strukturama niske gustoće

Doktorska teza

predložena Fizičkom odsjeku Prirodoslovno-matematičkog fakulteta Sveučilišta u Zagrebu radi stjecanja akademskog stupnja doktora prirodnih znanosti (fizika)

Zagreb, lipanj 2002.

UNIVERSITY OF ZAGREB

FACULTY OF NATURAL SCIENCES AND MATHEMATICS
POSTGRADUATE STUDY OF NATURAL SCIENCES
PHYSICS

Antonio Šiber

Theory of thermal energy He atom scattering from ordered submonolayers on solid surfaces

Doctoral Thesis

submitted to the Department of Physics,
Faculty of Natural Sciences & Mathematics, University of Zagreb,
for the academic degree of
Doctor of Natural Sciences (Physics)

Zagreb, june 2002

Acknowledgements

I wish to thank

- **Dr. Branko Gumhalter** for introducing me to the problem of atomsurface scattering and for numerous suggestions concerning the physics, language and the structure of this thesis.
- Prof. Dr. Christof Wöll for his hospitability during my visits to Ruhr Universität in Bochum where a part of this thesis has been written, for performing the potential calculation in subsection 6.3.2 and a number of comments concerning the He CO/Cu(001) scattering system.
- Marko T. Cvitaš for help with the log-derivative method and for providing relevant references concerning the method ([20, 21, 22, 23, 24, 106] and [107]).
- **Prof. Dr. Adolf Neckel** for providing reference [69], figure 6.10, and for a discussion on the electronic density contours of $c(2\times2)$ overlayer of Cl on Ag(001).
- **Dr. Dean Cvetko** for providing the experimental data in fig. 6.21 and a discussion on the experimental determination of bound states of the strongly corrugated interaction potentials in atom-surface scattering.
- **Dr. Gregor Witte** for discussions concerning the He-CO/Rh(111) scattering systems.
- **Prof. Dr. J. Peter Toennies** for comments concerning the He CO / Cu(001) scattering system and for bringing reference [87] to my attention.
- **Dr.** Christian Boas for a discussion on the drift spectra.
- **Dr. Davorin Lovrić** for a discussion concerning physisorption and chemisorption induced changes in atom-adsorbate interaction potential.

I also thank the personnel of the Institute of Physics in Zagreb for providing a good working environment. I was supported by the Croatian Ministry of Science and Technology through the funding for project 00350108.

Last, but not the least, I wish to thank my wife and my parents for supporting me during the period in which the ideas presented in this thesis have matured.

Contents

1	Intr	roduction	1			
2 Coupled channel equations approach to atom-st scattering						
	2.1	Time dependent and time independent approach to scat-				
		tering	6			
	2.2	Derivation of the scattering equations describing diffrac-	•			
		tion of atoms from surfaces	6			
	2.3	Numerical solution to the system of coupled channel	0			
		equations	9			
		2.3.1 Short description of the log-derivative method	9			
	2.4		11			
	2.5	Additional comments on the method of coupled channel				
		•	11			
		2.5.1 Coupled channel equations approach and pertur-				
			12			
	2.6	(1	13			
		2.6.1 Binary potential and pairwise additivity of the				
		potentials	13			
		2.6.2 Buckled surfaces	14			
3	Exp	perimental information on diffractive scattering of				
	the	rmal energy atoms from surfaces	۱9			
	3.1	Typical experimental setups	20			
	3.2	Selective adsorption or bound state resonances	21			
	3.3	Other information obtainable from the experimental data				
		<u>.</u>	23			
	3.4	Effects of incident energy spread and its inclusion in CC				
			26			

4	Mo	del po	tentials for atom-surface scattering	27							
	4.1	"True	\mathbb{P}^{2} potentials	28							
	4.2	The C	CLMTCD potential	28							
	4.3	Poisso	on sum formula and atom-surface potentials	30							
		4.3.1	Model potential for rectangular lattices	31							
		4.3.2	Model potential for HCP lattices	31							
		4.3.3	Honeycomb (graphite) structure	32							
		4.3.4	Other analytical representations of the V_{00} com-								
			ponent of the interaction potential	33							
		4.3.5	Other representations of surface corrugation	34							
5	Construction of realistic He-target potentials: The prob-										
			emisorbed adsorbates. Finite temperature ef-								
	fect		-	35							
	5.1	A "pr	oper" way of constructing the He-target potential .	36							
	5.2		ctive interaction	36							
		5.2.1	Physisorption and chemisorption induced								
			changes to the projectile - adsorbate attractive								
			interaction	37							
	5.3	Repul	sive interaction	42							
		5.3.1	Esbjerg and Nørskovs ansatz	42							
		5.3.2	Anticorrugation effects	43							
		5.3.3	Physisorption and chemisorption induced								
			changes in the projectile - adsorbate repulsive in-								
			teraction	43							
	5.4	A con	cept of pseudopotential	44							
	5.5										
		nents	of the interaction potential	44							
		5.5.1	Heuristic expressions for the effects of finite tem-								
			perature on the elastic scattering probabilities $% \left(1\right) =\left(1\right) +\left(1\right) +\left$	45							
6	Rea	al adso	orbate systems: Comparison of experimental	Į.							
	data with CC calculations 47										
	6.1	Xe/gr	$_{ m caphite}$	48							
		6.1.1	He-Xe gas phase potential	48							
		6.1.2	He-graphite potential	48							
		6.1.3									
			experimental results	49							
	6.2	$c(2 \times$	2)Cl/Ag(001)	55							
		6.2.1									
		·	action potential	56							

		6.2.2	Comparison of the results of CC calculations with				
			the experimental data	61			
		6.2.3	Playing with shapes: Extending the CLMT-CD				
			model from ellipses to "squares" and "stars"	63			
		6.2.4	Additional comments on the He-Cl pseudopotential	67			
	6.3	$c(2 \times$	2) CO/Cu(001)	67			
		6.3.1	He-CO gas phase potential	67			
		6.3.2	He-adsorbed CO potential	69			
		6.3.3	He-Cu(001) interaction potential	71			
		6.3.4	Comparison of the results of CC calculations with				
			experimental results	71			
		6.3.5	Additional information on the He - $c(2 \times 2)CO$ /				
			Cu(001) interaction potential	74			
		6.3.6	Test of the He-CO/Cu(001) potential in the case				
			of a dilute CO overlayer	77			
	6.4	$(\sqrt{3} \times$	$\sqrt{3}$)R30° CO/Rh(111)	83			
		$\hat{6}.4.1$		83			
		6.4.2	He-Rh(111) interaction potential	83			
		6.4.3	Comparison of the results of CC calculations with				
			the experimental results	85			
	6.5	$c(2 \times$	$2)3CO/Rh(111) \dots \dots \dots \dots \dots \dots$	87			
		6.5.1					
			experimental results	88			
		6.5.2	Sensitivity of CC calculations to the potential de-				
			tails in the cases of low and high coverage over-				
			layer structures	90			
	6.6	Addit	ional comments on the He - adsorbed CO potential.				
		Comp	arison with the various data from literature	92			
7	Sun	nmarv	and Conclusions	95			
•	Sull	iiiiiai y		00			
\mathbf{A}	A Notation						
В	Classical description of atom scattering from a rigid corrugated surface						
\mathbf{C}	Eigen-states wiht negative energy for the atoms ph-						
_	ysisorbed on a surface						

TEMELJNA DOKUMENTACIJSKA KARTICA

Sveučilište u Zagrebu Prirodoslovno-matematički fakultet Fizički odsjek

Doktorska disertacija

Teorija raspršenja termalnih atoma He na uredjenim strukturama niske gustoće

Antonio Šiber

Institut za fiziku, Zagreb

U radu se razmatra elastično raspršenje atoma He na uredjenim adsorbiranim strukturama niske gustoće. Sistemi od interesa su fizisorbirani i kemisorbirani uredjeni slojevi atoma i molekula na kristalnim površinama. Vrlo precizni potencijali interakcije projektila (He) sa ovim sistemima odredjeni su usporedbom teorijskih predvidjanja baziranih na metodi vezanih kanala i eksperimentalnih podataka.

(126 stranica, 41 slika, 108 literaturnih navoda, jezik izvornika: engleski)

Ključne riječi: raspršenje atoma na površinama, difrakcija, elastično i neelastično raspršenje, adsorpcija, monoslojevi, potencijali interakcije

Mentor: dr. Branko Gumhalter

Ocjenjivači: Rad prihvaćen:

BASIC DOCUMENTATION CARD

University of Zagreb Faculty of Natural Sciences and Mathematics Department of Physics

Doctoral Thesis

Theory of thermal energy He atom scattering from ordered submonolayers on solid surfaces

Antonio Šiber

Institut of physics, Zagreb, Croatia

In this thesis I consider the elastic scattering of He atoms from ordered (sub)monolayers on solid surfaces. The systems of interest are the physisorbed and chemisorbed ordered overlayers of atoms and moleculs on crystal surfaces. Very precise potentials of He atom interaction with these systems are determined by comparing the theoretical predictions based on the coupled channel method with the experimental data.

(126 pages, 41 figures, 108 references, original in English)

Keywords: scattering of atoms from surfaces, diffraction, elastic and inelastic scattering, adsorption, (sub)monolayers, interaction potentials

Supervisor: dr. Branko Gumhalter

Reviewers:

Thesis accepted:

Chapter 1

Introduction

The fact that atoms or molecules adsorb onto surfaces of metals, metal-oxides, insulators and other materials is of tremendous importance. In fact, it is even difficult to name all of the technological applications of the adsorption phenomena. Coating technologies, separation of polutants from the air or water, catalytic reactions, production of layered materials, molecular beam epitaxy - these are only few of the examples of technologies which encompass the phenomena of adsorption. Fertilizers, "clean" automobile exhaust systems, modern processors, data storage devices are some of the products which are very common and known to all, yet they were either created by or function thanks to the adsorption processes.

The motivation for the work described in this thesis is to contribute to the understanding of adsorption phenomena and the systems which consist of a substrate covered by ordered (sub)monolayers of adsorbate atoms or molecules. A very specific interest is the examination of such systems by utilizing the scattering of thermal energy atoms from surfaces. In particular, we are interested in the elastic, diffractive scattering of He atoms from such systems. The experimental and theoretical aspects of elastic and inelastic scattering of He atoms from surfaces have recently been reviewed in references [1] and [2].

Helium atom scattering (HAS ¹) has been known for a long time as a method of choice for surface characterisation due to its extreme surface sensitivity and its absolutely nondestructive nature. The potentials for He atom scattering from the various clean surfaces, both metalic and nonmetalic have been reported in the literature and summarized in reference [3], however the information on the potentials between the He atom and the systems consisting of (sub)monolayers of atoms and molecules adsorbed on ordered substrates is scarce. The properties of these potentials have been explored, but only in the highly repulsive region [1]. The attractive part of the potential has usually been neglected, except in the studies od physisorbed adsorbates (see article by H. Hoinkes and H. Wilsch in reference [4] for more details).

We shall show in this thesis that it is possible to construct reliable potentials pertinent to the systems of both weakly and strongly bound adsorbates and thereby gain additional insight in the properties of adsorbed atoms/molecules by comparing the results of theoretical descriptions of the scattering process with the existing experimental data.

Weakly bound, or physisorbed adsorbates are expected to remain to

¹The abbreviations and notational conventions are summarized in Appendix A.

INTRODUCTION 3

a large extent similar to the same species in the gas phase. The reason is that these adsorbates are bound to surfaces by the weak attractive van der Waals forces without significant change in their electronic structure. Such adsorbates interact with the projectile He atoms similarly as in the gas phase, so as that we can hope to be able to construct a very reliable He-target interaction potential without any kind of the electronic structure calculation, utilizing only the experimental data from the gas phase (crossed molecular beam) scattering experiments. These relatively simple systems are exemplified on the prototype system of adsorbed monolayer of Xe atoms on a graphite surface. The insight in the characteristics of the interactions we gain by this analysis can then be used in the studies of more complex systems.

There are adsorbates and substrates which form a strong chemical bond (we speak of *chemisorbed* adsorbates), resulting in the redistribution of charge both in the adsorbate and the substrate. The basic question in this case is whether one can conclude something about these redistributions by analysing the interaction of the projectile He atoms with such systems. We are also interested in the changes of the projectile-adsorbate long range interaction with respect to the corresponding interaction in the gas phase. These changes are expected and were roughly calculated in several theoretical investigations of the problem [5, 6]. One of our aims is to test these predictions. We shall present the results of our analyses for Cl atoms adsorbed on Ag(001) surface and CO molecules adsorbed on Cu and Rh surfaces. The system consisting of CO + O₂ molecules on Rh substrate has also a very large technological importance since it is used in automobile exhausts to oxidize CO to CO₂. Rh is also a metal of choice in various other catalitic reactions (as are also Fe, Co, Ni, Cu, Ru, Pd, Ag, Re, Os, Ir, Pt and Au and bimetalic combinations of these metals). The adsorption of CO on the various metals has been extensively studied with HAS both experimentally and theoretically [7]. Nevertheless, the precise information on the He-adsorbed CO potential is still lacking, although these systems have been the subject of many investigations. Due to this, very often the model or fitted potentials have been used. It is also one of the goals of this thesis to refine the knowledge on these potentials by exploiting the extraordinary sensitivity of the diffractive scattering to the details of the interaction potential. It will also be shown that some model potentials proposed earlier are very likely to be inappropriate.

The plan of this thesis is as follows:

In Chapter 2 we describe the method of coupled channel equations. We present a brief derivation of the method and its application to

scattering of atoms / molecules from surfaces, with the emphasis on diffractive scattering of atoms from ordered (sub)monolayers of adsorbed atoms/molecules.

In Chapter 3 we summarize the relevant experimental techniques which can provide information on the He-target interaction potential. We describe the phenomenon of selective adsorption (bound state) resonances and other resonant or interference structures that one can expect to affect the experimental data.

In Chapter 4 we propose a number of model potentials which should prove usefull in the case of surfaces that consist of atoms or molecules adsorbed on metallic or nonmetallic substrate material. The model potentials we propose here are particularly suited for use in CC calculations, since their Fourier components are analytical functions. This fact speeds up the CC calculations and enables the fitting of the potential.

In Chapter 5 we anticipate and discuss the problems which occur when applying the model potentials to the real adsorbate systems. We point to strong differences between the chemisorbed and physisorbed adsorbates. In particular, we discuss the changes induced in effective atom-adsorbate interactions due to the presence of the substrate and other adsorbates. In this chapter, we pinpoint the problems due to which the scattering from chemisorbed adsorbates has not been often discussed from the theoretical point of view.

In Chapter 6 we consider real adsorbate systems and analyse them by the methods developed in preceding chapters. We show how reliable potentials can be constructed for physisorbed and chemisorbed adsorbates. The extensive comparison between the theoretical predictions and experimental data is used for a precise determination of the interaction potentials.

Finally, in *Chapter* 7 we give a summary of the thesis and some prospects for future investigations.

Appendices contain additional relevant information not included in the main text.

Chapter 2

Coupled channel equations approach to atom-surface scattering

2.1 Time dependent and time independent approach to scattering

The scattering event is usually described in terms of particles (or, more generally, two subsystems) approaching to, interacting with and then separating from each other. The "products" of scattering can be either the same subsystems that were present before the interaction took place, in which case we speak of *inelastic* and *elastic* scattering, or the products can be different subsystems, in which case we speak of *reactive* scattering or reactions.

What is inherent to the above description is the concept of time. The scattering proceeds during finite time interval. However, we may think of scattering in a different way: We may imagine that the incident particles are fed into the scattering region (the region where the interactions take place), so that there is a constant influx and the same outflux of particles. This is a stationary situation, the particle density is constant in spatial and temporal coordinates, and we may only speak of a number of particles which end up in a particular segment of space or, equivalently, in a particular quantum number characterising the final state. Note here that these quantum numbers are not the quantum numbers characterising the entire hamiltonian but only the noninteracting part of the hamiltonian since in the region where the subsystems are formally infinitely separated (asymptotic region), there is no interaction between them. The concept of scattering time is not needed in this representation of scattering. This is the basic philosophy of the coupled channel approach to scattering.

That the two concepts are equivalent seems obvious, but the proof of this and the specification of the exact physical circumstances in which this is in fact true is far from simple. Here we only point to reference [16] where all these aspects have been discussed in detail.

2.2 Derivation of the scattering equations describing diffraction of atoms from surfaces

To describe the motion of a projectile atom of mass m and energy E that interacts with a target via a static potential, $V(\mathbf{r})$, one must solve

the Schrödinger equation:

$$\left[-\frac{\hbar^2}{2m} + V(\mathbf{r}) \right] \Psi(\mathbf{r}) = E\Psi(\mathbf{r}). \tag{2.1}$$

The physical origin of the interaction potential will be discussed later, but regardless of the nature of the potential $V(\mathbf{r})$, it must reflect the 2D surface periodicity and thus can be expanded in 2D Fourier series. The same holds for the wave function, $\Psi(\mathbf{r})$. Explicitly, we write the potential as ¹

$$V(\mathbf{r}) = \sum_{\mathbf{G}} V_{\mathbf{G}}(z)e^{i\mathbf{G}\cdot\mathbf{R}},$$
 (2.2)

and the wave function as

$$\Psi(\mathbf{r}) = \frac{1}{\sqrt{L_S^2 L_z}} \sum_{\mathbf{G}} \psi(\mathbf{K} + \mathbf{G}, k_z | z) e^{i(\mathbf{K} + \mathbf{G}) \cdot \mathbf{R}}.$$
 (2.3)

Substituting equations (2.2) and (2.3) into equation (2.1), we obtain the coupled channel equations

$$\left[\frac{d^2}{dz^2} + k_{\mathbf{G}z}^2\right] \psi(\mathbf{K} + \mathbf{G}, k_z | z)$$

$$- \frac{2m}{\hbar^2} \sum_{\mathbf{G}'} V_{\mathbf{G} - \mathbf{G}'}(z) \psi(\mathbf{K} + \mathbf{G}', k_z | z) = 0, \tag{2.4}$$

with

$$k_{\mathbf{G}z}^2 = k^2 - (\mathbf{K} + \mathbf{G})^2.$$
 (2.5)

We call the various final states of the projectile particle, characterized by $k_{\mathbf{G}z}^2$, the channels, or diffraction channels in this case. The channels for which $k_{\mathbf{G}z}^2 > 0$ ($k_{\mathbf{G}z}^2 < 0$) are called open (closed) channels.

There is an infinite number of solutions to the set of equations (2.4). However, we are interested in only one set of solutions, and this one should fulfill the scattering asymptotic boundary conditions (for $z \to \infty$) given by

$$\psi(\mathbf{K} + \mathbf{G}, k_z) \rightarrow \frac{1}{\sqrt{k_z}} e^{-ik_z z} \delta_{\mathbf{G}, 0} + \frac{1}{\sqrt{k_{\mathbf{G}z}}} S_{\mathbf{G}, 0} e^{+ik_{\mathbf{G}z}z}, \quad k_{\mathbf{G}z}^2 > 0$$

$$\psi(\mathbf{K} + \mathbf{G}, k_z) \rightarrow 0, \quad k_{\mathbf{G}z}^2 < 0 \tag{2.6}$$

These conditions are equivalent to the statement that the open channels should reduce to plane waves far from the surface, while the projectile

¹Note that here we restrict ourselves to the study of ordered structures only.

particle cannot be in closed channels in the region of large z-coordinate. The asymptotic conditions implicitly embody the concept of time. In particular, they account for the fact that the interaction vanishes at $t \to -\infty$ (before the scattering) and at $t \to \infty$ (after the scattering). All the incoming particles must come out of the surface. This unitarity statement can be represented as

$$\sum_{\mathbf{G}, k_{\mathbf{G}z}^2 > 0} |S_{\mathbf{G}, 0}|^2 = 1, \tag{2.7}$$

where the meaning of coefficients $S_{\mathbf{G},0}$, with the normalization of wavefunction as in equation (2.6), is

$$|S_{\mathbf{G},0}|^2 = \frac{\text{outgoing flux in channel } k_{\mathbf{Gz}} \text{ (or } \mathbf{G})}{\text{incomming flux (in channel } k_{\mathbf{z}} \text{ (or } \mathbf{G} = 0))},$$
 (2.8)

i.e. $S_{\mathbf{G},\mathbf{G}'}$ is the complete S-matrix for the diffractive scattering. As we are interested only in the case where the incident particle is in specified, open channel, initial state $|k_z\rangle$, of the whole S-matrix we need only one of its columns, $S_{\mathbf{G},0}$.

One might wonder about how the sticking processes, in which the projectile particle remains stuck to the surface after the interaction, are treated in this formalism. For projectiles which scatter elastically, the total energy must be conserved and although the z-component of energy may be negative, the total energy is positive. This means that the "stuck" particles travel parallel to the surface with a velocity higher than the one they had initially. In a finite time, these stuck particles diffract again and in such a way that their component of energy in z-direction becomes positive, i.e. they diffract in an open scattering channel and eventually separate from the surface. This argument is also valid for inelastic scattering from systems of finite dimensions. Assume for example that the projectile excites a quantum of surface vibration (phonon), so that its total energy is smaller than the initial energy and that the projectile sticks to the surface (or giant molecule). In systems of finite dimensions and isolated from its surrounding, the quantum of energy lost by the projectile remains in the system i.e. the total energy of the whole system is conserved. In a finite time period (which, however, may be too long for experimentalists to measure), the energy of the whole system will redistribute in such a way that the stuck projectile will have enough energy to leave the surface and eventually separate from it. For systems of infinite dimensions, the "lost" quantum of energy will never localize in the region of space occupied by the stuck projectile (see also discussion in reference [14]).

2.3 Numerical solution to the system of coupled channel equations

There are many ways to solve the systems of coupled linear differential equations. The numerical methods are still improving as a result of the need for precise calculations in the physical situations where many scattering channels are involved. Somewhat outdated but very instructive review of coupled channel approach to collisions in the gas phase is given in [17]. The equations one obtains for the gas phase scattering problem are essentially the same as for the case of diffractive scattering from surfaces, only the definition of the channels changes and the asymptotic solutions have different functional form. In reference [17] one can also find a review of the early numerical approaches to the solution of cc equations such as the Numerov method, the de Vogelaere method, the coupled channel R-matrix method, the method of piecewise analytic solutions and the variable phase method. Some of these early methods have inherent drawbacks, usually associated with the fact that the numerical propagation of deeply burried channels tends to be unstable as the propagation coordinate increases. For example, using the method of piecewise analytic solutions developed by R.G. Gordon [18, 19], one has to perform the so called stabilizing transformations in each step of the propagation coordinate. These are matrix transformations which usually cost a lot of computer CPU time. For our purposes, we have adopted a relatively recent, the so called log-derivative method.

2.3.1 Short description of the log-derivative method

The log-derivative method was introduced by Johnson [20, 21] and later rederived by Mrugala and Secrest [22] and by Manolopoulos et al [23].

The cc equations in equation (2.4) can be cast into matrix form as

$$\overline{\Psi}''(z) = \overline{W}(z)\overline{\Psi}(z), \tag{2.9}$$

where the matrix $\overline{W}(z)$ in the case of diffractive scattering of atoms from surfaces is given by

$$\overline{W}(z)_{\mathbf{G},\mathbf{G}'} = \frac{2m}{\hbar^2} V_{\mathbf{G}-\mathbf{G}'}(z) - k_{\mathbf{G}z}^2 \delta_{\mathbf{G},\mathbf{G}'}.$$
 (2.10)

The wavefunction is also a matrix, $\overline{\Psi}(z)$, and not a vector. This is due to the fact that we must propagate N wavefunctions, where N

is the number of elements in the CC basis, all with different initial conditions which represent N linearly independent solutions, the linear combination of which satisfies the asymptotic boundary conditions in equation (2.6).

The basic idea of the method is not to propagate the wave function matrix itself but rather a combination of a wave function matrix and a derivative wave function matrix, i.e. to propagate the matrix $\overline{Y}(z)$ given by

$$\overline{\Psi}'(z) = \overline{Y}(z)\overline{\Psi}(z). \tag{2.11}$$

The equations we actually solve are

$$\overline{Y}'(z) = \overline{W}(z) - \overline{Y}^{2}(z). \tag{2.12}$$

This equation is known as the matrix Riccati equation.

It should be noted that the elements of log-derivative matrix, $\overline{Y}(z)$, corresponding to closed channel solutions are well behaved and can not cause numerical underflow problems since for closed channels $\psi(z) \sim \exp(-\zeta z)$ and $\psi'(z)/\psi(z) \sim -\zeta$. The \overline{Y} -matrix is singular in all the points where the wave function has a node. However, this is of no importance for the numerical implementation of the log-derivative method because the probability to encounter one point from this discrete set of points sampled in the numerical application of the method is zero. The probability for the numerical overflow might be different from zero, but this is extremely unlikely in practice (see [24] for a more detailed discussion).

The numerical evaluation of eq. (2.12) consists in propagation of the \overline{Y} -matrix from the beginning of a small interval in z coordinate to the end of the interval. When the interval is in the asymptotic region, we stop the propagation and construct the asymptotic wave function vector from the propagated wave function matrix. This procedure also produces the S-matrix (eq. (2.6)). To obtain converged results, the integration of equation (2.12) must be started deeply in the clasically forbidden region of the interaction potential, at the value of coordinate z equal to some predetermined z_0 . The initial conditions we impose on the Y-matrix are

$$\overline{Y}(z_0) = \infty \overline{I}, \tag{2.13}$$

where \overline{I} is the unit matrix. Physically, this boundary condition is equivalent to assuming that the interaction potential is infinitely repulsive in the region $(-\infty, z_0)$, so that $\overline{\Psi}(z_0) = 0$. In practice the infinity in equation (2.13) is replaced by a finite large number (10¹⁵ in our implementation).

The description of how to actually propagate the \overline{Y} -matrix from the beginning to the end of the interval is beyond the scope of this thesis. All the details related to the numerical implementation of the log-derivative method are described in ref. [24]. In short, the log-derivative propagator we use is the same as in the original Johnson's approach [20].

2.4 Choice of the basis for numerical calculations

In order to get the converged results, one must choose large enough basis of G vectors which are of importance for a particular scattering event. The "best way" to do this is by no means obvious. Large bases imply slow calculations and small bases might not yield converged results.

The criterion we choose is the following: Each \mathbf{G} vector can be represented as $\mathbf{G} = m\mathbf{g}_1 + n\mathbf{g}_2$ where \mathbf{g}_1 and \mathbf{g}_2 are the basis vectors in the inverse space. We include in our basis all the \mathbf{G} vectors such that $|m| \leq n_{max}$ and $|n| \leq n_{max}$, where n_{max} is a predetermined positive integer. The thus constructed basis contains a lot of closed scattering channels, some of which are deeply burried and which are not expected to be of importance to the description of a diffractive scattering event. Therefore, we additionally reduce the basis by excluding all the channels for which $\frac{\hbar^2}{2m}k_{\mathbf{G}z}^2 \leq E_{min}$, where E_{min} is some predetermined and negative energy.

This is similar (although not the same) to the choice made in reference [52].

2.5 Additional comments on the method of coupled channel equations

The CC method yields an exact solution to the Schrödinger equation. The solution of CC equations can be arbitrarily close to the exact solution if the CC basis is sufficiently large. However, the problems occur when the number of possible channels is large. For example, in the scattering of molecules from surfaces, in the CC basis one should include channels corresponding to rotational excitations of the molecule, vibrational excitations of the molecule, diffractive transitions and excitations of phonons in the target. It is obvious that this would produce \overline{W} and \overline{Y} matrices of enormous dimensions, even if we knew how to deal

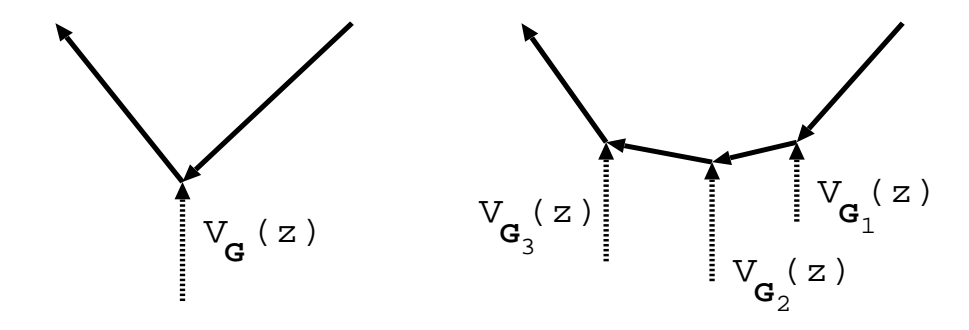


Figure 2.1: Left: First order Feynman diagram for 0-**G** transition. Right: Third order Feynman diagram for 0-**G** transition.

with the inclusion of target phonons in the formalism which is a complex matter *per se*, since the quantum numbers representing phonons in the (semi) infinite sample are continous variables (see e.g. references [25, 26]).

The \overline{W} and \overline{Y} matrices can also be huge if the basis functions we choose poorly reflect the symmetry of the problem. Then we need a large number of channels to obtain converged results (see subsection 6.3.6).

2.5.1 Coupled channel equations approach and perturbation theory

The earliest attempts to solve the problem of diffraction of thermal energy atoms from surfaces were based on perturbative approach [8] (see also review articles [1] and [2]). The assumption is that $V_{00}(z)$ is the most dominant component of the interaction. Other components, $V_{\mathbf{G}}(z)$, for $\mathbf{G} \neq 0$ are then treated as a small perturbation. The lowest order diagram describing the diffraction process in this approach is presented on the left hand side of figure 2.1. The transition probability is proportional to the matrix element $|<\mathbf{K}_i + \mathbf{G}|V_{\mathbf{G}}(z)|\mathbf{K}_i>|^2$, where the wave functions $|\mathbf{K}_i + \mathbf{G}| > 1$ are the solutions to the Schrödinger equation with only the $V_{00}(z)$ part included in the hamiltonian.

While this approach might work for surfaces with low corrugation (such as metal surfaces with low Miller indices), it is completely inapplicable to the surfaces with high corrugation which are of interest to us in this thesis. For example, the diagram on the right hand side of figure 2.1 also contributes to the 0-**G** transition if $\mathbf{G}_1 + \mathbf{G}_2 + \mathbf{G}_3 = \mathbf{G}$. Higher order diagrams become more important as the corrugation related components of the interaction potential grow in magnitude, and

the simplest perturbation theory approach becomes inappropriate.

2.6 \overline{W} (potential) matrix

What is needed in a calculation of the \overline{W} matrix is the set of Fourier components of the interaction potential, i.e.

$$V_{\mathbf{G}}(z) = \frac{1}{L_S^2} \int d^2 R e^{-i\mathbf{G} \cdot \mathbf{R}} V(\mathbf{r}), \qquad (2.14)$$

where L_S^2 is the total area of the surface of the sample. Since the above equation holds also for $\mathbf{G} = 0$, we see that $V_{00}(z)$ is nothing but an average of the interaction potential over the surface plane of the sample.

2.6.1 Binary potential and pairwise additivity of the potentials

When the total interaction potential can be written as a superposition of pair potentials,

$$V(\mathbf{r}) = \sum_{j} v(||\mathbf{r} - \mathbf{r}_{j}|), \qquad (2.15)$$

where j counts the crystal sites of the target, relation (2.14) additionally simplifies according to

$$V_{\mathbf{G}}(z) = \frac{1}{L_S^2} \int d^2R e^{-i\mathbf{G}\cdot\mathbf{R}} \sum_j v(\mathbf{r} - \mathbf{r}_j)$$

$$= \frac{1}{L_S^2} \sum_{l,\kappa} \int d^2R e^{-i\mathbf{G}\cdot\mathbf{R}} v(\mathbf{r} - \mathbf{r}_{l,\kappa})$$

$$= \frac{1}{L_S^2} \sum_{l,\kappa} \int d^2R e^{-i\mathbf{G}\cdot\mathbf{R}} v(\mathbf{R} - \mathbf{R}_l + z\mathbf{z}_0 - \mathbf{S}_\kappa). \quad (2.16)$$

Here, the index j was replaced by two indices (l,κ) which count the atoms within the crystal plane and the crystal planes themselves, respectively. The vector \mathbf{S}_{κ} connects the centers of the two-dimensional Wigner-Seitz cells in the topmost crystal plane $(\kappa=0)$ and the crystal plane κ . \mathbf{z}_0 is the unit vector pointing in the z-direction. Assuming that the pair potential v does not depend on the angle in the surface plane, ϕ , equation (2.16) simplifies to

$$V_{\mathbf{G}}(z) = \frac{2\pi}{A_c} \sum_{\kappa} e^{i\mathbf{G} \cdot \mathbf{S}_{\kappa}} \int_0^{\infty} R J_0(|\mathbf{G}|R) v\left(\sqrt{R^2 + (z - (\mathbf{S}_{\kappa} \cdot \mathbf{z}_0))^2}\right) dR,$$
(2.17)

where we have used the integral representation of the zeroth order Bessel function J_0 ,

$$J_0(w) = \frac{1}{\pi} \int_0^{\pi} \cos(w \cos \phi) d\phi,$$
 (2.18)

and 2

$$\sum_{l} \exp(-i\mathbf{H} \cdot \mathbf{R}_{l}) = N_{2D} \delta_{\mathbf{H},\mathbf{G}}.$$
 (2.19)

 A_c is the area of the two dimensional (2D) Wigner-Seitz cell of the target given by

$$A_c = \frac{L_S^2}{N_{2D}},\tag{2.20}$$

where N_{2D} is the number of 2D Wigner-Seitz cells in each crystal plane, κ . Note also that $\mathbf{S}_{\kappa} \cdot \mathbf{z}_0 < 0$.

The above equations were derived for surfaces which have one atom per surface unit cell. The generalization to surfaces with more than one atom per unit cell is straightforward. The formula for the potential Fourier components in this case is ³

$$V_{\mathbf{G}}(z) = \frac{2\pi}{A_c} \sum_{v} e^{-i\mathbf{G} \cdot \mathbf{R}_v} \int_0^\infty R J_0(|\mathbf{G}|R) v_v \left(\sqrt{R^2 + (z - z_v)^2}\right) dR,$$
(2.21)

where index v counts (possibly) different atoms within a surface unit cell. \mathbf{R}_v is the radius vector of v-th atom within a surface unit cell measured from the origin within a particular unit cell. z_v is the z-coordinate of the v-th atom.

2.6.2 Buckled surfaces

Overlayers of atoms or molecules deposited on a substrate can sometimes have complex geometry which cannot be described easily with a set of unit vectors in the direct space. One of the phenomena which can occur is the so called buckling of the overlayer (see e.g. reference [27]). The buckled surfaces have two characteristic periodicities: One is related to the lattice constant periodicity and the other is the periodicity of the height modulation 4 (see fig. 2.2). In what follows, we

²Here **H** is an arbitrary 2D vector within a surface plane and **G** is a reciprocal 2D vector of a structure in question.

³For simplicity we consider here only the topmost layer of atoms.

⁴Here we study only the height modulation, although one could imagine the density, i.e. in-plane type of modulation. The formulas for this case can be easily derived following the same procedure as described below.

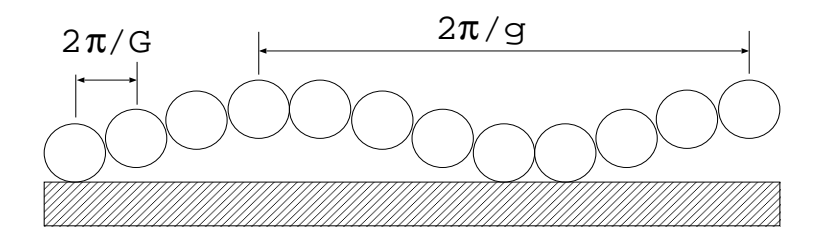


Figure 2.2: Buckled surface in 1D.

shall show how such surfaces can be treated in the close coupled diffraction calculations, in particular, we shall derive the expressions for the Fourier components of the projectile-target interaction potential.

Assuming that the total potential can be written as a superposition of the projectile-adsorbate potentials, we can write for the total potential

$$V(\mathbf{r}) = \sum_{l} v(\mathbf{r} - \mathbf{r}_{l}) = \sum_{l} v(\mathbf{r} - \mathbf{r}_{l}^{0} + z_{l}), \qquad (2.22)$$

where z_l represents the deviation of height of the l-th adsorbate site from its "unbuckled" position. The constant height of the "unbuckled" positions, \mathbf{r}_l^0 is arbitrary but it will prove fruitfull to define it in such a way that the z_l deviates symmetrically in positive and negative direction. Assuming now that the z_l deviations are small with respect to $\mathbf{r} - \mathbf{r}_l^0$, we can write for the potential

$$V(\mathbf{r}) = \sum_{l} v(\mathbf{r} - \mathbf{r}_{l}^{0}) + \sum_{l} \frac{\partial v(\mathbf{r} - \mathbf{r}_{l}^{0})}{\partial z} z_{l}.$$
 (2.23)

In the following, we shall restrict our attention to ordered (sub)monolayer films on smooth substrates i.e. we shall consider only the zeroth Fourier component of interaction of the projectile with the substrate. This is a good assumption even for the substrates with rather corrugated electronic densities due to the fact that the closest approach of the projectile to the substrate is restricted by the presence of the adlayer. The Fourier components of the potential in equation (2.23) are given by

$$V_{\mathbf{H}}(z) = \frac{1}{L_S^2} \int d^2 R \exp(-i\mathbf{H} \cdot \mathbf{R}) V(\mathbf{r}). \tag{2.24}$$

The first part of the sum in equation (2.23) produces Fourier components typical of ordered monolayers which are unbuckled, i.e.

$$V_{\mathbf{H}}(z)^{(1)} = \sum_{\mathbf{G}} \frac{2\pi}{A_c} \int dR R J_0(|\mathbf{H}|R) v(\sqrt{(R-R^0)^2 + (z-z^0)^2}) \delta_{\mathbf{H},\mathbf{G}}$$

$$+ V_{subs}(z)\delta_{\mathbf{H},0}. \tag{2.25}$$

Here **G** is the reciprocal vector of the lattice of the unbuckled (projected in 2D) monolayer. We have also explicitly included the interaction of the projectile with the uncorrugated substrate, $V_{subs}(z)$. For the second part, we write

$$V_{\mathbf{H}}(z)^{(2)} = \frac{1}{L_S^2} \int d^2 R \exp(-i\mathbf{H} \cdot \mathbf{R}) \sum_{l} \frac{\partial v(\mathbf{r} - \mathbf{r}_l^0)}{\partial z} z_l.$$
 (2.26)

The height modulation can be written as a Fourier series,

$$z_l = z(\mathbf{R}_l) = \sum_{\mathbf{g}} z_{\mathbf{g}} \exp(i\mathbf{g} \cdot \mathbf{R}_l).$$
 (2.27)

Inserting this into (2.26), we have

$$V_{\mathbf{H}}(z)^{(2)} = \frac{2\pi}{A_c} \sum_{\mathbf{g}} z_{\mathbf{g}} \delta_{\mathbf{G}+\mathbf{g},\mathbf{H}}$$

$$\times \int dR R J_0(|\mathbf{H}|R) \frac{\partial v(\sqrt{(R-R^0)^2 + (z-z^0)^2})}{\partial z} (2.28)$$

Finally, for the Fourier components of the total potential we write

$$V_{\mathbf{H}}(z) = V_{\mathbf{H}}(z)^{(1)} + V_{\mathbf{H}}(z)^{(2)}.$$
 (2.29)

Note that the channels available for diffraction are the channels supported by the unbuckled surface (**G**) and the "satelite" channels (**G** + **g**). If we choose \mathbf{r}_l^0 in such a way that $z_{\mathbf{g}=0} = 0$, then the modulation related features will appear only in the satelite channels (see eq.(2.28)) and will influence the channels of the unbuckled surface only through the total flux conservation requirement.

For typical buckling profiles it should be sufficient to take only the lowest order **g** components i.e. to represent the buckling profile as a superposition of two cosine functions in two perpendicular directions, with possibly different periodicities.

One might wonder whether the procedure described above can be used for the description of diffractive scattering of atoms from stepped surfaces. In this case, the amplitudes of the height modulation are of the order of interatomic spacings and also of the order of the classical turning point of the projectile atom. Thus, equation (2.23) will not be valid in this case.

It is of interest to see how the buckling of the surface influences the diffractive scattering of atoms. Some insight can be obtained without

a detailed calculation. Due to the fact that the number of channels is larger in the case of a buckled surface, we might expect that some of the intensity that would otherwise go into the unbuckled surface diffractive channels will now go into the satellite channels. Thus, the total intensity present in the ${\bf G}$ channels will be less than 1. It should in principle be possible to determine buckling amplitudes by comparing the CC calculations with extensive experimental data. Such experimental data have not been made available so far.

Chapter 3

Experimental information on diffractive scattering of thermal energy atoms from surfaces

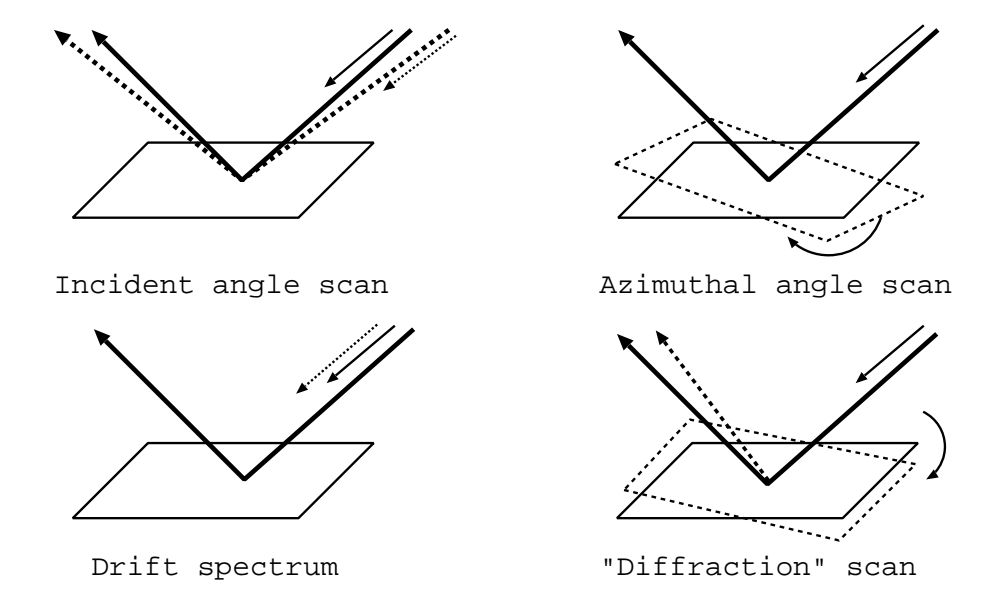


Figure 3.1: Experimental arrangements to study diffraction of the projectile atoms from surfaces. Short arrows represent the projectile incident wavevector.

3.1 Typical experimental setups

There are essentially four types of experiments which may be performed to obtain the desired information on the diffraction of projectile particles from the target. These four types are sketched in figure 3.1.

The incident angle scan is based on changing both the incident angle and the final angle of scattering (with respect to z axis) so that $\theta_i = \theta_f$. In this way, one follows the specularly scattered beam and measures its intensity, I_{00} , as a function of θ_i . Since both the incident and final angles must change, this type of measurement requires an experimental setup where the source and the detector arm of the instrument can not be fixed (see e.g. reference [12]).

The azimuthal angle scan is performed by rotating the target sample within the plane of its surface and recording the changes in the specularly scattered intensity. This type of experiment can be performed with the source and detector arms fixed.

The *drift spectra* are obtained by changing the incident energy of the projectile (i.e. by changing the nozzle temperature [12]) and recording the changes of the specularly scattered intensity. This type of experiment can be also performed with the source and detector arms fixed.

And finally, the measurements which are most often performed with

the modern HAS machines, which were primarily designed for the TOF (inelastic) measurements and have fixed geometry, produce the so called "diffraction" spectra. To obtain these spectra one rotates the sample so as to change the incident angle with respect to the z axis, keeping the azimuthal angle constant, and recording the intensities of diffraction peaks which enter the detector (zeroth order intensity is recorded for $\theta_i = \theta_f$).

All of the described experimental setups have their advantages and drawbacks. For example, when one performs the incident angle scans, the change of perpendicular "component" of the incident energy causes the change of the degree of inelasticity of scattering. For systems with low corrugation [2] this means that the inelastically scattered intensity increases as the incident angle decreases. Due to the unitarity (i.e. total intensity conservation) of the scattering, this means that less intensity is scattered into the elastic channels. Additionally, if the cross section of the beam is larger than the sample area, as the incident angle increases the number of projectiles that actually hit the target diminishes. A simple geometrical consideration shows that the effective incident intensity, I_{in}^{eff} , scales with the incident angle θ_i as $I_{in}^{eff} = I_{in} d \cos \theta_i/D$, where I_{in} is the total incident intensity, d is the area of the target sample and D is the area of the cross section of the beam.

Similarly, for drift scans, since one changes the incident energy, for higher incident energies there will be more projectiles scattered inelastically, i.e. a smaller number will end up in the diffractive channels. The information produced by the "diffraction" scans in usually not adequate for detailed conclusions about the interaction potential. The problems related to inelastic scattering effects persist also in this case. Azimuthal scans do seem to be the best choice for diffractive scattering investigations. There are, however, problems related to a precise determination of the azimuthal angle, especially in the modern TOF HAS machines [15] which were not designed primarily for this use.

3.2 Selective adsorption or bound state resonances

The most interesting information, concerning the precise determination of the interaction potential that one can obtain from the experiments is related to the appearance of *selective adsorption* or *bound* state resonances. This phenomenon takes place when the projectile atom diffracts from the surface in such a way that its energy in the z-direction coincides with a bound state of the interaction potential. Explicitly,

$$E_i = \frac{\hbar^2 (\mathbf{K}_i + \mathbf{G})^2}{2m} + \epsilon_n, \tag{3.1}$$

where $\epsilon_n < 0$ is the energy of a bound state of the interaction potential. Experimentally, these phenomena produce distinct features in the spectra. Usually, one detects a sudden drop in the specularly scattered intensity when the condition for appearance of a selective adsorption resonance is fullfilled ¹. Of course, the correct assignment of the resonance features detected experimentally leads directly to the bound states of the interaction potential which is an information of extreme usefullness for the determination of the potential itself. Unfortunatelly, the situation is not as simple when one deals with strongly corrugated systems which are of interest to us.

For strongly corrugated systems, the bound state energies are not simple numbers but functions of the projectile parallel wave vector. This is due to the fact that the interaction potential is not flat in the directions parallel to the surface (i.e. its higher Fourier components are not vanishingly small), and the states it supports are not given as free particle bands as in equation (3.1). More generally, the selective adsorption criterion should be written as ²

$$E_i = \frac{\hbar^2 (\mathbf{K}_i + \mathbf{G})^2}{2m} + \epsilon_n (\mathbf{K}_i + \mathbf{G}). \tag{3.2}$$

The interpretation of selective adsorption resonances is very complicated in the case of strongly corrugated systems. The position of resonances is influenced by the bound states of the $V_{00}(z)$ component of the potential and by the corrugation of the potential, i.e. by $V_{\mathbf{G}}(z)$, $\mathbf{G} \neq 0$ components of the potential. However, one can hope that the free-particle resonance criterion is approximatelly satisfied and that the influence of corrugation on the resonances is a secondary effect.

¹Sometimes, the bound state resonance phenomena reflect themselves as maxima in the experimental spectra. This will be discussed later.

²The calculation of the bound states of atom adsorbed on corrugated surface is presented in appendix C.

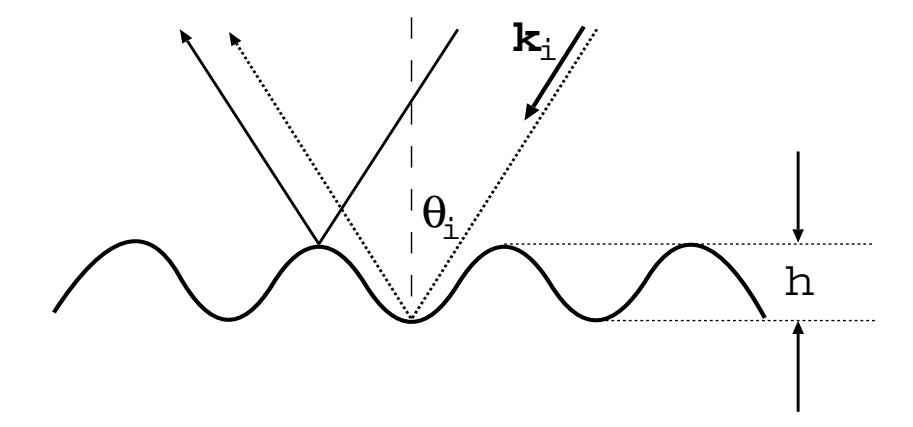


Figure 3.2: A sketch of a corrugation induced interference phenomenon in 1D.

3.3 Other information obtainable from the experimental data on diffractive scattering

In addition to selective adsorption resonances, there are other phenomena that can be seen in the experiments which may be of use for a construction of the interaction potential. Figure 3.2 displays a sketch of a phenomenon that one can expect to take place in the strongly corrugated systems.

Due to strong corrugation of the potential, the projectiles following the full and the dotted path enter the detector with different phases. The interference between the two trajectories causes the oscillations in the specularly scattered intensity. It can be easily shown that the intensity oscillations follow the relation

$$I_{env} \sim 1 + \cos \left[\frac{2h}{\cos \theta_i} \sqrt{\frac{2m(E_i + \overline{D})}{\hbar^2}} \right],$$
 (3.3)

where h is the corrugation amplitude in the direction of specular scattering. The parameter \overline{D} was introduced in this equation to simulate the fact that the difference in phase was accumulated in the region of the attractive potential. For typical ranges of the atom-surface interactions and typical projectile energies, the distance between the classical turning point and the potential minimum is ~ 0.7 Å. Thus, for highly corrugated systems, say $h \sim 1$ Å, a difference in phase is accumulated between the classical turning point and the inflection point of the po-

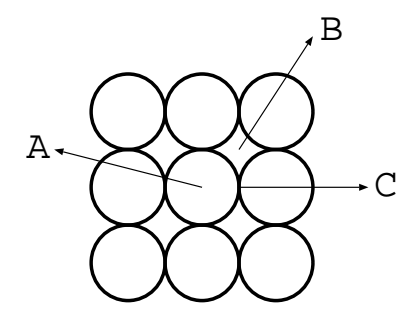


Figure 3.3: A sketch of a corrugation induced interference phenomenon in 2D.

tential. Of course, the potential in this region is not uniform and equal to $-\overline{D}$, so that we can expect that our estimate of \overline{D} should be smaller than the actual depth of the potential well in this region. On the other hand, the region where the phase difference accumulates is the region where the potential is more attractive than the $V_{00}(z)$ component, so the well depth actually seen by the projectile is larger than the well depth of the $V_{00}(z)$ component of the potential. The partial cancelation of these two effects should make the optimum parameter $-\overline{D}$ to be a reasonable estimate of the well depth of the $V_{00}(z)$ component of the interaction potential.

The above decribed effect has been used in HAS to determine the quantities as step heights, island heights and such [81], but we shall show that it plays a significant role for strongly corrugated systems as well. This effect appears in the incident angle scans and in the drift spectra as a clear modulation (envelope) of the specularly scattered intensity.

A simple analysis of this phenomenon has been given in 1D but for realistic surfaces with 2D corrugation the phenomenon is more complex since there are more than two points where the corrugation profile has an extremum. Let us examine qualitatively this case as well.

In figure 3.3 we show the three characteristic points in the direct space where the corrugation profile has extrema. It is easy to show that the superposition of beams scattered specularly from these three points results in the intensity envelope given as

$$I_{env} \sim 3 + 2 \left[\cos \frac{s_1 + s_2}{2} \cos \frac{s_1 + s_2}{2} + \cos(s_1) \cos(s_2) + \sin(s_1) \sin(s_2) \right],$$
 (3.4)

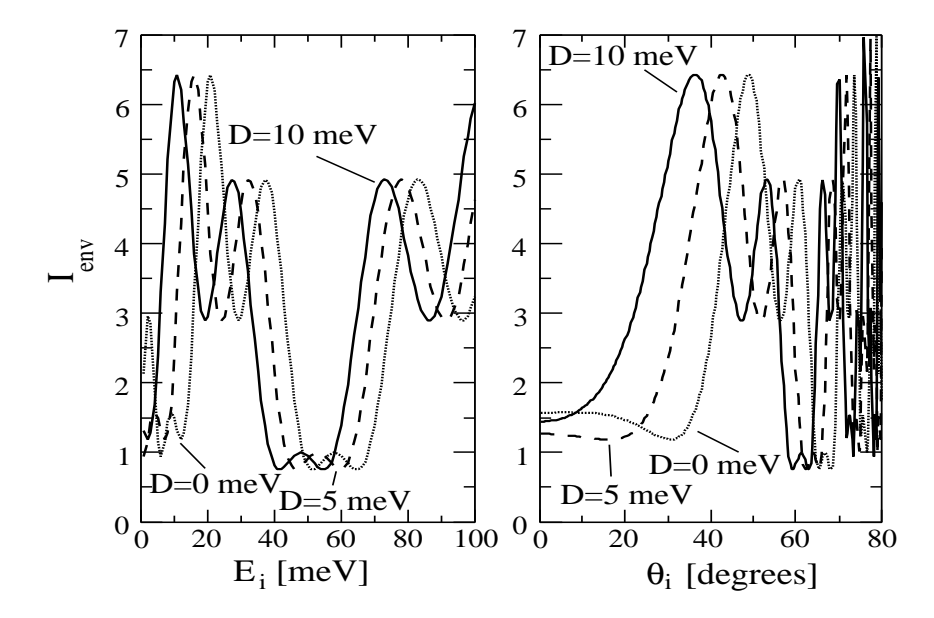


Figure 3.4: I_{env} from eq. (3.4) as a function of incident energy (left panel, $\theta_i = 47.9^{\circ}$) and incident angle (right panel, $E_i = 20 \text{ meV}$). The parameters are $h_1 = 1 \text{ Å}$, $h_2 = 0.7 \text{ Å}$ and m = 4 amu

where

$$s_1 = \frac{2h_1}{\cos \theta_i} \sqrt{\frac{2m(E_i + D)}{\hbar^2}}$$

$$s_2 = \frac{2h_2}{\cos \theta_i} \sqrt{\frac{2m(E_i + D)}{\hbar^2}}.$$
(3.5)

 h_1 and h_2 are the "height" differences between the A and B and A and C points, respectively. For simplicity, we have assumed that the effective well depths are the same along the s_1 and s_2 paths and equal to D. To show that these interference features are indeed sensitive to the well depth, at least in this simple model, we show in figure 3.4 the influence of the well depth, D, on the drift scan (left panel) and the incident angle scan (right panel).

The same effect is responsible for the appearance of the rainbow maxima in diffraction scans, where for a particular final angle of scattering, the condition for positive (negative) interference is fullfilled.

The most important message of this section is that selective adsorption resonances are not the only phenomena that one can use for a construction of the potential and the estimate of its well depth. As shown in equations (3.3) and (3.4), there are other interference features

which strongly depend on the corrugation of the potential, but also on the well depth of the potential. The position and shape of these features can thus be used to estimate the potential well depth.

3.4 Effects of incident energy spread and its inclusion in CC calculations

In experiments, the distribution of energies in the incident beam of atoms cannot be made arbitrarily narrow. This distribution always has a finite width which is larger for larger mean incident energies [4]. However, the formalism of coupled channel equations is developed for incident particles represented by plane waves i.e. completely monochromatic. The effects of incident energy spread are usually included in the CC formalism in the following way. The CC transition probabilities, $|S(i, f; E)|^2$ should be calculated for a number of incident plane wave energies, E. The final value of the transition probability is given as

$$|S(i,f)|^2 = \int dE |S(i,f;E)|^2 P(E,E_i), \tag{3.6}$$

where $P(E, E_i)$ represents the distribution of energies of the incident beam centered around the mean incident energy, E_i .

The CC calculations can be very time consuming and the calculation of transition probabilities for a large number of incident energies is usually out of the question. However, we can approximate equation (3.6) with

$$|S(i,f)|^2 = \frac{1}{2} \left[|S(i,f;E_i)|^2 + \frac{1}{2} (|S(i,f;E_i - w)|^2 + |S(i,f;E_i + w)|^2) \right],$$
(3.7)

which requires a CC calculation for only three incident energies. The FWHM (full width at half maximum) of the experimental incident energy distribution is 2w.

Note here that equation (3.6) does not account for the possible interferences in the incident beam due to the finite incident energy spread.

Chapter 4

Model potentials for atom-surface scattering

4.1 "True" potentials

In a hypothetically ideal situation for the interpretation of atom-surface scattering the interaction potentials would be obtained from independent sources, such as the total energy calculations. The scattering experiments combined with the coupled channel calculations could then be used to test the potentials and see if some refinements are needed. This is usually not the case and one is faced with the experimental data only, often without a firm starting point for obtaining the potential. A firm starting point exists, however, in weakly bound, physisorbed adsorbate systems such as Xe on graphite. In these cases a very reliable potential can be obtained as a superposition of the projectile - adsorbed atom potentials known from the gas phase, combined with the long-range interaction of the projectile with the substrate material. In other cases of strongly bound, chemisorbed adsorbates, the model potentials are usually needed. If one wants to carry out extensive search in the space of the potential parameters, it is advantageous if the potential can be represented by a superposition of the analytic functions in both direct and inverse space. This speeds up the coupled channel calculations since the hamiltonian matrix can be guickly set up. In the next sections we present some model potentials which have this property. The physical interpretation of these potential is not of primary importance at present and will be discussed in the next chapter.

4.2 The CLMTCD potential

The CLMTCD potential was suggested by Cvetko, Lausi, Morgante, Tommasini, Cortona and Dondi in reference [34]. This model potential could be also considered as a "true" potential due to the fact that its parametrisation is based on the physical constants of interaction (such as the C_6 coefficient of the long range interaction ¹). The basic trick is to represent the "true" atom-site potential (in this case, exponential repulsion combined with the sum of attractive contributions (C_6 , C_8 ...) damped with Tang-Toennies functions [31]) as a superposition of exponential functions in the radial coordinate which are then easily transformed in the inverse space i.e. their Fourier components are analytical functions [30]. The pair potential is given as

$$v(r) = \frac{C_6}{120} \left(\frac{b}{3}\right)^6 \left(ae^{-br} - \xi e^{-(2/3)br} - e^{-(1/3)br}\right), br \le 16.6$$

¹The origin of the attractive interaction is discussed in chapter 5.

$$v(r) = \frac{C_6}{120} \left(\frac{b}{3}\right)^6 a e^{-br} - \frac{C_6}{r^6 - Q^2 r^4}, br \ge 16.6, \tag{4.1}$$

where Q is related to multipolar coefficients C_6 , C_8 and C_{10} of the attractive interaction as

$$Q = \left(\frac{C_8 C_{10}}{C_6^2}\right)^{1/6},\tag{4.2}$$

and the coefficient ξ is determined by the continuity condition of v(r) at br = 16.6 to be

$$\xi = \frac{(14.6 + 0.918(Qb)^2)}{(1 - (Qb/16.6)^2)}. (4.3)$$

This particular form of the potential has been shown to reproduce the various existing forms of atom-atom potentials in the gas phase rather accurately [34]. The numerical constants in equation (4.1) (120 and 16.6) should not be taken too seriously - they were chosen to best represent the H-H³ Σ potential [34].

The potential can also be made elliptical [30] by scaling the radial coordinate r as

$$r' = \sqrt{z^2 + (\eta_x x)^2 + (\eta_y y)^2},$$
 (4.4)

writing r' instead of r in equation (4.1), and multiplying the potential by $\eta_x \eta_y$. When the CLMTCD potentials are used to describe the ordered (sub)monolayers of adsorbates, this procedure leaves the $V_{00}(z)$ component unchanged and independent on the ellipticity parameters η_x and η_y . The higher order Fourier components depend on the parameters η . These components become smaller as the parameters η decrease.

The ellipticity parameters mimic the electronic rearrangements in the surface plane that are possibly present in the target system. The electronic delocalization within the surface plane would require η_x and η_y to be smaller than 1.

Even with the substitution of eq. (4.4), the atom-surface potential has Fourier components which can be cast into an analytic form very suited for calculations [30]. This effectively means that one does not have to perform numerical integration in equation (2.17) each time a parameter of the potential is changed.

There is an additional feature of this potential which is worth mentioning. The authors of ref. [34] find that the product Qb is nearly the same for all inert-inert, alkali-alkali and inert-alkali atom pairs and equal to $Qb = 8 \pm 1$. This suggest a similar shape of all the potentials

examined. Futhermore, it is an interesting concept that there may be a combination of parameters related to the repulsive part of the potential (b) and the attractive part of the potential (Q) which is nearly universal. The contribution of higher multipole coefficients of the attractive interaction is contained in the value of ξ . If we set Q=0, taking into account only C_6 coefficient of the interaction (damped with Tang-Toennies function), $\xi=14.6$. For He-metal interaction, values of ξ between 75 and 84 ² have been proposed [33, 35, 93, 100]. Since the parameter ξ effectively determines the profile of the interaction potential in the z-direction (r-direction in the gas phase), this suggest a nearly universal shape of the He-metal interaction potentials, a feature discussed in references [3, 94].

4.3 Poisson sum formula and atom-surface potentials

A very convenient and powerfull method for constructing model atomsurface potentials is based on the application of the Poisson sum formula which reads:

$$\sum_{n=-\infty}^{\infty} f(x+n) = \sum_{k=-\infty}^{\infty} \exp(2\pi i k x) \int_{-\infty}^{\infty} f(x) \exp(-2\pi i k x) dx. \quad (4.5)$$

The simplest example of the use of this equation is a model of interaction of a particle with a discrete lattice of atoms, separated by a lattice constant a in one dimension (x). One such model for the total potential is

$$V(x,z) = -2De^{-\gamma z} + Da\sqrt{\frac{\alpha}{\pi}} \sum_{l} e^{-\alpha(x-la)^2} e^{-2\gamma z}.$$
 (4.6)

Applying the Poisson sum formula, we immediately see that the Fourier components of this potential are given as

$$V_{G\neq 0}(z) = D \exp(-\frac{\pi^2 k^2}{\alpha a^2}) \exp(-2\gamma z)$$

$$V_{G=0}(z) = D \left[\exp(-2\gamma z) - 2 \exp(-\gamma z)\right], \tag{4.7}$$

where $G = 2\pi k/a$. This is very convenient due to the fact that the bound states of the Morse potential can be calculated analytically as

$$E_n = -D\left[1 - \frac{\hbar\gamma}{\sqrt{2mD}}\left(n + \frac{1}{2}\right)\right]^2. \tag{4.8}$$

The model can be easily extended to two dimensions.

²One should note here that Qb = 8 implies $\xi = 95$.

4.3.1 Model potential for rectangular lattices

For rectangular lattices with lattice parameters a and b, we can construct the model potential as

$$V(x, y, z) = -2De^{-\gamma(z-z_0)} + Dab \frac{\sqrt{\alpha\beta}}{\pi} \sum_{h,l} e^{-\alpha(x-ha)^2} e^{-\beta(y-lb)^2} e^{-2\gamma(z-z_0)}. \quad (4.9)$$

The Fourier components of this potential are given by

$$V_{\mathbf{G}\neq 0}(z) = D \exp(-\frac{\pi^2 p^2}{\alpha a^2}) \exp(-\frac{\pi^2 q^2}{\beta b^2}) \exp(-2\gamma (z - z_0))$$

$$V_{\mathbf{G}=0}(z) = D \left[\exp(-2\gamma (z - z_0)) - 2 \exp(-\gamma (z - z_0))\right], \quad (4.10)$$

where $\mathbf{G} = (2\pi p/a, 2\pi q/b)$. Note here that the attractive part of the interaction is *not* written as a pairwise sum of the binary potentials i.e. this part of the potential is uncorrugated. One could easily devise similar models in which the attractive part of the interaction potential is also corrugated. Note also that the attractive part of the interaction potential includes the long range attractive interaction with the substrate material. Summing over the shortest four \mathbf{G} vectors, we obtain an approximate expression for equation (4.9):

$$V(x, y, z) = D \left[\exp(-2\gamma(z - z_0)) - 2 \exp(-\gamma(z - z_0)) \right]$$

$$+ 2D \exp(-2\gamma(z - z_0)) \left[\exp(-\frac{\pi^2}{\alpha a^2}) \cos(\frac{2\pi x}{a}) + \exp(-\frac{\pi^2}{\beta b^2}) \cos(\frac{2\pi y}{b}) \right].$$

$$(4.11)$$

This form is very commonly found in the literature from the very beginning of theoretical interpretation of the scattering of thermal energy atoms from surfaces [8].

4.3.2 Model potential for HCP lattices

The easiest way to derive the expression for an interaction potential for this type of lattices is to visualise the HCP lattice as two interpenetrating rectangular lattices with $b=a\sqrt{3}$, mutually displaced by $(\pm a/2, \pm a\sqrt{3}/2)$. In this case, we may assume that $\alpha \approx \beta$, and we set $\alpha = \beta$. The final formulas read

$$V(x,y,z) = -2De^{-\gamma(z-z_0)} + Da^2 \frac{\sqrt{3}}{2} \frac{\alpha}{\pi} \sum_{l} e^{-\alpha(x-x_l)^2} e^{-\alpha(y-y_l)^2} e^{-2\gamma(z-z_0)}, (4.12)$$

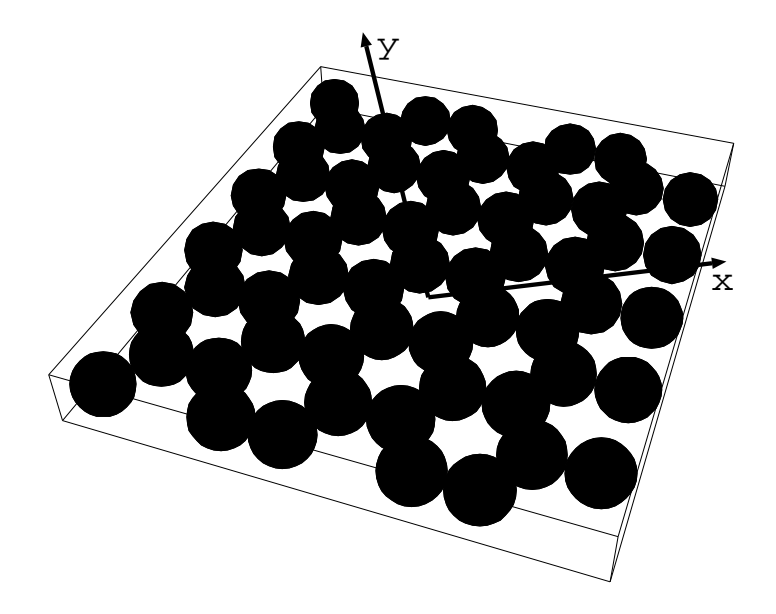


Figure 4.1: The structure of graphite and the choice of coordinate system.

and

$$V_{\mathbf{G}\neq 0}(z) = D \exp\left(-\frac{4\pi^2(m^2 - mn + n^2)}{3\alpha a^2}\right) \exp(-2\gamma(z - z_0))$$

$$V_{\mathbf{G}=0}(z) = D \left[\exp(-2\gamma(z - z_0)) - 2\exp(-\gamma(z - z_0))\right], \quad (4.13)$$

where $\mathbf{G} = m\mathbf{g}_1 + n\mathbf{g}_2$, $\mathbf{g}_1 = g\mathbf{y}_0$ and $\mathbf{g}_2 = g\sqrt{3}/2\mathbf{x}_0 - g/2\mathbf{y}_0$, and where \mathbf{x}_0 and \mathbf{y}_0 are the unit vectors in x and y directions, respectively ³.

Note that the ranges of all nonzero Fourier components of the interaction potential obtained in this way are the same. This is a consequence of the specific model we use and need not be the case for a "true" potential.

4.3.3 Honeycomb (graphite) structure

Our choice of the coordinate system with the lattice vectors is represented in figure 4.1.. The sum of the binary potentials for this structure can be performed as two sums: One over the coordinates of the whole lattice which is a HCP sum have we already calculated, and the other over the local coordinates of the atoms in a particular unit cell. One has to take some care not to overcount the sites in this procedure. The

³Note here that $m^2 - mn + n^2 > 0$ for all m and n.

total potential can be written in the form

$$V(\mathbf{r}) = V_{att}(z) + \frac{D}{2}a^2 \frac{\sqrt{3}}{2} \frac{\alpha}{\pi} \sum_{l} \frac{1}{3} \sum_{v} e^{-\alpha(x - x_{v,l})^2} e^{-\alpha(y - y_{v,l})^2} e^{-2\gamma z}, \quad (4.14)$$

where the index l represents the HCP coordinates of the unit cell centers and index v represents the individual atoms in the unit cell. The factor of 1/3 takes care of avoiding the overcounting. The trick is to use the Poisson sum formula for the HCP sum and then to explicitly sum over the local coordinates within the unit cell. This yields

$$V_{\mathbf{G}\neq 0}(z) = F_{m,n}D \exp\left(-\frac{4\pi^2(m^2 - mn + n^2)}{3\alpha a^2}\right) \exp(-2\gamma z)$$

$$V_{\mathbf{G}=0}(z) = D \exp(-2\gamma z) + V_{att}(z), \tag{4.15}$$

where the form factor $F_{m,n}$ is given as

$$F_{m,n} = \frac{1}{3} \left[\cos \left(\frac{2\pi (2m-n)}{3} \right) + (-1)^n 2 \cos \left(\frac{\pi (2m-n)}{3} \right) \right], \quad (4.16)$$

and the meaning of m and n is the same as in the HCP case.

4.3.4 Other analytical representations of the V_{00} component of the interaction potential

In some cases the Morse potential cannot accurately reproduce the bound states of the potential. There are other analytic potentials which support the bound states whose energies can be calculated from analytic formulas. The preceding model potentials can be easily redesigned in such a way that their zeroth order Fourier component represents the analytic potential of our choice. Some possible choices of the zeroth order Fourier potentials one might want to consider are **3-9 potential** given as

$$V_{00}(z) = \frac{3^{1.5}D}{2} \left[\left(\frac{\sigma}{z + z_0} \right)^9 - \left(\frac{\sigma}{z + z_0} \right)^3 \right], \tag{4.17}$$

where D is the well depth, z_0 is the position of the potential minimum and σ is the range parameter. The bound states of this potential are approximately given by

$$E_n = -D\left(1 - \frac{(n+1/2)}{L}\right)^6,\tag{4.18}$$

where

$$L = \frac{3.07}{\pi} \sqrt{\frac{2mD\sigma^2}{\hbar^2}},\tag{4.19}$$

The **p-potential** or Mattera *et al* potential is given as

$$V_{00}(z) = D\left\{ \left[1 + \frac{\lambda(z - z_e)}{p} \right]^{-2p} - 2\left[1 + \frac{\lambda(z - z_e)}{p} \right]^{-p} \right\}, \quad (4.20)$$

where D is the well depth, z_e is the position of the potential minimum, $\lambda > 0$ and $-1 \le 1/p \le 1$. The bound states of this potential are given as

$$E_n = -D \left[\left(1 + \frac{\delta}{A^2} \right)^{\frac{1}{S}} - \frac{n + 1/2}{AS} \right]^S,$$
 (4.21)

where

$$\frac{1}{S} = \frac{1}{2} - \frac{1}{4p} \left(3 + \frac{1}{p} \right)$$

$$A = \frac{\sqrt{2mD}}{2\hbar\lambda}$$

$$\delta = \frac{1 + \frac{1}{p}}{32p}.$$
(4.22)

4.3.5 Other representations of surface corrugation

There are other suitable functions which can be employed instead of the commonly used gaussians to represent the lateral profile of the binary potential (and thereby also the profile of the total corrugation). For example one could use functions like $1/(a^2+x^2)$ or $1/\sqrt{(a^2+x^2)}$ which have analytic Fourier transforms. The formulas for the Fourier components of the interaction potential are easily derived for these cases. One might also wonder whether the assumption of the gaussian lateral profile is too restrictive. Here we just want to point out that it can be easily shown that the classical turning point profile from a single adsorbate is not a gaussian but a paraboloid, given (for energies where the attractive part of the interaction can be neglected) as

$$z_t(\rho) = C(E) - \frac{1}{\gamma} \alpha^2 \rho^2, \tag{4.23}$$

where $\rho^2 = x^2 + y^2$. It has been shown experimentally that the classical turning point profile of the adsorbed CO at high incident projectile energies can to a good approximation be represented by a half sphere [36, 81]. A half sphere can be well represented by a paraboloid.

Chapter 5

Construction of realistic He-target potentials: The problem of chemisorbed adsorbates. Finite temperature effects.

5.1 A "proper" way of constructing the He-target potential

A proper way to construct the He-target potential would consist in calculating the total interaction energy for a range of the projectile z coordinates and for a number of (x, y) coordinates within the surface unit cell of the target. From this data set one could construct the Fourier components of the interaction potential, perform the CC calculations and thus test the potential in comparison with experiment.

This approach is not feasible for several reasons. First, the inclusion of attractive interactions in the total energy calculations is still in a nascent phase. Some progress has been achieved, but this problem still lies in the center of scientific interest and has not been completely resolved yet. Second, the number of points which need be sampled in (x, y, z) space is fairly high and a lot of CPU time would be needed for such a task. This problem should be overcomed in the future. Third, the quality of information one would obtain from such a calculation is questionable. In particular, it is questionable as how much would such a calculation contribute to our understanding of the physics responsible for the shape and magnitude of a particular potential. This approach is in fact partially followed in section 6.3 where its shorcommings and advantages become apparent.

In the following sections we shall discuss the physical effects which determine the projectile - target potential. Although we cannot quantify them without extensive calculations, a qualitative discussion of these effects will be presented.

5.2 Attractive interaction

The long range interaction of a He atom (or any other projectile atom) with an adsorbed atom or molecule is asymptotically given as

$$V_{att}^{He-ads.} = -\frac{C_6^{eff}}{|\mathbf{r} - \mathbf{r}_{ads.}|^6},\tag{5.1}$$

where \mathbf{r} and $\mathbf{r}_{ads.}$ are the coordinates of the projectile and the adsorbate atom, respectively. The C_6^{eff} constant of interaction may be different from the corresponding constant (C_6) when both atoms are in the gas phase. The origin of the attractive interaction when both atoms are in the gas phase is sketched in diagram 5.1. Basicaly, the electronic density fluctuations (bubbles in fig. 5.1) within the p and a subsystems couple

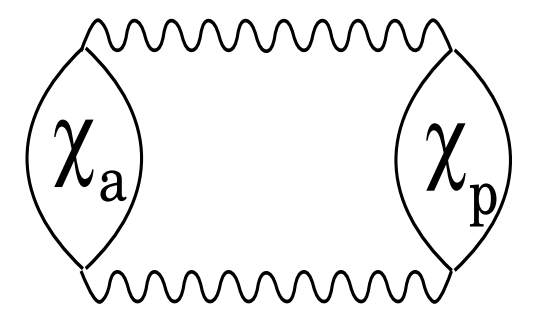


Figure 5.1: Lowest order Feynman diagram contributing to the attractive interaction between the p and a electronic subsystems.

to each other via the Coulomb interactions (wavy lines in fig. 5.1). When a and p are atoms or molecules, the evaluation of this contribution to the total energy produces the attractive interaction decaying asymptotically with the distance as $1/r^6$ where r is the separation between a and p. When p and a represent an atom and a semi-infinite crystal, the attractive interaction decays asymptotically with distance as $1/r^3$. In fact, the evaluation of diagram 5.1 is in principle possible for the whole range of r coordinate 1 . In the dipole approximation, which is valid for large r, one obtains inverse power divergencies $(1/r^6)$ and $1/r^3$ which are the consequence of the approximation itself and are not real features of the attractive interaction.

5.2.1 Physisorption and chemisorption induced changes to the projectile - adsorbate attractive interaction

When the adsorbate atoms are physisorbed, the change of projectile-adsorbate attractive interaction takes place due to the presence of a third polarizable body. In fact, this is a three body interaction which can be thought of as a contribution to the effective binary projectile-adsorbate interaction. The physical processes contributing to this three body interaction are sketched in fig. 5.2.

The Feynman diagrams of the type sketched in fig. 5.2 must be included in the calculation of the total attractive interaction (see ref. [11, 89] for more detailed information). The polarization induced in

 $^{^{1}}$ When r is so small that the electronic densities of the subsystems overlap, the change in eigenenergies of the subsystems takes place and in the evaluation of diagram 5.1, one must take this fact into account.

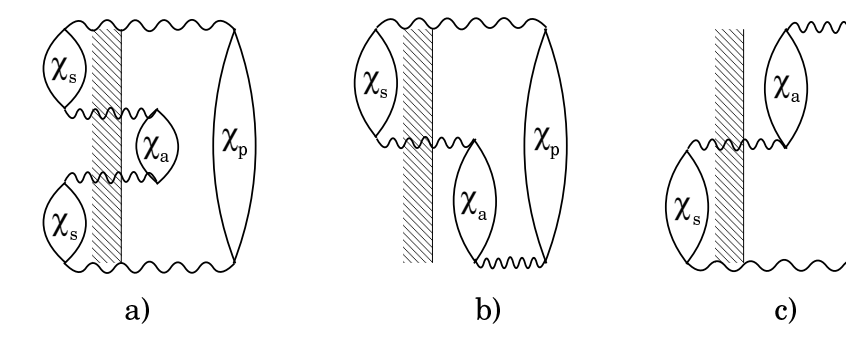


Figure 5.2: Three-body terms in the projectile (p) - adsorbate (a) on substrate (s) interaction.

the adsorbate (a) couples to the analogous polarization in the projectile atom (p) not only directly, but also indirectly, through the substrate material (s).

When the third polarizable body is a substrate material, one usually speaks of McLachlan's three body contribution (see e.g. refs. [6, 11, 37, 53]). This contribution enhances the attractive interaction (but see reference [55] for the change in interaction between two adsorbed atoms). In a (sub)monolayer of adsorbates, the third polarizable body can be another adsorbate atom/molecule. This three-body contribution to the interaction is called Axilrod-Teller-Muto (ATM) interaction and is usually ² repulsive [37, 39, 40, 52, 53].

For the calculation of polarization bubbles in fig. 5.2, one needs to know the energy levels and their population in all three subsystems participating in the interaction (p,a,s). When the adsorbate is weakly bound to the substrate, we may take these levels to be the same as if all the particles were infinitely separated, i.e. free. In the case of a chemisorbed adsorbate, the energy levels and their population change in p and s subsystems and this effect contributes to the interaction energy already in the lowest order (fig. 5.1) and also in all higher order diagrams (fig. 5.2). We may try to incorporate all these changes in the effective constant of long range interaction, C_6^{eff} as in equation (5.1) (see also references [5, 40]).

There are some calculation related to the C_6^{eff} constant for the CO molecule adsorbed onto the Ni and Cu surfaces. It turns out that C_6^{eff}

²This contribution can also be attractive but only when the three atoms in question are arranged nearly colinearly [40]. The attractive contribution to ATM interaction is negligible in atom-surface scattering since the projectile atom reflects from the surface at about 2-3 Å above the centers of the atoms/molecules in the topmost target layer. Thus, the ATM interaction is generally repulsive in this case.

can be even 100 % larger than the gas phase value, C_6 [10]. This is due to the fact that the volume, and thus the polarizability of adsorbed CO molecule is larger in the adsorbed phase due to the transfer of electrons from the metal to the $2\pi^*$ orbital of CO [5, 6]. One of the aims of this work is also to test such predictions.

The total attractive interaction between the projectile and the adsorbed overlayer is given in the first approximation as sum (over the adsorbate lattice sites) of these binary interactions:

$$V_{att}^{He-lay.} = -\sum_{ads.} \frac{C_6^{eff}}{|\mathbf{r} - \mathbf{r}_{ads.}|^6}.$$
 (5.2)

For large values of z, the sum can be replaced with the integral and we obtain

$$V_{att}^{He-lay.} \rightarrow_{z \to \infty} = -\frac{\pi C_6^{eff}}{2A_c} \frac{1}{z^4}, \tag{5.3}$$

where we have assumed that the centers of adsorbates lie in the z=0 plane. In fact, it can be shown that equation (5.3) represents the zeroth Fourier component of this part of the interaction exactly at all distances. Of course, we may fit the experimental data with the various different and convenient functional forms of binary attraction. The relation (5.2) can be used after the successfull fitting to extract information on C_6^{eff} .

The attractive interaction of the projectile with the underlying substrate can be written for the case of physisorbed adsorbates as

$$V_{att}^{He-subs.} = -\frac{C_3}{(z - z_s + d)^3},$$
 (5.4)

where z_s is the distance which depends on the electronic structure of the substrate (see e.g. [11]), and d is the normal distance between the adsorbate atoms plane and the topmost substrate plane. This relation cannot be expected to hold in the case of chemisorbed adsorbates for the following reason. In the case of strong chemisorption, the charge in the substrate material rearranges to form a chemical bond with the adsorbate. Most notably, the charge in the plane of substrate atoms lying directly underneath the adsorbate atoms is very different than in the case of clean substrate surface. These effects can be very strong and it is known that some adsorbates can induce the reconstruction of the surface [44]. The simplest way to account for this redistribution would be to "renormalize" the z_s distance which is related to the decay range of the surface electronic density. For example when the transfer

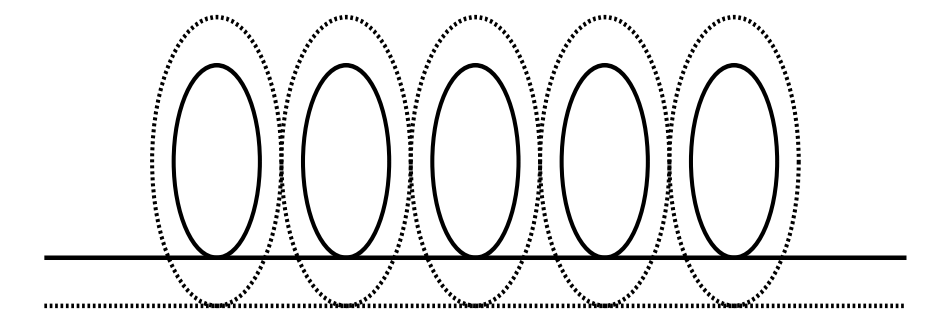


Figure 5.3: Full lines: Physisorption; Dashed lines: Chemisorption. Horisontal lines denote the position of the effective "jellium edge" in the case of physisorbed and chemisorbed adsorbates.

of charge is in the direction from the surface to the adsorbate, the additional charge on the adsorbate atom causes a "renormalization" of the C_6 constant of the projectile - adsorbate interaction. It can also cause significant changes in the repulsive part of the potential, possibly shifting it towards the projectile atom. But is also causes a depletion of the charge in the surface layer, and thus a renormalization of this interaction. We might be able to account for this change by assuming that the negative jellium edge of the crystal is closer to the position of the outmost substrate nuclei than it would be when adsorbate atoms were not present. This would require a decrease in the z_s distance (z – $(z_s - \Delta z_s) = z - z_s + \Delta z_s > z - z_s$, although such a procedure is no doubt only approximate. In particular, one can also expect a change in the C_3 coefficient. The situation we discuss here is represented roughly and in a very exaggerated fashion in fig. 5.3. It is also obvious that the effects discussed here will depend on the density of the adsorbate overlayer. Overlayers with higher coverage will cause more drastic changes in the projectile-substrate interaction potential.

The preceding discussion reveals serious problems that one can expect in dealing with chemisorbed adsorbates. Namely, the superposition of the projectile-adsorbate and projectile-substrate interactions is not so simple as in the case of physisorbed adsorbates. In particular, it is not clear which part of the rearranged charge should be associated with the adsorbates and which part with the substrate. The situation is additionally complicated by the fact that the localized adsorbate orbitals hybridize with the substrate bands which in principle represent delocalized electrons. Any distinction between the projectile-adsorbate and the projectile-substrate interaction is in fact at least partially artificial. Despite all these problems, we shall try to find pseudopotentials that

can reproduce the experimental data. From the previous discussion we can say in advance that the *total* potential will be much more appropriate than its decomposition into the parts related to projectile-adsorbate and projectile-substrate interactions.

The simplest and the most naive representation of the total attractive part of the He-target interaction would be a simple sum of the terms in equations (5.3) and (5.4) yielding

$$V_{att} = -\frac{C_3}{(z - z_s + d)^3} - \frac{\pi C_6^{eff}}{2A_c} \frac{1}{z^4}.$$
 (5.5)

This equation is approximate in many aspects. First, we have extended the asymptotic expressions to the whole range of the z coordinate. This may cause the attraction to be too strong in the region of small z and divergent for $z = z_s - d$ and z = 0. This can be "repaired" by the damping of attractive interaction at short distances e.g. by using the Tang-Toennies correction [31] or any similar one. But it should be kept in mind that these corrections are rather heuristic (but plausible, see reference [38]) and do not have a firm theoretical background. We have also disregarded all the terms which may cause the corrugation of the attractive potential. Second, we have accounted for all the screening effects which arise as a consequence of the proximity of the adlayer and the substrate material in an oversimplified way (by renormalizing the C_6 constant of interaction). Third, we have neglected all higher multipolar coefficients of the attractive interaction $(C_8, C_{10}, ...)$ assuming that they are much smaller than the effective C_6 coefficient. Including all these effects is possible in the case of weekly bound adsorbates but it seems to be rather difficult in the case of chemisorbed adsorbates. Thus, we neglect many of these effects as their inclusion would only additionaly complicate an already very complicated problem. We must keep in mind, however, that all the values of the coefficients we obtain when comparing the calculations with experimental data must be considered as "dressed". These values are "dressed" with all the effects we have disregarded and effectively put in the simplified forms and constants.

It is much more convenient to speak of the effective potential itself, characterizing its well depth, position of the minimum, steepness of its repulsive part ... than to speak of physical origins of the potential. For example, we might be totally unable to separate the contributions from the C_6 and C_7 , C_8 ... components of interaction. This is even more so if we have in mind that the long range expressions for the attractive interactions are not expected to hold in the region where the projectile

is in the vicinity of the target. However, we can certainly determine the approximate functional dependence of the interaction potential. In the case of chemisorbed adsorbates, comparison of this function with the one which could be expected if the adsorbates were physisorbed may yield additional insight in the character and physical consequences of chemisorption.

5.3 Repulsive interaction

If the substrate material is a low index surface of a metal, we can neglect the corrugation of the substrate potential as regards the interaction with thermal energy atoms. In fact, if the adsorbed overlayer is sufficiently dense, we can completely disregard the repulsive component of the projectile interaction with the substrate. In this case, the projectile rebounds in the region where the substrate electronic density (and thus the repulsive component of the interaction) is completely negligible. In the cases when the density of adsorbed overalyer is very low, the repulsive projectile-substrate interaction must be taken into account. The easiest way to do this is to add this repulsive interaction only to the $V_{00}(z)$ component of the total potential. The repulsive interaction arising from the adsorbed atoms or molecules is usually the dominant part of the total repulsive interaction and produces the corrugation of the potential. It is often assumed that the repulsive interaction can be well described by an exponential function of relative distance. This applies both to the binary potentials in the gas phase and to the zeroth order Fourier component of the repulsive projectile-target interaction. We shall assume that this specific functional relation holds in the case of adsorbed atoms too.

5.3.1 Esbjerg and Nørskovs ansatz

Esbjerg and Nørskov predict that the repulsive part of the interaction potential is directly proportional to the electronic density of the target, $\rho(\mathbf{r})$ i.e.

$$V_{repulsive}(\mathbf{r}) = \alpha \rho(\mathbf{r}). \tag{5.6}$$

Thus, if one knew the electronic density of the target from e.g. density functional calculations, one could construct the repulsive component of the total potential from eq. (5.6). The "constant" α , proved, however, not to be universal. Depending on a system in question and a theoretical method used, values from $\approx 200 \text{ eV}$ a_B^3 to $\approx 600 \text{ eV}$ a_B^3 have

been obtained [64, 65]. The value recommended by Takada and Kohn [41, 42], and also by Celli in ref. [43], is $A \approx 500$ eV a_B^3 . This is in agreement with Nordlander and Harris calculations [45]. The value suggested by Manninen *et al* is A = 205 eV a_B^3 . The value suggested from the He-Cu interaction potential calculations by Batra [66] is A = 375 eV a_B^3 .

5.3.2 Anticorrugation effects

Although equation (5.6) proved to be quite usefull for interpretation of atom scattering from surfaces, it now seems that it cannot be used for all systems in question. In particular, when one compares the cases of Ne and He atoms scattering from Rh surfaces, there seems to be a kind of anticorrugation effect, i.e. whereas the Ne atom sees the potential maxima at the position of the electronic density maxima, the He atom sees the potential minima at the position of electronic density maxima. We do not expect this phenomenon to have any importance in the systems of our interest. One should remember, however, that relation (5.6) has a limited validity [28, 29].

5.3.3 Physisorption and chemisorption induced changes in the projectile - adsorbate repulsive interaction

In the case of physisorbed atoms, we can disregard the change in the repulsive part of projectile - adsorbate interaction, i.e. we can take it to be the same as in the gas phase. One may want to include the repulsive contribution arising from three-body interactions of Axilrod-Teller-Muto type in the effective binary potentials, but these contributions are usually very small.

For chemisorbed atoms, we can roughly expect a shift in the position of the repulsive potential wall. When the charge transfer is from the substrate (adsorbate) to the adsorbate (substrate) one can expect a shift of the repulsive interaction towards (away from) the projectile atom ³. One can also expect important changes in the "softness" of the repulsive interaction. These effects cannot be easily accounted for without the total energy calculations.

³Although this is a phenomenon one can a priori expect in this case, it may be negligible in real adsorbate systems, see section 6.3.

5.4 A concept of pseudopotential

Guided by the discussion preceding this section, we introduce the concept of a pseudopotential ⁴. The pseudopotential is not a "true" potential, i.e. a potential obtained from first principles calculation which properly accounts for all the physical effects contributing to the interaction. Nevertheless, a pseudopotential is ideally an excellent represenation of the true potential, which means that it correctly reproduces the shape and the magnitude of the true potential, though the physical effect responsible for the particular shape and magnitude cannot be or can only be roughly traced in the particular model of pseudopotential.

The pseudopotentials we propose can be, at least, roughly related to the physical properties of the system. For example, in the CLMTCD potential, the parameters η_x and η_y are roughly related to the smoothness and the lateral spread of the target electronic density. The parameter ξ can be roughly related to the importance of multipolar attractive interactions $(C_8, C_{10}, ...)$, although, as we discussed, this may be difficult to do for the targets involving chemisorbed adsorbates.

5.5 Thermal effects: Renormalization of the Fourier components of the interaction potential

The target material is not static, even at T=0 K. Thus, during the time in which the projectile interacts with the target, the target atoms move. Assuming that the target oscillations are fast on the scale of the interaction time 5 , the probability for inelastic transitions is small. We can thus disregard the inelastic channels. However, we can account for the change in the static potential introduced by the motion of the target atoms. This can be done by averaging the interaction potential components over the time related to the period of the target atom oscillations. This results in the temperature dependent renormalization of the Fourier components of the potential (see references [46, 47]).

However, the condition that the target oscillations are fast on the scale of the interaction time is almost never met in HAS, and the descibed way of including the temperature in the CC calculations is there-

⁴For a general discussion of the pseudopotential concept, see reference [67].

⁵This also means that the projectile energy is low with respect to the target frequencies (energies).

fore very questionable. One could account for the high frequency target modes in this way, but for these modes the correction to the potential is generally negligible [46]. In principle, one should account for the loss of intensity from the elastic channels and its redistribution into the open inelastic channels. This is a difficult task and has not been yet satisfactorily solved.

5.5.1 Heuristic expressions for the effects of finite temperature on the elastic scattering probabilities

The simplest way to approximately include effects of temperature in the elastic CC calculations would be to multiply *all* the elastic diffraction probabilities with the same number smaller than 1, i.e.

$$|S_{\mathbf{G},0}|_{T_S}^2 = e^{-2W(T_S)}|S_{\mathbf{G},0}|_{el}^2, \tag{5.7}$$

where the subscript el indicates a value of the S matrix element obtained from the purely elastic calculations. The total number of particles scattered into inelastic channels is given as $1-e^{-2W(T_S)}$ and $2W(T_S)$ could be interpreted as a Debye-Waller exponent related to inelastic processes. Equation (5.7) is approximate and usually poorly satisfied in atom-surface scattering. What is often observed is that the intensities of different diffraction peaks behave differently with temperature some of them decaying more slowly than the others as the temperature increases. A way to account for this effect is given by the following equation:

$$|S_{\mathbf{G},0}|_{T_S}^2 = e^{-cT_S q_{\mathbf{G}}^2} |S_{\mathbf{G},0}|_{el}^2, \tag{5.8}$$

where c is a parameter related to the surface Debye temperature [50], and $q_{\mathbf{G}}$ is the perpendicular momentum exchange related to diffractive channel \mathbf{G} , sometimes calculated in the literature by including the Beeby correction for the finite well depth [51, 52].

None of the expressions written in this subsection cannot be shown to hold exactly. As shown by Levi and Suhl [48], a simple factorisation of the temperature effects resembling the Debye-Waller factor known from the neutron and X-ray scattering can be achieved only under rather special conditions, such as for extremely fast incident atoms and also for slow atoms and extremely hard lattice [48]. For the conditions usually met in HAS, a simple factorisation of the temperature effects as in equations (5.7) and (5.8) cannot be expected to hold. A general discussion of Debye-Waller effect can be found in reference [49].

Chapter 6

Real adsorbate systems: Comparison of experimental data with CC calculations

In this chapter we intend to show that it is in principle possible to construct a reliable interaction potential for scattering of thermal energy atoms from ordered (sub)monolayers of adsorbates. The sequence of systems we consider here is ordered in accord with the theoretical effort needed for their analysis. Thus, we start with the simplest system of an ordered Xe monolayer on graphite. Since in this system the Xe atoms are physisorbed, one can expect that the well known He-Xe potentials from the gas phase will be a very good point of departure for the calculation of the He-surface interaction. In addition, there is a wealth of experimental information concerning this system. The next system we consider is the ordered $c(2\times 2)$ phase of Cl atoms on Ag(001). Although this is a complicated adsorbate system, there are very precise experimental data and an electronic density calculation for this system [68, 71]. This will prove to be a very usefull starting point for our analysis. Armed with the knowledge we gained in examining these systems, we consider the more difficult and less explored systems of CO monolayers adsorbed on surfaces of Cu and Rh.

6.1 Xe/graphite

6.1.1 He-Xe gas phase potential

The gas phase potential used in our analysis has been suggested by Cvetko et~al in ref. [34]. This type of the potential was described in section 4.2. The parameters suggested by these authors are (in atomic units): C_6 =19.56, Q=5.0, b=1.715 and a=7550. The authors of reference [34] show that this potential is compatible with the potentials previously suggested on the basis of experimental information. We assume that the effective interaction of He atoms with the adsorbed Xe atoms is the same as in the gas phase. Additionally, we extend the functional behaviour of this potential for br < 16.6 (equation (4.1) to the whole range of r coordinate. According to ref. [34], this is an excellent approximation to the potential except in highly asymptotic region of the r coordinate where the interaction energy is equal to zero within 0.1 meV.

6.1.2 He-graphite potential

Xe atoms are large so that in the region of space sampled by the He atoms, only the attractive interaction of He atom with the graphite substrate is of importance. We represent the long range He graphite

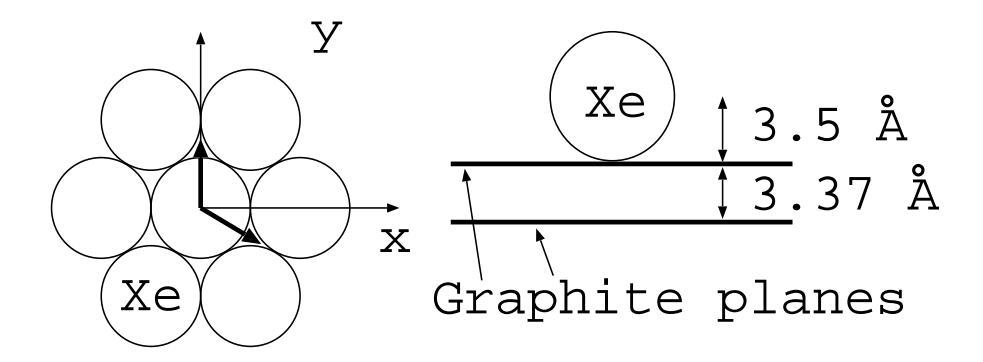


Figure 6.1: Coordinate system and \mathbf{g}_1 and \mathbf{g}_2 vectors (bold arrows) for Xe/graphite.

interaction as

$$V_{He-graphite}(z) = -\frac{C_3}{(z+d)^3},\tag{6.1}$$

where we take $C_3 = 184$ meV Å³ (the value recommended by Vidali et al [3] is $C_3 = 180 \pm 15$ meV) and d = 1.818 Å. This is consistent with the Xe-graphite surface distance of 3.5 Å and 3.37 Å interplanar graphite distance [57, 52] (see fig. 6.1). The same set of parameters was used in reference [52]. The total potential was constructed as a sum of the He-Xe gas phase potentials and the He-graphite long range interaction. Xe atoms are known to form a $(\sqrt{3} \times \sqrt{3})$ R30° lattice in registry with the substrate [56, 57], with a lattice constant 4.2695 Å.

6.1.3 Comparison of the results of CC calculations with experimental results

Our choice of the coordinate system and the basis vectors in the inverse space is presented in figure 6.1.

In figure 6.2 we present the results of CC calculation for this system, with the potential specified in the previous two subsections. The specularly scattered intensity is plotted as a function of incident angle. In this calculation, the CC basis was chosen by setting $n_{max} = 5$, $E_{min} = -29$ meV, and the equations were numerically propagated from $z_{min} = 1.1$ Å to $z_{max} = 13$ Å in 120 equidistant steps of z coordinate. The angle between the surface projection of the incident beam and the x axis is $\phi = 30^{\circ}$.

Unlike in ref. [52], we did not account for the temperature effects since they can be introduced only in a very approximate fashion (see

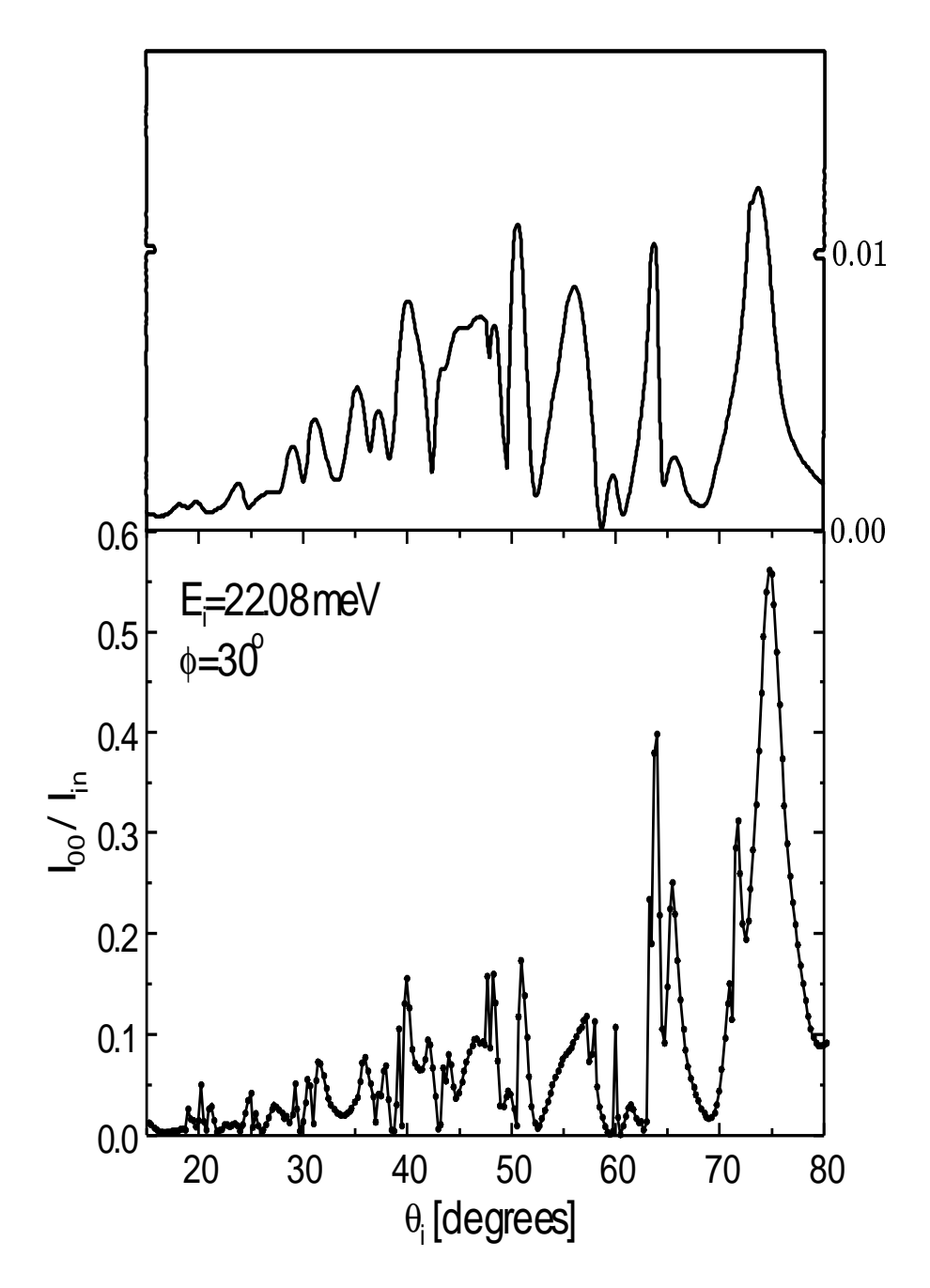


Figure 6.2: Upper panel: Experimental incident angle scan reproduced from reference [57]. Lower panel: Theoretical incident angle scan for He-Xe/graphite. Dots represent the points actually calculated. $E_i=22.08~{\rm meV},~\phi=30^o,~T_S=17~{\rm K}.$

discussion in section 5.5). Since we do not know the details of the experimental setup, we also did not account for any kind of geometrical factors, such as $\cos \theta_i$ factor (see discussion in section 3.1) which was included in ref. [52]. Even without these factors it can be seen that the agreement with the experimental data is excellent.

In figure 6.3 we present a comparison of the CC calculation with the experimental data for higher incident energy, $E_i = 63.8$ meV. In this calculation, due to a significantly larger number of open channels, we have taken $n_{max} = 9$ and $E_{min} = -29$ meV. Since the \overline{W} matrix is much larger in this case, the calculations are much slower than for $E_i = 22.08$ meV.

It can be seen that the CC calculations reproduce all the features found in the experiment although the shapes and widths of these features are different in the calculated and measured incident angle scans. This can be easily explained by taking into account the spread of energies in the incident beam which is more significant for higher incident energies. We did not try to account for this due to the fact that the time needed for a calculation of an incident angle scan for particular incident energy is too long.

In figure 6.4 we present a different type of experimental data in comparison with our calculations. Due to the movable detector arm, the authors of reference [56] were able to measure all diffraction intensities for fixed incident conditions ($E_i = 63.8 \text{ meV}$, $\theta_i = 0^o$). This type of measurement was not described in section 3.1. The diffraction peaks were taken along the y-direction (fig. 6.1) in the surface plane. It can be seen that the higher order diffraction peaks are wider. This is due to the incident energy spread. Assuming the gaussian profile of incident energy spread, with the width parameter $\sigma(E)$, the width parameter, $\sigma(\theta_f)$, of the diffraction peak observed at final angle θ_f can be calculated as (for normal incidence only)

$$\sigma(\theta_f) = \frac{1}{2\cos\theta_f} \frac{G_f}{k_i} \frac{\sigma(E)}{E_i},\tag{6.2}$$

where G_f is the modulus of the inverse lattice vector associated with the diffraction in a particular diffraction peak ((10),(20),...). In our calculations we have taken $\sigma(E)/E_i = 7 \%$.

To illustrate the importance of the attractive component of the interaction, we also display the results of independent CC calculations in which either the closed channels (evanescent waves) were excluded from the CC basis, or the attractive component of the total potential was excluded from the calculation. As can be seen from the compar-

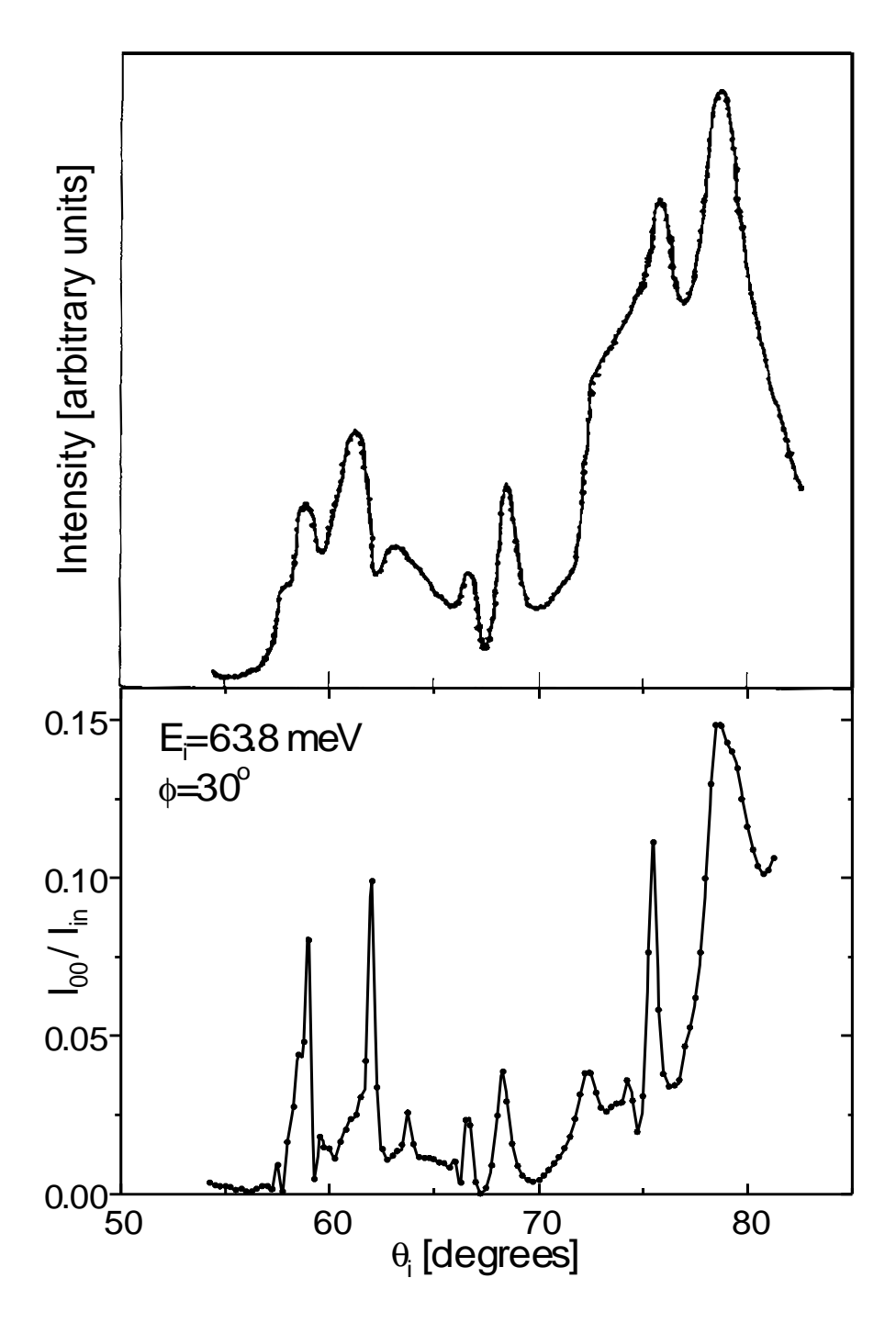


Figure 6.3: Upper panel: Experimental incident angle scan reproduced from reference [57]. Lower panel: Theoretical incident angle scan for He-Xe/graphite. Dots represent the points actually calculated. $E_i=63.8~{\rm meV},~\phi=30^o,~T_S=17~{\rm K}.$

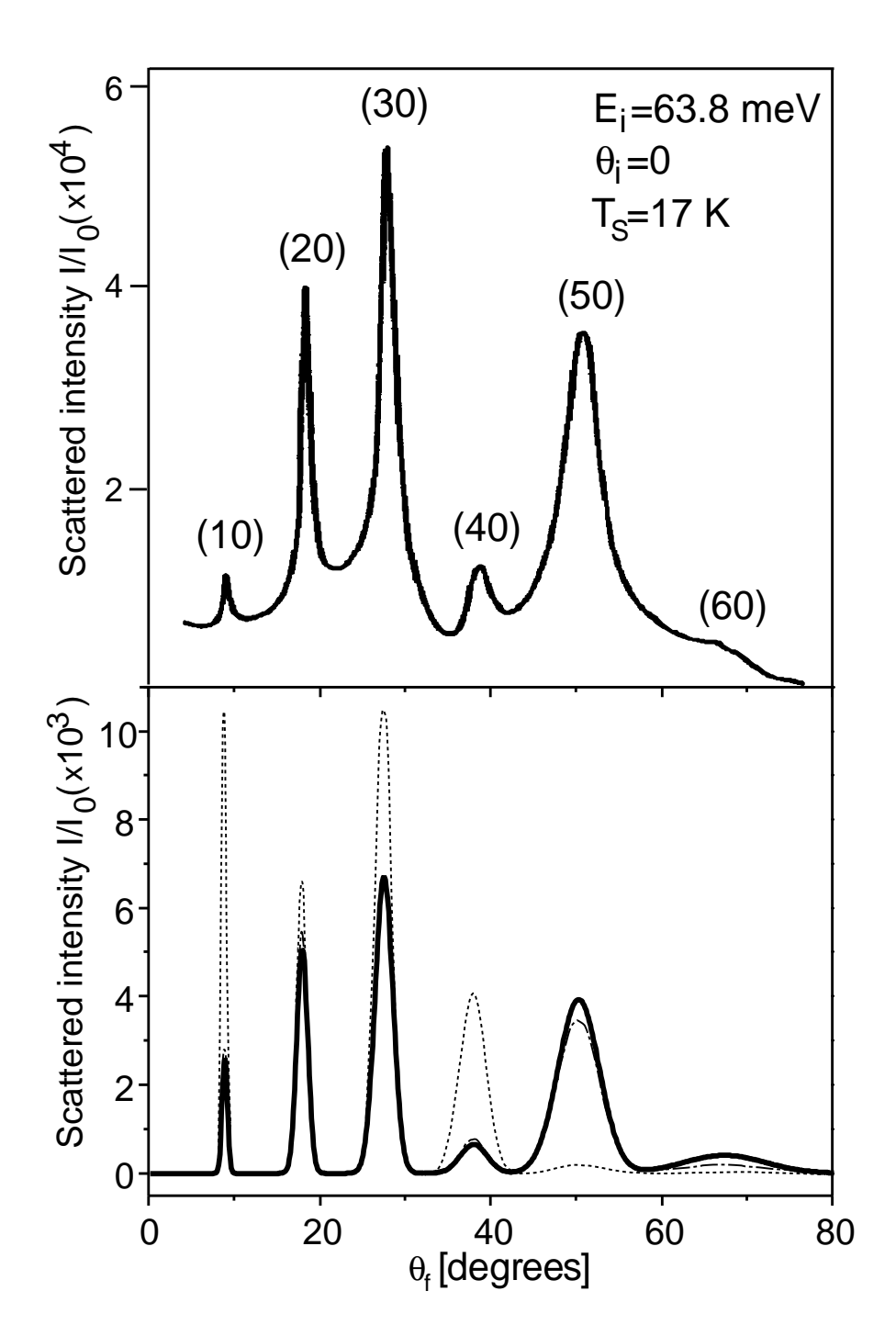


Figure 6.4: Upper panel: Experimental data reproduced from reference [56]. Lower panel: CC calculation (see text). $E_i=63.8$ meV, $\theta_i=0^o$, $T_S=17$ K.

ison of the full and dash-dotted line in lower panel of Fig. 6.4, the first effect caused by the exclusion of closed channels is large for the (60) diffraction peak which is more than a factor of 2 less intense in this approximation. However, the second effect of exclusion of the attractive potential is much more important since it influences the open diffraction channels in a more profound way and not only through the closed scattering channels. This effect is demonstrated by carrying out the CC calculations in which all the Fourier components of the attractive He-Xe/Gr(0001) interaction potential are neglected. The resulting diffraction spectrum shown by the dashed line in lower panel of fig. 6.4 is very different from the one obtained with the full potential and does not reproduce the experimental spectrum in any of the important aspects.

The overall intensities of diffraction peaks obtained by the CC calculation with the full potential are about a factor of 10 larger than those obtained experimentally. This suggests that about 90 % of He atoms in the experiment of Bracco et al. [56] were scattered inelastically. Indeed, the experimental intensities when summed over all the measured diffraction peaks (c.f. Table 1 of Ref. [56]) yield only 11.2 % of the incident intensity, which means that nearly 88.8 % of the scattered He atoms end up in inelastic channels, in excellent agreement with the factor of 10 that can be deduced from comparison of the results of our calculations and experiments. Note that this also implies a multiphonon scattering regime since the mean number of phonons \overline{n} excited in a scattering event can be estimated from $\overline{n} = -\ln(I/I_0) = -\ln(0.11) = 2.21$, where I and I_0 are the experimental values of the total intensity scattered into the elastic channels and the incident beam intensity, respectively, and I/I_0 is the Debye-Waller factor [2, 12, 60]. We calculate the theoretical value of \overline{n} for the present system using the EBA formalism described in detail in references [2, 12]. This yields $\overline{n} = 2.6$ [62], again in a very good agreement with the value that can be extracted from experiments.

Several very important conclusions can be drawn from the results presented in this section.

1 - The projectile-adsorbate potentials known from the scattering experiments in the gas phase represent an excellent starting point for studying the surfaces covered by physisorbed adsorbates. Higher order corrections to the interaction can be accounted for, as was briefly discussed in section 5.2, but in this case they are almost negligible and furthermore, the Axilrod-Teller-Muto contribution cancels partially with the McLachlan contribution

[52, 53, 54]. Additionally, the gas-phase potential is known within an uncertainty which is comparable to these corrections.

- 2 The calculated scattering intensities are insensitive to the precise shape of the interaction potential in the extreme asymptotic region. The binary potential we have used has in fact an incorrect asymptotic behaviour (exponentially decaying instead of $1/z^6$), since we did not take into account the terms contibuting to the potential for br > 16.6 (see section 4.2). Also, the CLMTCD model for the binary interaction potential proves to be as good as any other presently accepted model.
- 3 Although the number of particles scattered inelastically seems to be very large (compare the experimental and theoretical intensities in figures 6.2 and 6.4) due to the "softness" of Xe/graphite phonons [58, 59] (see also theoretical considerations in references [60, 61]), the global shape of the incident angle scan does not seem to be influenced by this. In fact, it seems that the inclusion of inelastic channels in the CC calculation would result only in slowly varying envelope to the purely diffractive CC calculation. Interestingly enough, this holds for both He incident energies considered although the current of inelastically scattered particles for $E_i = 63.8$ meV should be significantly larger than for $E_i = 22.08$ meV [60, 61].

6.2 $c(2 \times 2)Cl/Ag(001)$

According to reference [69], "This system is of particular interest for several reasons. The adsorption of chlorine on silver surfaces plays an important role in the selective oxidation of ethylene to ethylene epoxide, whereby the oxidation of ethylene to the thermodynamically stable end products, carbon dioxide and water, is an unwanted side reaction in this process. The selectivity is improved by the addition of chlorinated hydrocarbons. These compounds decompose at higher temperatures, producing chlorine atoms which are adsorbed on the silver surface and act as the true mediators.". The geometry of Cl overlayer on Ag(001) has been investigated in the past and, based on the LEED structure analysis, two geometrical arrangements of atoms have been proposed [70]. These structures were termed as SOM (simple overlayer model) and MLM (mixed layer model, with a quasiepitaxial AgCl surface layer - see figures in references [70, 68]). One of the spin-offs of our investiga-

tion will be a confirmation of the validity of the SOM model to describe the overlayer structure.

An overlayer of Cl atoms on Ag(001) has been studied very extensively with helium atom scattering in references [68, 71]. Additional electronic density calculations have been performed in references [68, 69]. The bound states of the V_{00} component of He-c(2×2)Cl/Ag(001) potential have also been determined experimentaly. These are all very usefull ingredients for our theoretical study.

Our plan is the following: We shall construct the "site" electronic densities i.e. the densities related to a particular atom of adsorbed Cl. We shall construct them in such a way that their simple geometrical superposition, together with the contribution from the Ag substrate, yields the total electronic density of the system.

According to Esbjerg and Nørskov's ansatz described in 5.3.1, the repulsive part of the potential is proportional to the electronic density. However, the constant of proportionality, A, may depend on the system in question. We adopt the value suggested by Manninen *et al* [63], $A = 30 \text{ eV} \text{ Å}^3$.

The attractive part of the interaction can be represented as a superposition of the long range attractive interaction of He atom with the Ag(001) substrate and the attractive interaction of a He atom with adsorbed Cl atoms. We shall fix the distance of Cl atoms from the Ag(001) substrate, fix the C_3 constant of He-Ag(001) interaction and treat the C_6^{eff} constant of He-Cl attractive interaction as a fit parameter. We shall show that it is possible to find the value of C_6^{eff} constant which optimally reproduces the experimental data. We test the thus obtained potential by performing the CC calculations and comparing the results with the experimental incident angle scans.

6.2.1 Construction of the He-c(2×2)Cl/Ag(001) interaction potential

The electronic density of the $c(2 \times 2)Cl/Ag(001)$ system, $\rho_{tot}(\mathbf{r})$, can be represented as a sum of the densities $\rho(\mathbf{r})$ each centered around a particular Cl site (l), $\rho(\mathbf{r}-\mathbf{r}_l)$, and the density of the substrate material. This gives

$$\rho_{tot}(\mathbf{r}) = \sum_{l} \rho(\mathbf{r} - \mathbf{r}_{l}) + f \rho^{Ag}(z), \qquad (6.3)$$

where we take

$$\rho(\mathbf{r}) = P\eta^2 \exp(-br'),\tag{6.4}$$

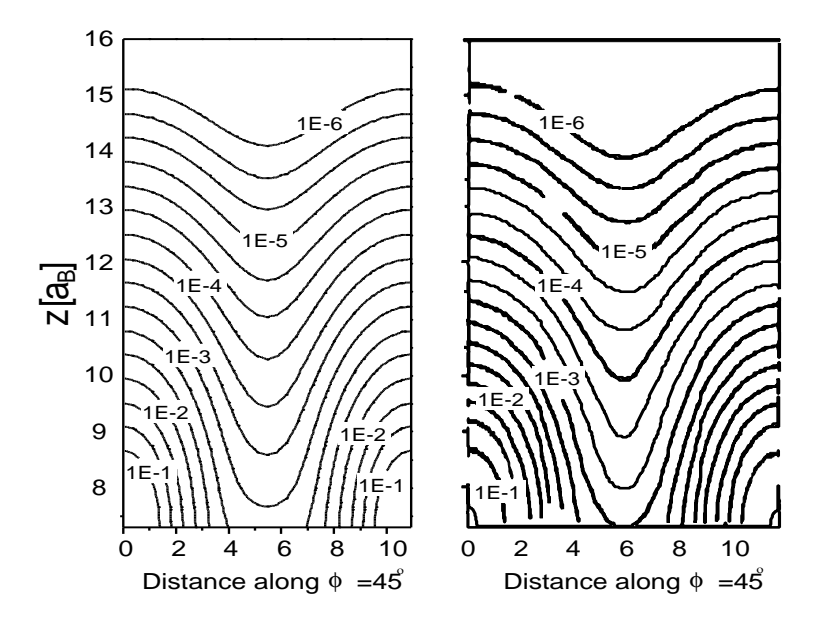


Figure 6.5: Left: Electronic density contours in $1/a_B^3$ along the $\phi = 45^o$ direction (fig. 6.6) of our model. Two Cl atoms are at the bottom left and the bottom right corner of the plot. The origin of z-coordinate is the same as in ref. [68]. Right: The calculation from ref. [68].

and
$$r' = \sqrt{\eta^2(x^2 + y^2) + z^2}. \tag{6.5}$$

 $\rho^{Ag}(z)$ represents the electronic density of a clean Ag(001) substrate. Note that we have weighed the substrate contribution with an unknown parameter f which is left to be determined by a fit. This is in agreement with the line of reasoning presented in Chapter 5 where we discussed that the substrate electronic density can be strongly perturbed by adsorption. Due to the symmetry of the Cl overlayer, there is no reason to assume different ellipticity parameters in x and y directions, so that we take $\eta_x = \eta_y = \eta$. For the representation of $\rho^{Ag}(z)$, we adopt the procedure and parameters suggested in references [30, 32, 51].

The electronic density contours obtained in ref. [68] can be well represented by choosing $\eta = 0.99$, b = 3.402 1/Å, $P = 8.098 \text{ 1/Å}^3$ and $f \approx 0.5$. Since f < 1, a charge transfer from Ag to Cl atoms is suggested, in agreement with the findings of ref. [69].

Our representation of the charge density is represented in fig. 6.5.

It can be seen that the agreement with the calculations presented in reference [68] is fairly good, except for the region of high electronic densities which is of no importance to us since this is the highly repulsive region of the He-c(2 \times 2)Cl/Ag(001) potential not sampled by the He atoms. It should be mentioned that the electronic density contours can be fitted with a similar succes with slightly different values of the parameter η (from 0.96 to 1.04). The attempts to fit the electronic density profile with the superposition of gaussian functions, as described in subsection 4.3.1, have proven unsuccesfull. This representation of the electronic density profile cannot correctly account for the fact that the contours of constant electronic density become more corrugated for higher electronic densities.

Knowing the electronic density, we construct the repulsive part of the binary (He-Cl) potential as $v_{rep}(\mathbf{r}-\mathbf{r}_l)=30~\mathrm{eV}$ Å $^3\rho(\mathbf{r}-\mathbf{r}_l)$. We represent the whole binary potential as the CLMTCD potential with the repulsive part constructed in this fashion. We additionally extend the functional dependence of CLMTCD potential for $br \leq 16.6$ (see section 4.2 and equation (4.1)) to the whole range of r. For the pairs of atoms studied by Cvetko et al in ref. [34] this proved to be an excellent approximation because $br \geq 16.6$ typically represents the asymptotic region of the binary potential in which the detailed functional dependence is of no importance for our purposes. Furthermore, we set $\xi = 14.6$. Since the repulsive part of the potential and the parameters η , b and ξ are fixed, the only remaining parameter of the binary potential is C_6^{-1} . The total potential is represented as a sum of the binary potentials over the Cl lattice sites. The geometric structure of the Cl overlayer is represented in fig. 6.6.

Additionaly, we add to the $V_{00}(z)$ component of the interaction potential the long range interaction of He with the Ag(001) substrate which we represent as $-C_3/(z-z_3+d)^3$ for $z>z_a$, and as $-C_3/(z_a-z_3+d)^3$ for $z< z_a$, where $z_a=2.5$ Å. This is the simplest form of damping of the attractive interaction. Note that the critical distance of 2.5 Å appears in these expression. Other choices of the critical distance, z_a , were tested and we found that the calculations are almost independent on the precise value of this distance as long as it was smaller than 2.5 Å but not too small to induce the divergence of the potential for small z values. Other parameters are d=1.748 Å, the distance between the plane of Cl atoms and the plane of the topmost Ag atoms, $C_3=249$ meV ų and $z_3=1.34$ Å, as suggested by Vidali et al in reference [3]. We have adopted the value of d from reference [72] where it has been measured by the EXAFS technique to the precision of $\pm 1\%$.

We have first tried to reproduce the bound states (of the $V_{00}(z)$

¹The choice of coefficient C_6 also fixes the coefficient a of the CLMTCD potential since the repulsive part of the potential is fixed - see eq. (4.1).

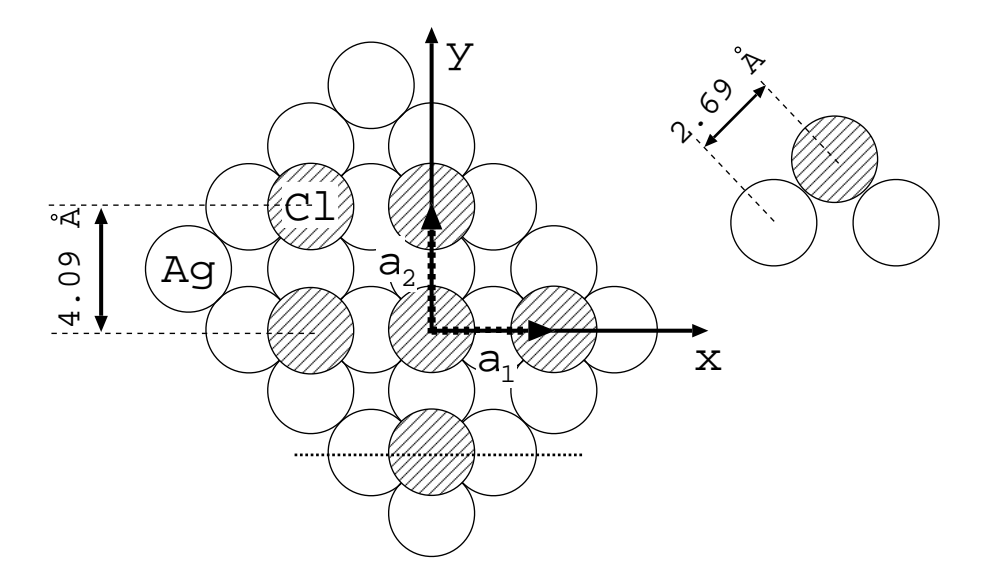


Figure 6.6: Geometry of the $c(2 \times 2)Cl/Ag(001)$ (SOM model) and our choice of the coordinate system.

component of the potential) reported in ref. [68], however this was not possible. The sequence of experimentally determined bound states cannot be obtained within our description of the potential. If we fit, for example, the deepest bound state determined experimentally (-13.7 meV), the higher energy states are reproduced very poorly (-8.2 meV, -4.4 meV, -1.9 meV, -0.7 meV, -0.1 meV), suggesting that the potential needed for description of the experimentally determined bound states is significantly narrower in the well region than our model potential. This may imply either the inadequacy of our model or an incorrect experimental asignment of the bound states. We consider the second possibility.

The well depth of the potential proposed by the authors of ref. [71] is ~ 18 meV. To our knowledge this is the deepest potential reported for He-surface scattering, comparable only to He-graphite potential (well depth ~ 16 meV) which, according to ref. [3], is an exceptionally deep potential and much deeper than other He-surface potentials measured experimentally for a number of chemically very different surfaces. The authors of refs. [68, 71] have tried to interpret the minima they observe in the experimental incident angle scans with the modified bound state resonance criterion which can lead to erroneous conclusions due to the

²The authors of ref. [71] encountered the same problems. The model potential they propose seems rather artificial.

Level	0	1	2	3	4	$D [\mathrm{meV}]$
Ref. [71]	-13.7	-6.9	-3.6	-1.8	-0.4	18
This work	-6.302	- 3.089	- 1.256	-0.401	-0.095	8.55

Table 6.1: Comparison of the bound states of the $V_{00}(z)$ component of the interaction potential between He and $c(2 \times 2)Cl/Ag(001)$ obtained in ref. [71] and in this work (in meV units). The experimental uncertainties are ~ 0.2 meV.

Parameter	a	b	ξ	η	C_6	C_3	z_3	f
Units	-	$1/ ext{Å}$	-	-	${ m meV\AA^6}$	${ m meV\AA^3}$	Å	1
Value	2213	3.402	14.6	0.99	6200	249	1.34	0.5

Table 6.2: The parameters of the He-c(2 \times 2)Cl/Ag(001) potential we propose.

fact that the system is strongly corrugated, and even the revised [71] bound state resonance criterion (which approximately includes corrugation of the potential) might fail in this case.

Having all this in mind, we have concluded that the deepest state in the potential suggested in ref. [71] was probably erroneously assigned and that the state they report as the first excited state corresponds in fact to the lowest energy state of the $V_{00}(z)$ component of the potential. The "renormalized" sequence of bound states can be fairly well represented within our model, with $C_6 \approx 6500$ meV Å³. However, by performing the CC calculation with the thus determined potential, we have found that even a better fit to the experimental data can be obtained by further relaxing the C_6 constant to the value of $C_6 = 6200$ meV Å³. This also fixes the parameter a to a = 2213.

The CC calculations with the thus constructed potential are presented in the next subsection. The bound states of our potential are compared to the bound states suggested in ref. [71] and shown in table 6.1. The well depth of our potential is D = -8.55 meV. The set of parameters of the potential is concisely presented in table 6.2.

6.2.2 Comparison of the results of CC calculations with the experimental data

In figure 6.7 we present a comparison between the measured and calculated incident angle scans for $E_i = 32.2$ meV. The surface projection of the projectile incident beam makes the angle of $\phi = 45^{\circ}$ with the x-axis in fig. 6.6. This calculation was performed with $n_{max} = 8$, $E_{min} = -31$ meV, and the equations were numerically propagated from $z_{min} = 0.5$ Å to $z_{max} = 9.9$ Å in 99 equidistant steps of the z-coordinate.

The bottom panel of fig. 6.7 displays the experimental results reproduced from ref. [71].

The topmost (first) panel displays the CC calculation results. The second panel displays the CC calculation results which include the incident energy spread of ~ 6 % of E_i (FWHM) in accordance with the experimental conditions. The third panel represents the results of the second panel which were adjacent averaged so that each point was calculated as the mean value of three points (the point in question and the two neighboring points). The CC points were calculated for incident angles between 20 and 87 degrees in the steps of 1/3 of a degree, and the averaging procedure should thus simulate the incident angle spread and the detector acceptance angle of $\sim 1^o$, in agreement with the experiment.

It can be seen that the theory and experiment compare exceptionally well. All the minima and maxima observed experimentally are very well reproduced by our calculation. The level of agreement is even comparable to that for He-Xe/graphite case, and thus we show that it is indeed possible to construct adequate He-surface potentials for surfaces consisting of chemisorbed atoms. The relative intensities are not reproduced entirely satisfactorily, as is always the case for this type of calculation which does not include the inelastic scattering channels and the incoherent scattering from surface imperfections (see section 3.1).

Figure 6.7 is of special importance since this measurement was speciffically and additionally performed by the authors of ref. [71] ³ to denote and mark the bound state resonances. In particular, they have assigned the most prominent feature of the experimental incident angle scan, which is the minimum around 68°, to the bound state resonance with the state at -13.7 meV. However, we show that this feature is not related to this process and that it can be reproduced with a much

³It also seems to be the most precise measurement in ref. [71] with the highest density of points.

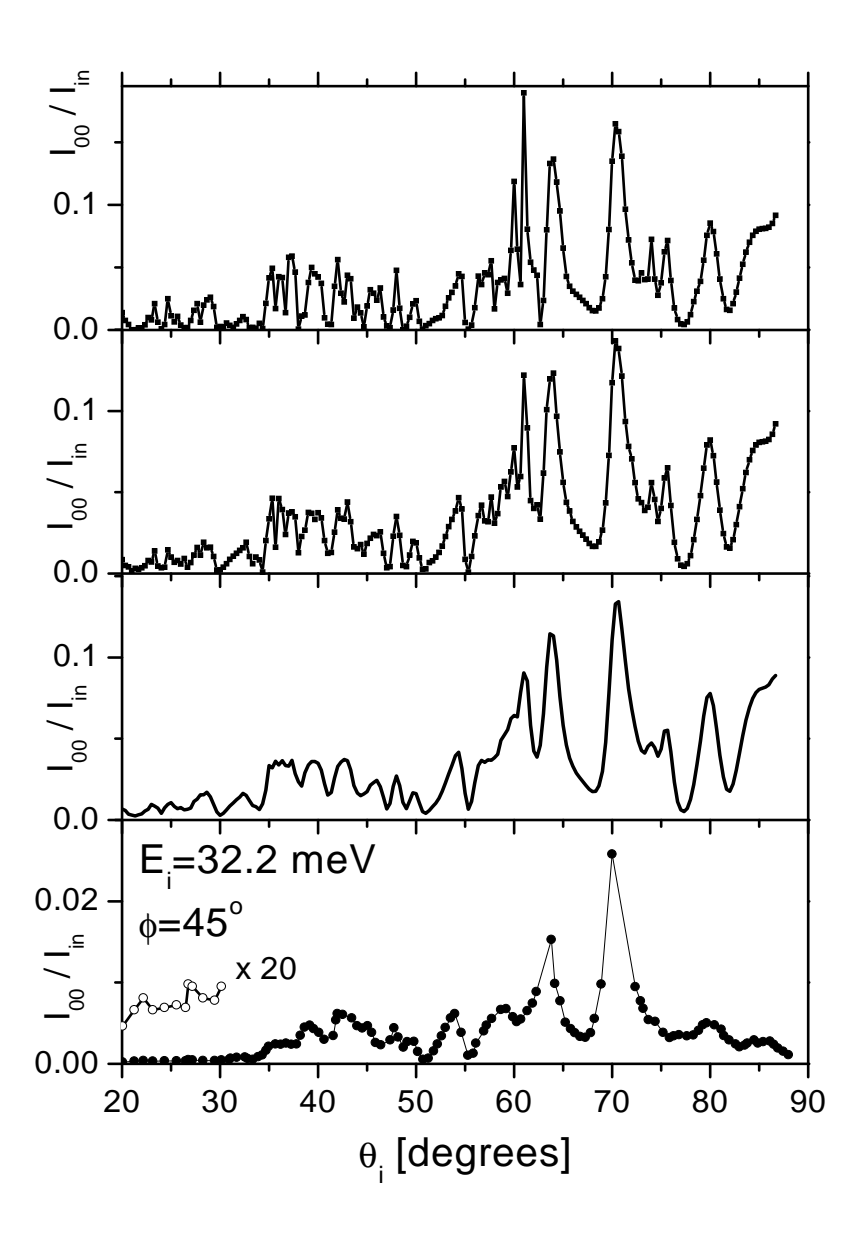


Figure 6.7: Experimental and theoretical incident angle scans (see text) for He-c(2 \times 2)Cl/Ag(001). $\phi=45^{o},~E_{i}=32.2~\mathrm{meV},~T_{S}=205~\mathrm{K}.$

shallower potential.

To further test the proposed potential, we have performed additional calculations for a number of different scattering conditions.

Figure 6.8 shows the results for higher He incident energy, $E_i = 63$ meV. The basis for the CC calculation was larger in this case $(n_{max} = 8)$ due to the higher He atom energy. The agreement is very good and all the experimental features are present in our CC calculation. The energy spread in this case is ~ 15 % of E_i (FWHM). The adjacent averaged CC spectrum was calculated in the same way as for $E_i = 32.2$ meV incident energy. The dashed line in the third panel is obtained from the full line in the third panel as $I_{dashed} = 4I_{full}\cos\theta_i$, which should account for the geometrical factor discussed in section 3.1.

Figure 6.9 displays the results for lower He incident energy, $E_i = 25$ meV. The energy spread in the CC results is ~ 6 % of E_i (FWHM), in agreement with the experimental incident energy spread. The agreement is somewhat worse than in the previous two cases, but it should be noted that all the features seen experimentally are reproduced in our calculation. Note also that the experimental data are less precise in this case than in the previous two ones and that the step in θ_i is larger.

6.2.3 Playing with shapes: Extending the CLMT-CD model from ellipses to "squares" and "stars"

It should be noted that the equipotential contours of the binary CLMTCD potential that correspond to an isolated adsorbate atom are circles in the xy (surface) plane. This needs not to be the actual situation - it is a consequence of a specific model potential used. In fact, according to Neckel [73], for the case of SOM model of Cl on Ag(001), the total electronic density contours should look like those sketched in fig. 6.10 4 . It is of interest to us to see whether the scattered helium atoms are sensitive to anisotropy of the binary potential which can be expected due to

⁴This figure is based on the calculations reported in reference [69] and here we quote the author's description of its features [73]. "From our calculations follows that the Cl-atoms form bonds to the 4 Ag-atoms lying in the plane below the Cl-atoms. This effect can be deduced from Fig. 4a, which displays the difference electronic density. One observes an accumulation of electronic charge at a Cl-atom in the directions towards neighboring Cl-atoms (due to the interactions of the Cl-atom with the Ag-atoms lying in the plane below). px- and py- like electronic density is built up, whereas pz- like charge density (below the Cl-atom) is removed."

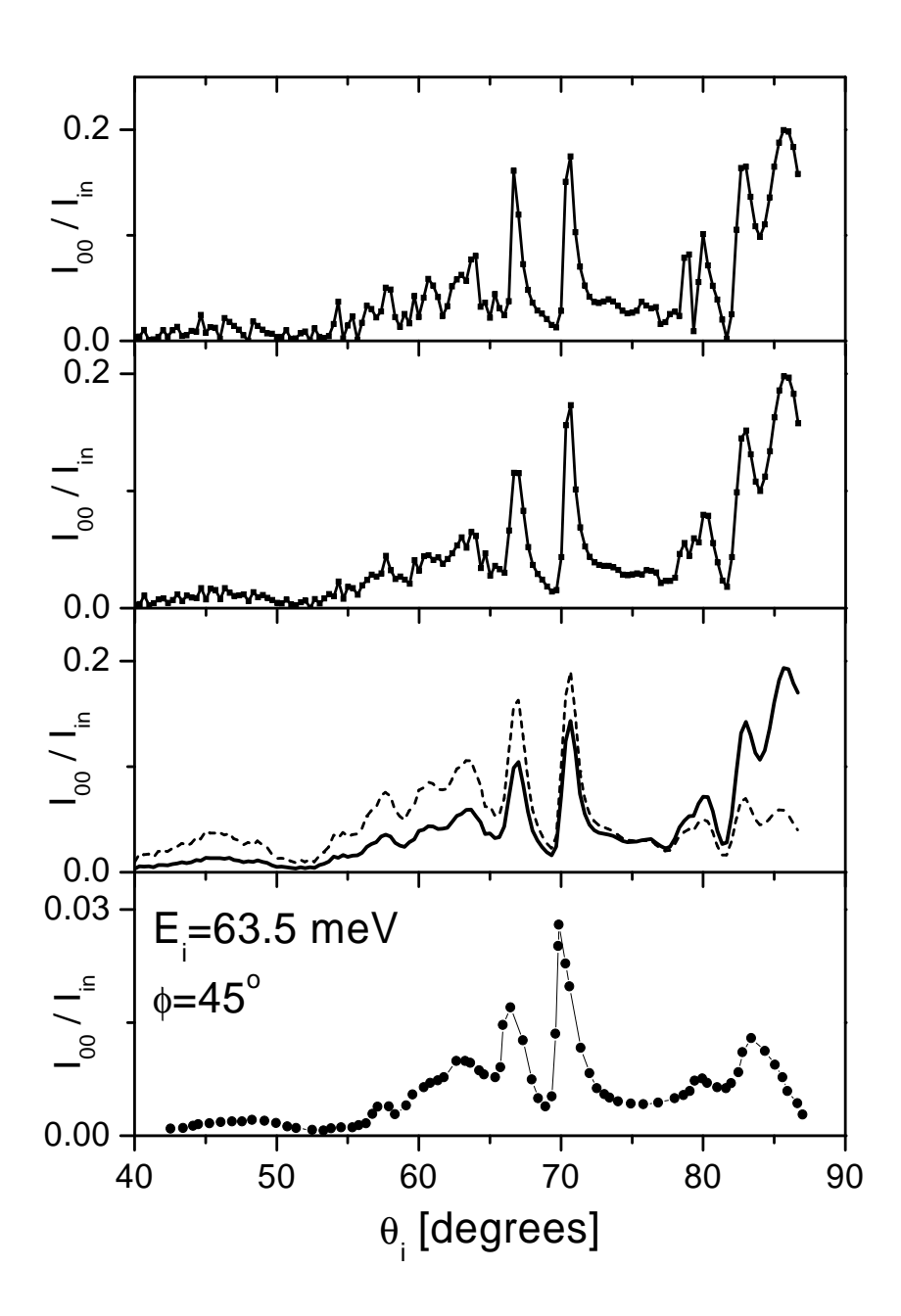


Figure 6.8: Same as in fig. 6.7 but for $\phi=45^o$ and $E_i=63$ meV. $T_S=205$ K.

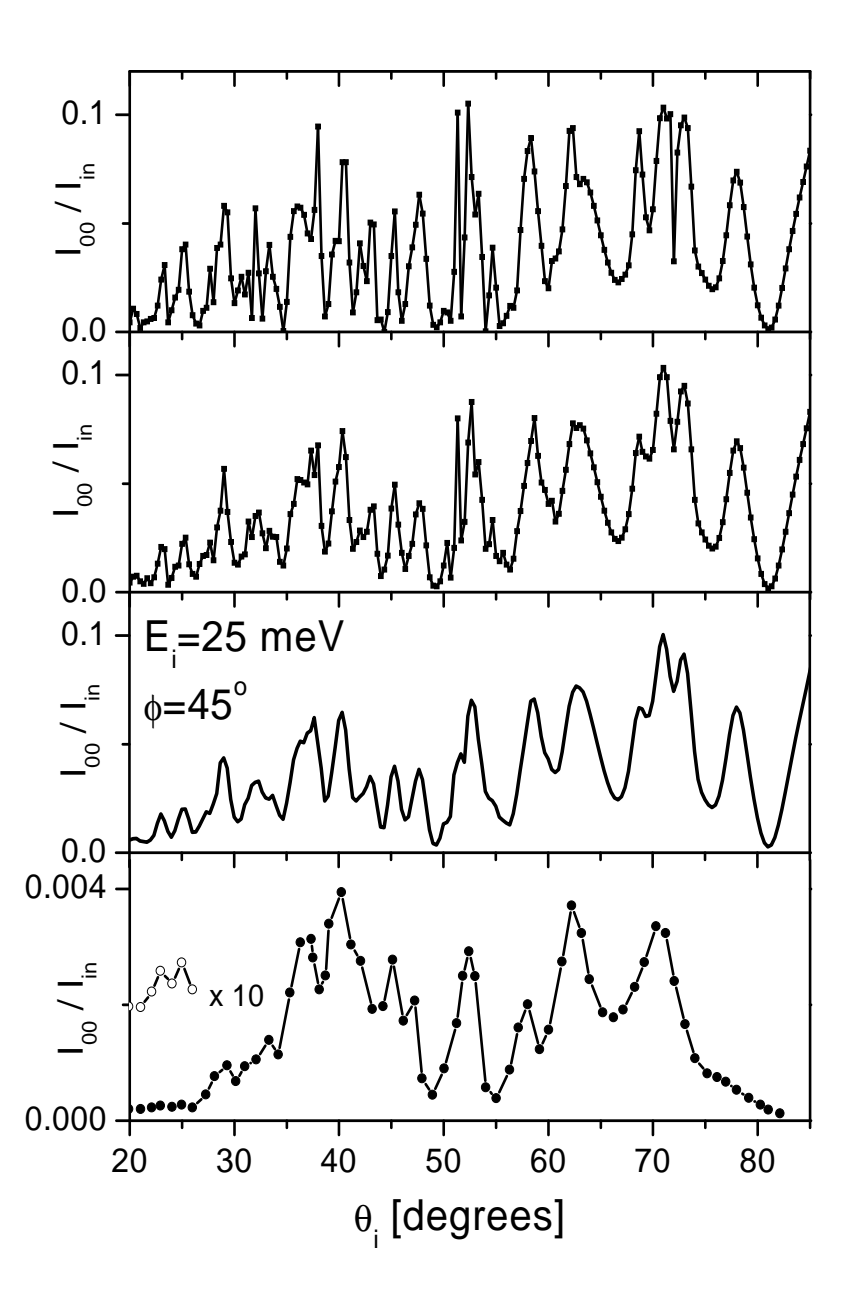


Figure 6.9: Same as in fig. 6.7 but for $\phi=45^o$ and $E_i=25$ meV. $T_S=205$ K.

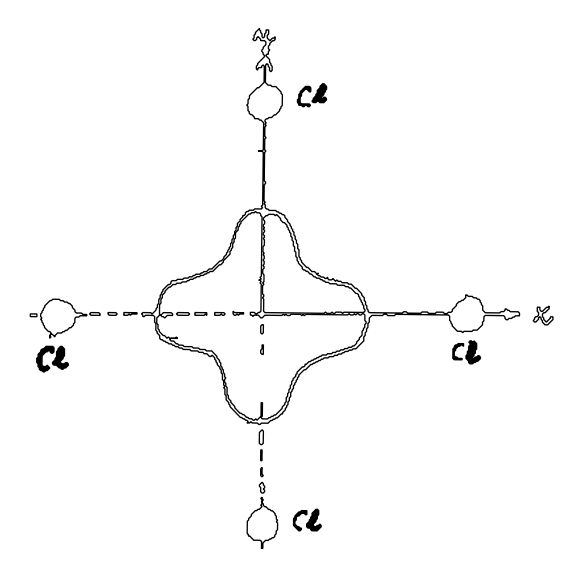


Figure 6.10: A sketch of the electronic density contours in the SOM Cl overlayer on Ag(001). One Cl atom is at the origin of the coordinate system.

the specific discrete geometry of both the substrate and the overlayer. Note that the use of equation (4.4), with $\eta_x \neq \eta_y$, is inappropriate in our system (c(2 × 2)Cl/Ag(001)) since it does not reflect its symmetry. However, a model electronic density (or the repulsive part of the binary potential) reflecting this symmetry can be constructed as

$$\rho_{tot}(\mathbf{r}) = \frac{P}{2} \eta_1 \eta_2 \sum_{l} [\exp(-b\sqrt{z^2 + \eta_1^2 x^2 + \eta_2^2 y^2}) + \exp(-b\sqrt{z^2 + \eta_2^2 x^2 + \eta_2^2 y^2})].$$
(6.6)

For $\eta_1 = \eta_2$ this model reduces to the "standard" CLMTCD potential. It can be easily seen that the maximum corrugation along the $\phi = 45^{\circ}$ direction in fig. 6.6 that is produced by this model density will be the same as in the original CLMTCD model if

$$2\eta^2 = \eta_1^2 + \eta_2^2, \tag{6.7}$$

where η is the ellipticity parameter of the original CLMTCD model. The corrugation along the $\phi = 0^o$ will be smaller than in the original CLMTCD model, the smaller as $|\eta_1 - \eta_2|$ increases. The equipotential contours of the model we propose are similar to those sketched in fig. 6.10.

The advantage of the proposed model potential is that it has analytic Fourier components as does its predecessor, the original CLMTCD potential. Since we have information on the electronic density along the $\phi = 45^{\circ}$ direction only, the lack of knowledge on the behaviour of the electronic density along other directions can be cast into the unknown coefficients η_1 and η_2 which are related by eq. (6.7).

The fact which motivated us to consider this model potential was a somewhat worse agreement between the theory and experiment for the experimental data taken along the $\phi = 0^{\circ}$ direction. The attempts to fit the experimental data with the model potential proposed in this subsection are shown in fig. 6.11. We did not account either for a finite incident energy spread or for finite incident angle spread in these calculations.

6.2.4 Additional comments on the He-Cl pseudopotential

One should note that we could definitely conclude from the electronic density calculations that the electronic density of Ag(001) substrate is not the same as for a clean Ag(001) surface. We have explicitly taken this into account by introducing the parameter f (see equation 6.3). However, we haven't scaled the attractive interaction of He-Ag(001) but taken it to be the same as if the Ag(001) substrate were clean. This is certainly not true and a more appropriate modification of this interaction is needed. If we were to modify the attractive part of this interaction, deeper He-Cl pseudopotential would be needed to reproduce the experimental data with comparable success. However, the total potential is very reliable.

6.3 $c(2 \times 2) CO/Cu(001)$

The structure of this system is sketched in fig. 6.12. The C-O and C-Cu distances were taken from ab-initio calculations (see subsection 6.3.2). They compare favourably with the values from other literature sources (see e.g. ref. [80]).

6.3.1 He-CO gas phase potential

The potential of interaction between He atom and CO molecule has been investigated since the early seventies and information on these

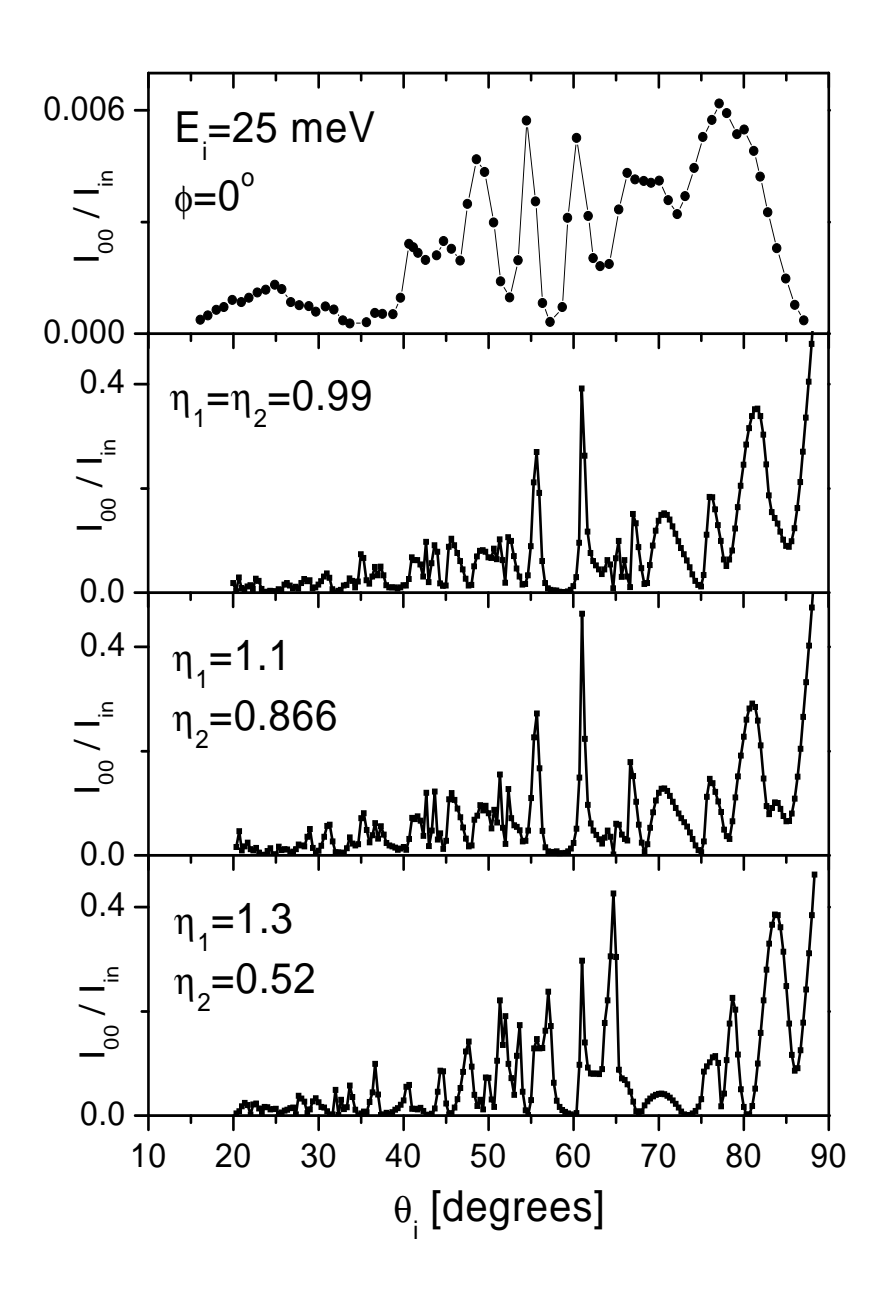


Figure 6.11: Top panel: Experimental data. Second, third and fourth panels from the top: CC results with different choices of η_1 and η_2 parameters (see text). $\phi = 0^o$, $E_i = 25$ meV and $T_S = 205$ K.

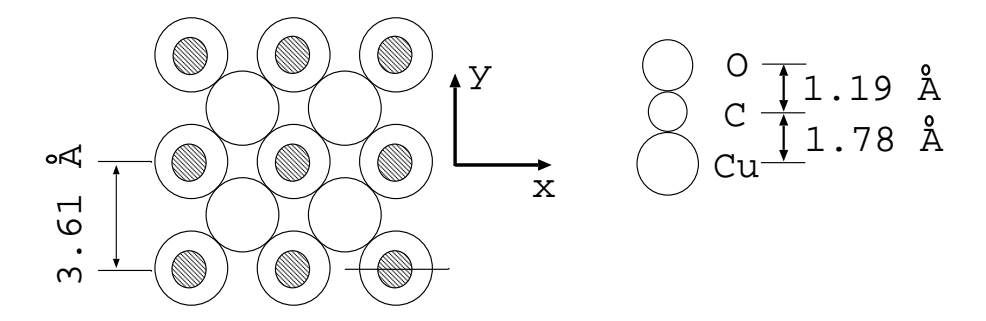


Figure 6.12: Geometry of $c(2 \times 2)$ CO/Cu(001).

early potentials can be found in ref. [82]. We concentrate here on somewhat more modern and presumably more precise potentials. We mention here the theoretical potential proposed by Thomas, Kraemer and Diercksen (the TKD potential) in ref. [83], the empirical V333 potential proposed by Chaqui *et al* in ref. [84] and the theoretical potential proposed by Tao *et al* in ref. [85].

6.3.2 He-adsorbed CO potential

To gain information on the repulsive part of He-CO/Cu(001) potential, self consistent Hartree-Fock type of calculation was performed for a finite cluster representing He, CO and Cu substrate. The total energy calculations were performed for different positions of He atom [15]. The Cu substrate was represented with 14 Cu atoms arranged in three layers in the z-direction, containing 5 (Cu layer closest to CO molecule),4 and 5 Cu atoms. The atoms were arranged in x and y direction according to the geometry of Cu(001) surface and subsurface layers. The CO distance above the surface was obtained by carrying out a geometry optimization on the MP2 level for the Cu-Cluster/CO complex. The calculations were carried out using Gaussian 98 [74] commercial software package with the following basis sets:

- 1) Cu 28 el Pseudopotential for Cu-Atoms except the one below the CO, as described in ref. [75].
- 2) 6-311G Basis Set for atom below the CO
- 3) 6-311G Basis Set for all other atoms (C,O,He)

Note that the potential does not reproduce the attractive part of the interaction and we have to additionally account for this.

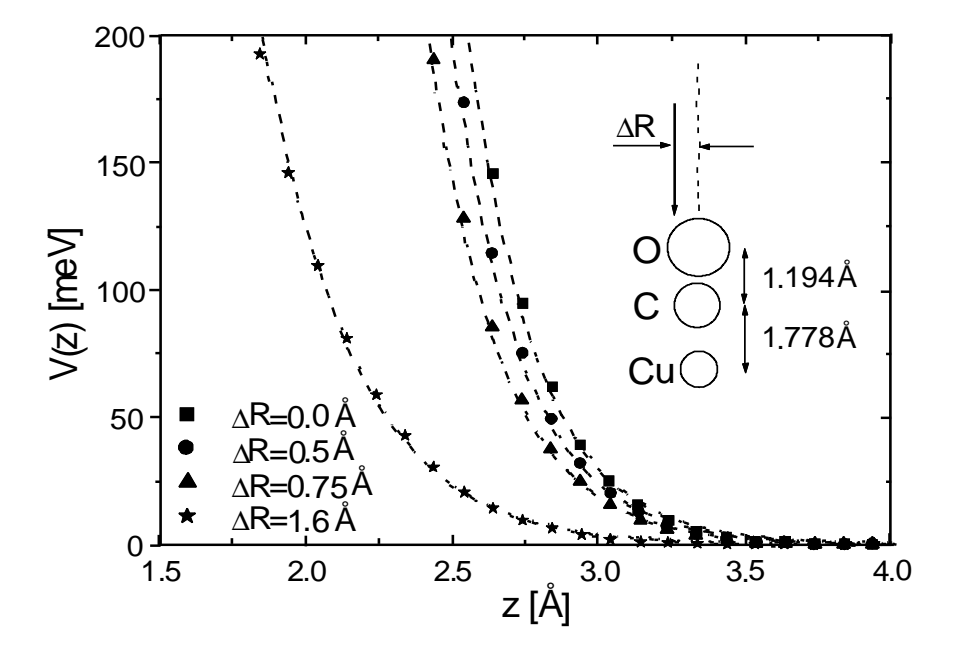


Figure 6.13: The He-CO/Cu₁₄ interaction potential in the Hartree-Fock approximation. Symbols: calculation. Dashed lines: CLMTCD model. Horizontal axis is the z-component of distance between He and the center of mass of CO molecule.

The dashed lines in fig. 6.13 represent the values of a model potential given as

$$v(x, y, z) = \eta^2 v_0 \exp(-b\sqrt{z^2 + \eta^2(x^2 + y^2)}), \tag{6.8}$$

with $v_0 = 8926$ eV, b = 4.27 1/Å and $\eta = 1.1$ ⁵. The fit with this type of the repulsive potential is not entirely satisfactory since the HF values significantly deviate from the expontential behaviour for v(x, y, z) < 10 meV. The fit with a gaussian profile of the site electronic density is very poor, due to the fact that this model does not account correctly for the fact that the repulsive potential becomes less steep for larger ΔR in figure 6.13.

The total potential was constructed as in section 4.2 with the repulsive part given by eq. (6.8).

 $^{^5} For$ metal surfaces, values of η smaller than one are always obtained. For adsorbed species, this needs not to be the case.

$(z, \Delta R)$ [Å]	(3.0, 0.0)	(3.25, 0.0)	(3.5, 0.0)	(2.77, 1.6)
$V_{HF}^{Taoetal} [\mathrm{meV}]$	32.1	11.0	3.7	9.3
$V_{HF}^{Thisstudy}$ [meV]	30.6	9.5	2.4	7.1

Table 6.3: Energies of the HF interaction for a He atom and a CO molecule in the gas phase (from reference [85]), and as found in this study for CO adsorbed on Cu_{14} cluster. z and ΔR variables are defined and discussed in connection with fig. 6.13.

Comparison of the repulsive parts of He-CO interactions for CO in the adsorbed and gas phase

In table 6.3 we compare the Hartree-Fock energies of the He-CO interaction calculated in this study for CO adsorbed on a Cu₁₄ cluster and of He-CO interaction in the gas phase according to reference [85].

From this comparison we see that the HF energies of the He-CO interaction in the gas phase and for CO adsorbed on Cu_{14} cluster are very similar, at least in the region where the strength of the potential does not exceed 50 meV. Thus, although one could expect a shift in the electronic density of CO adsorbate due to the partial occupation of the $2\pi^*$ orbital, and a corresponding shift in the repulsive part of He-CO interaction, this effect is seen to be of minor importance ⁶.

6.3.3 He-Cu(001) interaction potential

We have neglected the corrugation of this part of the interaction. Thus, this part was added to the zeroth order Fourier component of the total potential. The parameters of this potential were taken from ref. [78]. They correspond to He - clean Cu(001) interaction.

6.3.4 Comparison of the results of CC calculations with experimental results

There seems to be a very limited number of experimental investigations of this system which are of use for our purposes. The experimental results [76] relevant to our studies are displayed in fig 6.14. The author of ref. [76] claims that the oscillations in specularly scattered intensity

⁶This is in contrast to arguments presented in reference [102] and in agreement with reference [81].

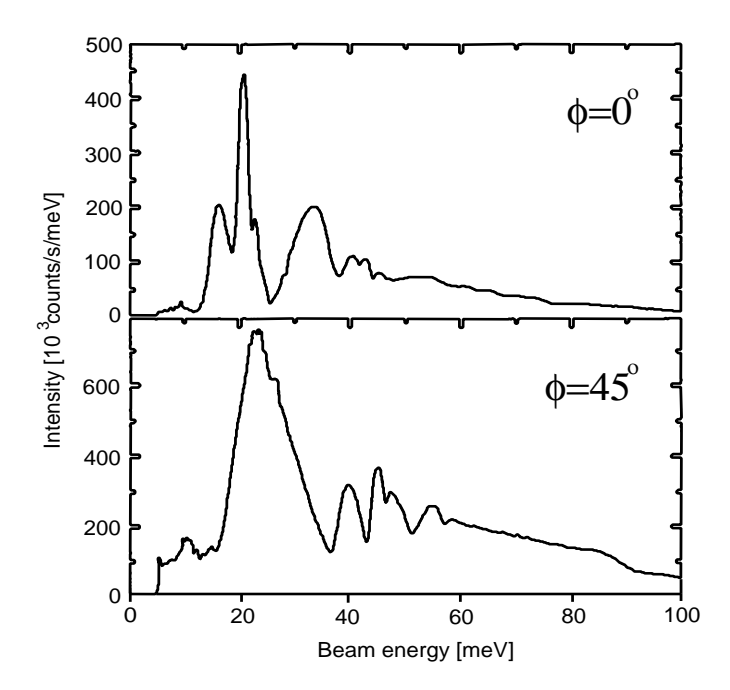


Figure 6.14: The experimental drift spectra for $c(2 \times 2)$ CO/Cu(001) system reproduced from reference [76]. $\theta_i = 47.9^{\circ}$, $T_S = 120$ K.

are due to selective adsorption resonances, however, at the first sight they seem to be much too wide to be attributed to this phenomenon. We presume that they are due to interference effects discussed in section 3.3.

We have tried to fit the experimental data with the potential constructed as a sum of binary He-adsorbed CO potentials given by the CLMTCD form with the repulsive part as in eq. (6.8), $\xi = 14.6$, and with C_6 treated as a fit parameter. The behaviour of this potential for br < 16.6 was extended to the whole range of r coordinate. The He-Cu(001) part of the potential was calculated as described in section 6.3.3.

The results of this investigation are presented in fig. 6.15. The best-fit C_6 constant was found to be 10450 meV Å⁶.

The third row of graphs are the experimental data [76] reproduced in fig. 6.15 for the sake of comparison. The first row of graphs represents the CC results which were transformed to yield the data presented in the second row, so as to account for a finite experimental resolution of the incident energy. It was assumed that $\Delta E_i/E_i = 2 \%$ 7 which is

⁷This means that the experimental data are much less sensitive to the details for higher incident energies of He atoms.

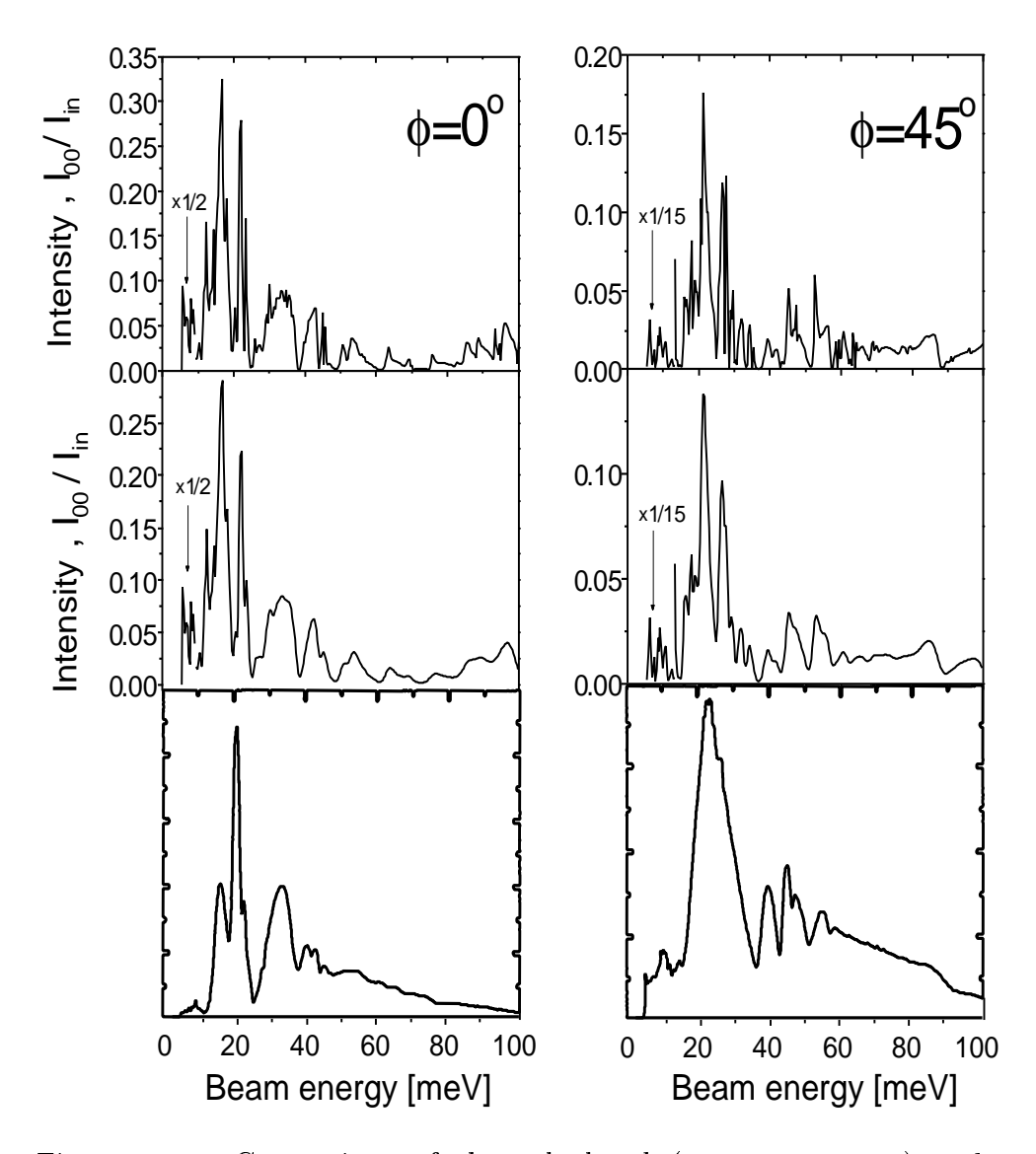


Figure 6.15: Comparison of the calculated (two upper rows) and measured (bottom row) drift spectra for He - c(2 × 2)CO/Cu(001), C_6 =10450 meV Å⁶, η =1.1. The two graphs in the second row were obtained from the corresponding graphs in the first row by accounting for the experimental energy resolution. $\theta_i = 47.9^{\circ}$.

a typical resolution for the type of HAS machines used in this experimental study.

It can be seen that the agreement is not entirely satisfactory. Some disagreements can be explained by the specificities of the experiment. In particular, the experimental intensity for $E_i < 20$ meV seems to be significantly smaller than the one predicted by the calculations. To facilitate comparisons, the theoretical data were scaled for low He energies as denoted in the figure. According to the author of ref. [76], the reflected intensity for smaller energies is reduced due to the condensation effects. It seems that this refers to the condensation effects in the He beam itself [77]. Additionally, it seems that the beam intensity is a function of the beam energy in this type of experiments [79], which was not accounted for in the calculations. However, the main experimental features are present in the calculations. For energies lower than 30 meV, even the smoothed calculations predict more structure than observed experimentally. In particular for $\phi = 45^{\circ}$, two peaks at ≈ 21.5 meV and ≈ 27 meV are predicted, whereas only a peak at ≈ 21.5 meV and a shoulder at ≈ 27 meV are observed in the experiment. Two small peak-like features at $\approx 31 \text{ meV}$ and $\approx 34 \text{ meV}$ are not observed experimentally.

It should be noted that there exists a possibility to obtain better agreement with the experiment by slightly relaxing the form of the repulsive part of the binary potential. In figure 6.16 we present the CC results with the same potential, in which η was varied from 1.1 to 1.05 and a much better account of the experimental data along the $\phi = 45^o$ azimuth is obtained. The shape of the features between 35 and 60 degrees is correctly reproduced. It is also possible that the electronic density of adsorbed CO is slightly anisotropic, even more so when the CO molecules are arranged in $c(2 \times 2)$ CO overlayer. The investigations of this effect are under way.

6.3.5 Additional information on the He - $c(2 \times 2)$ CO / Cu(001) interaction potential

To further illustrate the potential we have constructed, we plot in figure 6.17 the potential for He atom scattering from a *single* CO molecule adsorbed on the Cu(001) substrate.

The equipotential contours at 9.4 meV, 30.1 meV and 40.3 meV were specifically emphasised (dashed lines) in order to compare their geometry with the predictions of ref. [86]. The authors of this reference perform an exact quantum calculation for scattering of He atoms

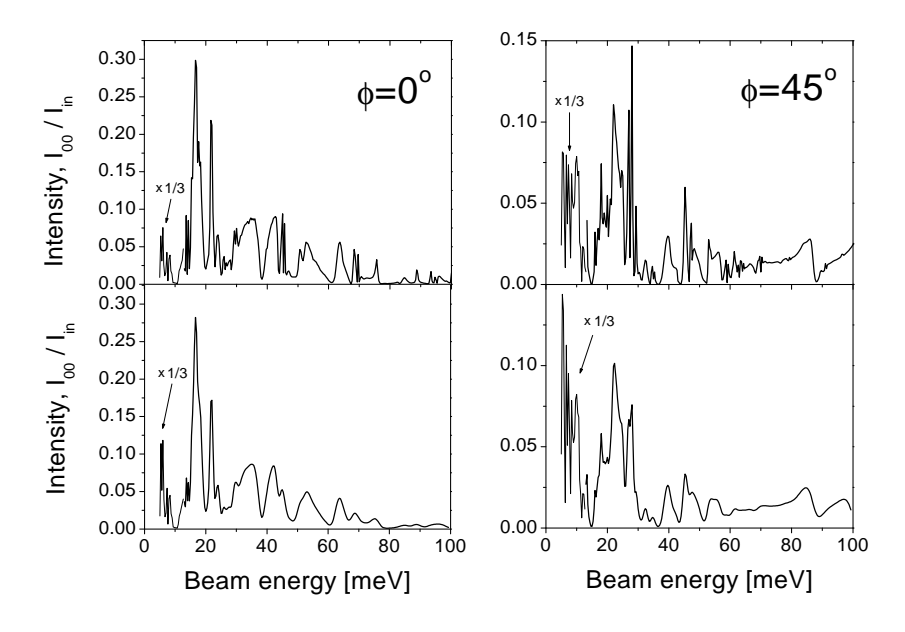


Figure 6.16: Calculated drift spectra for He - c(2 × 2) CO/Cu(001). $C_6=10450$ meV Å³, $\eta=1.05$. $\theta_i=47.9^o$.

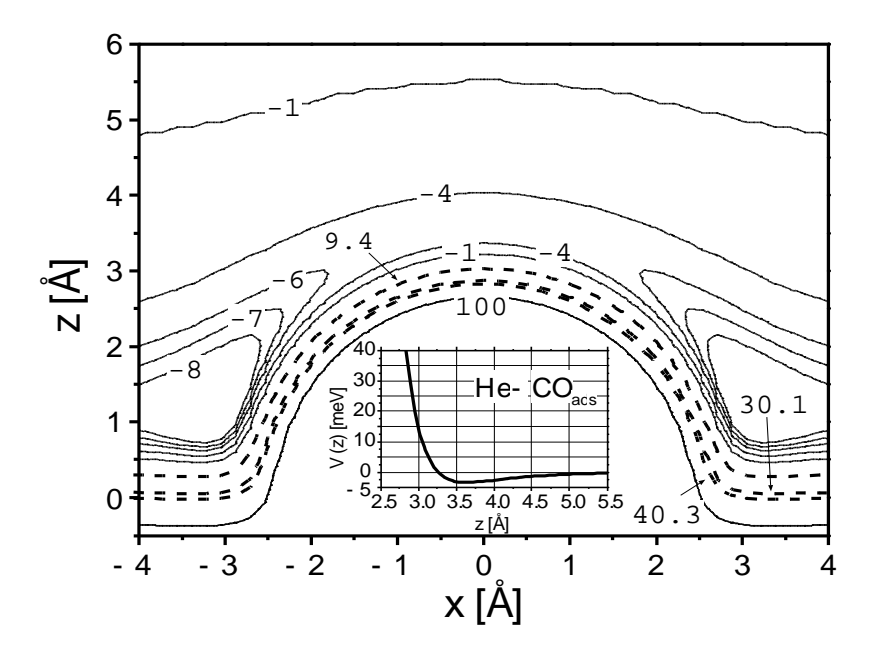


Figure 6.17: Interaction potential (in meV) for He atom scattering from a single CO molecule adsorbed on Cu(001) substrate. Inset: Binary He-adsorbed CO potential along z-axis (x=0). The influence of the Cu(001) substrate is not included in the inset.

from a hard hemisphere representing the adsorbed CO molecule. By comparing their results with the experimental data, they find the best fit hemispere radii (r_H) for different incident He atom energies. In particular, for $E_i = 9.4$ meV they find $r_H = 4.4$ Å, for $E_i = 30.1$ meV, $r_H = 2.8 \text{ Å}$, and for $E_i = 40.3 \text{ meV}$, $r_H = 2.4 \text{ Å}$. This should be compared with the radii of equipotential curves of the potential we obtain. For the same incident energies of He atom, we obtain $r_H \approx 3.05, 2.88$ and 2.81 Å, in fair agreement with the results of ref. [86] taking into account the approximations inherent to the approach of the authors of ref. [86], in particular the complete neglect of the attractive component of the interaction and the assumption of infinitely repulsive He-CO and He-Cu potentials at the classical turning point of the He atom (see also discussion in reference [91]). Another study [87] dealing with the hard-sphere radius of isolated CO on Cu(001), yielded for the same set of energies $r_H = 2.15, 2.35$ and 2.39 Å. The calculations were essentially based on an Eikonal approximation for scattering from a hard hemisphere.

We note that the effective binary He-adsorbed CO potential has a well depth of D=3.4 meV, and the minimum of the potential is positioned at $z_m=3.66$ Å. The interaction of He with CO adsorbed onto Cu(001) has been calculated in references [6, 10, 89]. For He atom approaching the CO molecule along the z axis, their expressions for the attractive part of the binary He-CO interaction reduce to

$$V_{att}(z) = -\frac{2C_{ab}}{z^6}(2+\mu)$$

$$-\frac{2C_{aMbM}}{(z+2d)^6}(2+\mu)$$

$$-\frac{4C_{abM}}{[z(z+2d)]^3}(1+4(1-\mu)), \qquad (6.9)$$

where $\mu = \alpha_{xx}(\omega)/\alpha_{zz}(\omega)$ is the ratio of CO polarizabilities in z and x directions and d is the distance between the center of mass of the CO molecule and the topmost substrate crystal plane. The other parameters of interaction were taken from ref. [10]. These parameters should also include the effect of charge transfer from Cu to $2\pi^*$ orbital of CO. The parameters are: $C_{ab} = 1506$ meV Å⁶, $C_{aMbM} = 555$ meV Å⁶, $C_{abM} = 816$ meV Å⁶, $\mu = 0.62$. The thus constructed attractive part of He-adsorbed CO interaction was added to the repulsive part in eq. (6.8). We call this potential the GL potential. The comparisons of various He-CO potentials for CO both in the gas phase and in the adsorbed phase are summarized in table 6.4.

Potential		$D [\mathrm{meV}]$	z_m [Å]
TKD (gas phase)	[83]	2.05	3.79
Tao et al (gas phase)	[85]	2.38	3.73
V333 (gas phase)	[84]	2.72	3.65
GL (CO/Cu(001))	[11]	1.88	3.77
MGL (CO/Cu(001))	-	3.11	3.63
Liu and Gumhalter (CO/Cu(001))	[90]	3.6	3.4
This study $(CO/Cu(001))$	-	3.40	3.66

Table 6.4: The well depths and the positions of the minimum of various He-CO potentials

It is seen that the potential we propose is deeper than all the potentials proposed for the He-CO interaction in the gas phase. The well depth of the GL potential is surprisingly small, even smaller than for the potentials proposed for the interaction in the gas phase. The reason for this is a neglect of C_7 terms in the He-CO interaction which seem to be of importance according to references [84] and [85]. We added these terms to the GL potential using the C_7^1 and C_7^3 values suggested in ref. [84]. We call this potential modified GL potential (MGL) and it can be seen in table 6.4 that its well depth is indeed much deeper and closer to the number we find in our study. However, the GL potential needs to be reconsidered in the view of the more precise number for μ parameter which in recent studies [88, 84, 85] was found to be $\mu \approx 0.78$ rather than 0.62 as supposed by Lovrić and Gumhalter. Additionally, it seems that the substrate induced contribution to C_7 and higher multipole constants of attractive interaction might be also of importance. The potential which approximately includes the effects of chemisorption and higher multipole interactions was suggested by Liu and Gumhalter in reference [90] (see also reference [11]). From table 6.4, this potential is seen to be fairly similar to the potential we propose.

6.3.6 Test of the He-CO/Cu(001) potential in the case of a dilute CO overlayer

The scattering from isolated adsorbates can be also treated within a framework of coupled channel calculations. However, the usual choice of the coordinate system is spherical rather than Cartesian as in our case. In fact, the case of a single adsorbed molecule is a bit tricky con-

cerning the best coordinate system one should use: On the one hand, the geometry of the substrate suggests the Cartesian system and, on the other, the geometry of an isolated adsorbate suggests the spherical coordinate system. When one decides to use the spherical coordinate system, the projectile-substrate potential must be very simplified to be treated in spherical coordinates. Very often, the substrate is represented as an infinitely repulsive, hard wall, and the component of the projectile - substrate attractive interaction is treated only as Beeby's correction to the projectile incident energy [36, 86]. This is not an approach which can be expected to yield any precise results.

We suggest another approach. We treat the problem of isolated adsorbate as a very dilute, ordered overlayer of adsorbates. We argue that in the limit when the overlayer lattice constant tends to infinity, this reproduces the case of an isolated adsorbate. This approach is prefered for several reasons:

- (i) There are no problems associated with the representation of the potential in spherical coordinates. We can use the potential models described in the previous chapters.
- (ii) The projectile-substrate interaction can be represented by a realistic potential model. There is no need for a hard wall assumption.
- (iii) Experimentally, one always deals with low but finite coverage of adsorbates, although the dilute adsorbate overlayer is probably poorly ordered. Our approach naturally includes the finite coverage of adsorbate atoms/molecules.

Of course, there are problems which are not encountered in the representation of scattering in the spherical coordinate system:

(i) - As the lattice constant of the overlayer becomes larger, the basis vectors in the inverse space become smaller and the number of open scattering channels rapidly increases (see equation (2.5)). Thus, a large number of channels must be included in the CC calculations and we can expect to cover only the case of only a moderately low coverage overlayer. Nevertheless, this might be a fair representation of the isolated adsorbate case. Futhermore, for lower incident energies, the lower coverage overlayers can be treated.

- (ii) The experimental data on the isolated adsorbate systems are taken in such a way that one essentially measures diffraction scans (see section 3.1) ⁸. In this case, however, for every substrate tilt angle a finite intensity is recorded since an isolated adsorbate is a source of arbitrary parallel momentum. In our approach we still reproduce a finite intensity only for a discrete set of tilt angles, and as the overlayer lattice constant becomes larger, the set of angles becomes larger as well.
- iii As the minimum parallel wave vector transfer is finite and fixed by our choice of the overlayer lattice constant, we expect our results to be qualitatively and perhaps quantitatively correct to describe the phenomena which occur for *large* parallel wave vector transfers. We do not expect to correctly describe phenomena which occur at distances which are comparable to the overlayer lattice spacing.

Due to the problems associated with this approach we must adapt it before making comparison with experiments. In particular, we have to calculate the Jacobian transformation which transforms our discrete transition probabilities into a continuous quantity, $dN/d\Omega$, representing a number of particles scattered into an element of the solid angle Ω . We note that the transition probabilities $|S_{\mathbf{G},0}|^2$ can be transformed into a scattering spectrum as

$$N(\Delta K_x, \Delta K_y) = \frac{1}{g^2} |S_{\mathbf{G}',0}|^2,$$
 (6.10)

where $\Delta K_x < G_x' + g/2$ and $\Delta K_x > G_x' - g/2$ and similarly for ΔK_y . Here, $g = 2\pi/a$, where a is the length of the basis vector of the square adsorbate lattice. Note that

$$\sum_{\mathbf{G}'} g^2 N(\Delta K_x, \Delta K_y) = 1, \tag{6.11}$$

which is a discrete analogon of the unitarity property

$$\int \int d\Delta K_x d\Delta K_y N(\Delta K_x, \Delta K_y) = 1.$$
 (6.12)

We pass from ΔK_x and ΔK_y variables to $\Delta \Omega = \sin \theta d\theta d\phi$ (increment of the space angle) and instead of a simple uniform distribution of

 $^{^{8}}$ One should also note that the sum of the incident and final angle of scattering with respect to the z-axis is fixed in this type of experiment.

intensity within $\Delta\Omega = \frac{g^2}{k_i^2 \cos \theta_{\mathbf{G}'}}$ (as in eq. (6.10)), we assume a Gaussian distribution with the widths related to $\Delta\phi$ and $\Delta\theta$ components of $\Delta\Omega$.

Finally, for the number of particles scattered within an element of the solid angle, we obtain

$$\frac{dN}{d\Omega} = \sum_{\mathbf{G}} |S_{\mathbf{G},0}|^2 \frac{1}{2\pi\theta_w \phi_w \sin \theta} e^{-\frac{(\theta_{\mathbf{G}} - \theta)^2}{2\theta_w^2}} e^{-\frac{\Delta\phi^2}{2\phi_w^2}}, \tag{6.13}$$

where

$$\Delta \phi = |\phi_{\mathbf{G}} - \phi|, \quad |\phi_{\mathbf{G}} - \phi| < \pi,$$

$$\Delta \phi = 2\pi - |\phi_{\mathbf{G}} - \phi|, \quad |\phi_{\mathbf{G}} - \phi| > \pi,$$
(6.14)

and

$$\theta_w = \frac{g}{2k_i \cos \theta_{\mathbf{G}}},$$

$$\phi_w = \frac{g}{2k_i \sin \theta_{\mathbf{G}}}.$$
(6.15)

 $\theta_{\mathbf{G}}$ and $\phi_{\mathbf{G}}$ are the angles associated with the final direction of projectile atom diffractively scattered into a channel characterised by the wavevector \mathbf{G} that is one of the vectors associated with the representation of the overlayer structure in inverse space. Note that

$$\lim_{q \to 0} \int d\Omega \frac{dN}{d\Omega} = 1, \tag{6.16}$$

as it should be.

The experiments do not "see" $d\Omega \frac{dN}{d\Omega}$, but rather

$$I_{exp} \sim \int_{\theta-\theta_e}^{\theta+\theta_e} \int_{\phi-\phi_e}^{\phi+\phi_e} d\theta d\phi \sin\theta \frac{dN}{d\Omega},$$
 (6.17)

where $2\theta_e$ and $2\phi_e$ are detector acceptances in the angles θ and ϕ . The quantity we compare with experiments is thus

$$I_{exp}(\theta, \phi) = C \sum_{\mathbf{G}} |S_{\mathbf{G},0}|^2 \frac{1}{2\pi\theta_w \phi_w} e^{-\frac{(\theta_{\mathbf{G}} - \theta)^2}{2\theta_w^2}} e^{-\frac{\Delta\phi^2}{2\phi_w^2}}, \tag{6.18}$$

where $C \sim 4I_{in}\theta_e\phi_e$ is a constant depending on the experimental parameters.

In figure 6.18 we present the comparison of the experimental data (first panel) from reference [87] with our CC calculations. The angle between the detector and source arms is fixed and equal to 95.8 degrees.

In CC calculations presented in the second panel, only open channels were included in the \overline{W} matrix. The CO molecules were positioned on a square lattice with a lattice parameter of 12.56 Å. In this calculation, the parameters determining the CC basis were $E_{min} = 0$ and $n_{max} = 36$. The scattering is along $\phi = 45^{\circ}$ azimuth. In CC calculations presented in the third panel, the CO molecules were arranged in a square lattice with a lattice parameter of 7.95 Å. In this calculation we take $E_{min} = -10$ meV and $n_{max} = 33$. The same calculation was repeated for $\phi = 0^{\circ}$ and the results are shown in the fourth panel. Strong oscillations in the intensity observed in the third and fourth panel are due to selective the adsorption resonances. The position of these resonances are determined by the choice of the lattice parameter and should be treated as an artefact of the calculations that reflects the periodicity of the system which is not realized in experiments. This is why we smoothed (thick lines in third and fourth panels) the calculated data (symbols) by adjacent averaging of 5 calculated points. This procedure should partially remove the selective adsorption related artefacts. Due to the problem with the selective adsorption resonances, we also performed a CC calculation which does not include the closed channels (second panel). In several aspects, this calculation produces the best agreement with the experimental data. Additional reason for this could be that in this calculation the lattice constant was largest⁹. All the intensities are calculated as a function of parallel momentum transfer which can be easily related to incident and final angles of scattering, θ_i and θ_f , respectively [87].

In figure 6.19 we present the experimental data from reference [87] (first panel) and the results of two CC calculations with $E_{min} = -10$ meV, $n_{max} = 35$. The lattice constant in these caclulations is 11.42 Å. The agreement is far from perfect and it is obvious that the calculations along two different azimuths, $\phi = 0^{\circ}$ and $\phi = 45^{\circ}$, are not the same, so that the results are still influenced by the periodicity of CO overlayer. Nonetheless, the approach seems promissing. If the overlayer systems with larger lattice constant could be examined, the agreement with the experiments should improve. Furthermore, it seems better not to include closed channels in these calculations since they give rise to selective adsorption resonance induced artefacts. This type of calculation was not performed in this case ($E_i = 30.10$ meV) since extremely

⁹Due to the exclusion of closed channels, we could examine an overlayer structure with larger lattice constant. The total number of channels was essentially the same as in the calculations which do include closed channels but relate to the structures with smaller lattice constant.

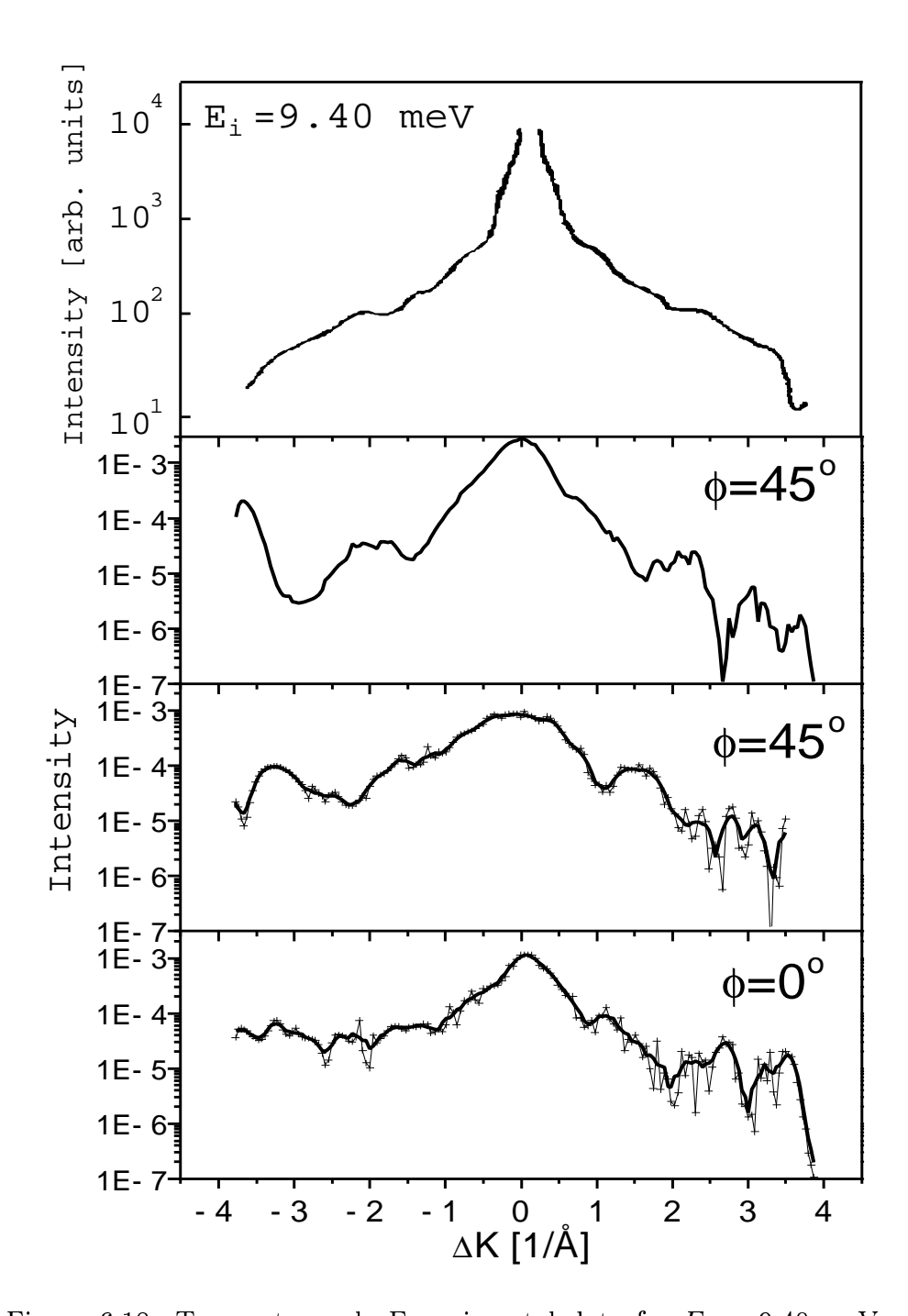


Figure 6.18: Topmost panel: Experimental data for $E_i = 9.40$ meV. Second topmost panel: CC calculation without closed channels, $\phi = 45^{\circ}$. Third panel: CC calculation, $\phi = 45^{\circ}$. Bottom panel: CC calculation, $\phi = 0^{\circ}$

long times are demanded to propagate the CC equations with large \overline{W} matrices ¹⁰.

6.4 $(\sqrt{3} \times \sqrt{3})$ R30° CO/Rh(111)

The structure of this system is sketched in fig. 6.20. The C-O and C-Rh distances were taken from the LEED analysis reported in reference [92].

6.4.1 He-adsorbed CO interaction potential

Unfortunately, we neither have any information on the He - CO/Rh(111) potential, nor are we aware of any literature source in which this potential has been studied and discussed. However, we may suppose that the repulsive part of this potential is not much different from the corresponding part of the potential in the system He - CO/Cu(001). As in the case of He-CO/Cu(001), we fit the attractive part of the potential by using the CLMTCD form of the binary potential.

6.4.2 He-Rh(111) interaction potential

The C_3 constant of long-range interaction is known from the literature [93]. We have taken $C_3 = 255$ meV Å³ in agreement with calculations of Lovrić and Gumhalter [95]. Since the coverage of $(\sqrt{3} \times \sqrt{3})$ R30° CO/Rh(111) overlayer is low, the repulsive interaction of He with the Rh(111) substrate must be accounted for. We have fitted this part of the interaction to the exponentially repulsive form in such a way that the total potential reproduces a sequence of bound state energies measured for the He-Rh(110) interaction. The He-Rh(110) and He-Rh(111) potentials should be very similar [78]. The range of the repulsive part has been set to $\beta = 2.57$ 1/Å, which is the same as the range of the repulsive part of the effective He-Rh binary potential reported in ref. [93]. The total He-Rh(111) potential is given as

$$V_{He-Rh(111)}(z) = A \exp(-\beta z) - \frac{C_3}{(z+d)^3},$$
(6.19)

with A = 129 meV and d = 1.436 Å. The origin of the z-axis is at the center of mass of the CO molecule.

 $^{^{10}}$ The calculations for $E_i = 30.10$ meV include ~ 700 channels.

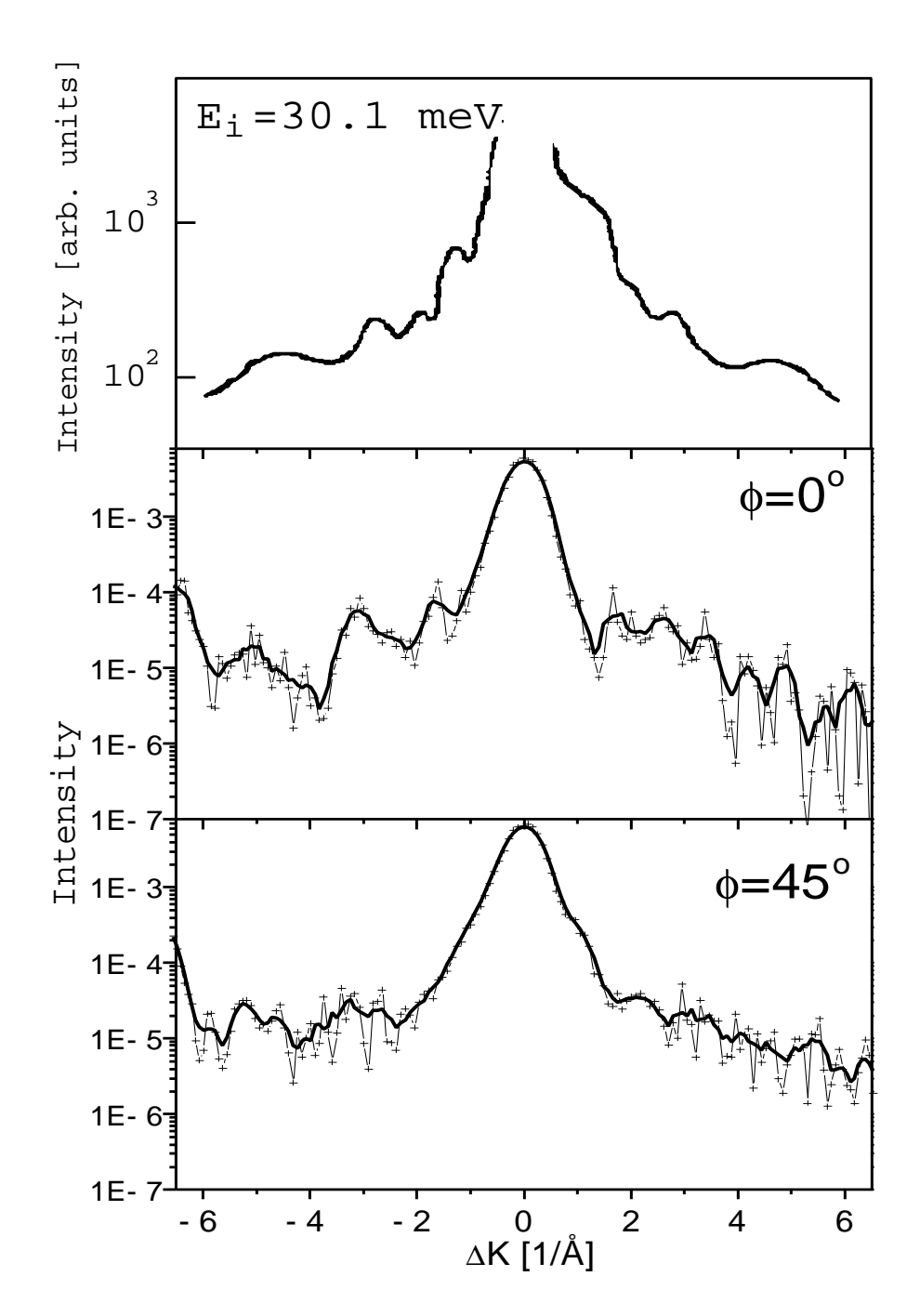


Figure 6.19: Topmost panel: Experimental data for $E_i = 30.10$ meV. Second topmost panel: CC calculation, $\phi = 0^{\circ}$. Bottom panel: CC calculation, $\phi = 45^{\circ}$.

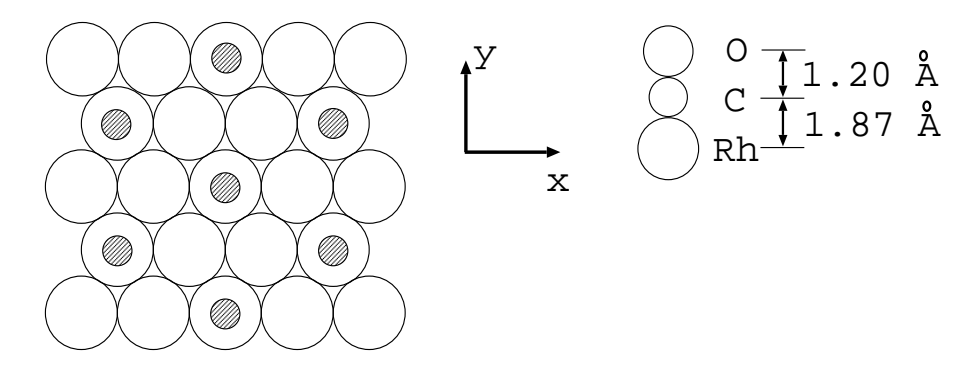


Figure 6.20: Geometry of $c(\sqrt{3} \times \sqrt{3})$ CO/Rh(111).

6.4.3 Comparison of the results of CC calculations with the experimental results

Unfortunately, the CC calculations could not quite satisfactorilly reproduce the experimental azimuthal scan published in ref. [96].

The CC probabilities are calculated according to equation (3.7) by taking the FWHM of the incident energy distribution to be equal to 1.1 % of the incident energy [100].

As can be seen from figure 6.21 the agreement is relatively poor. In particular, a very pronounced structure observed in CC calculations for ϕ between 0 and 13 degrees is not present in the experimental azimuthal scan, although some rough agreement does exist (the structure at 10 degrees and the two structures at 8 and 6.5(5.5) degrees). The most striking point of disagreement is a very pronounced minimum at 13 degrees in the CC calculations, which is seen as a rather shallow minimum at ≈ 11.5 degrees in the experimental scan. The best fit C_6 parameter we obtain is $C_6 = 9000$ meV Å⁶ with the ξ parameter of the CLMTCD potential set to 14.6. The attempts to obtain a better agreement with the experimental data with another choice of ξ parameter have proven unsuccessful.

The possible reason for this disagreement could be that the $(\sqrt{3} \times \sqrt{3})$ CO/Rh(111) structure might be very difficult to prepare [97, 98]. In particular, the author of ref. [98] has observed a significant decay of the diffraction peaks characterising the well ordered $(\sqrt{3} \times \sqrt{3})$ R30° CO/Rh(111) only 3 hours after the preparation of the sample ¹². This

¹¹The azimuthal angle, ϕ is measured with respect to the x-axis in fig. 6.20.

 $^{^{12}}$ In connection with this I may cite G. Witte [97]: "I prepared the $\sqrt{3} \times \sqrt{3}$ CO structure by dosing CO at room temperature. After the partial CO pressure had dropped to less than 1e-9 mbar I started cooling the sample to about 120 K in order

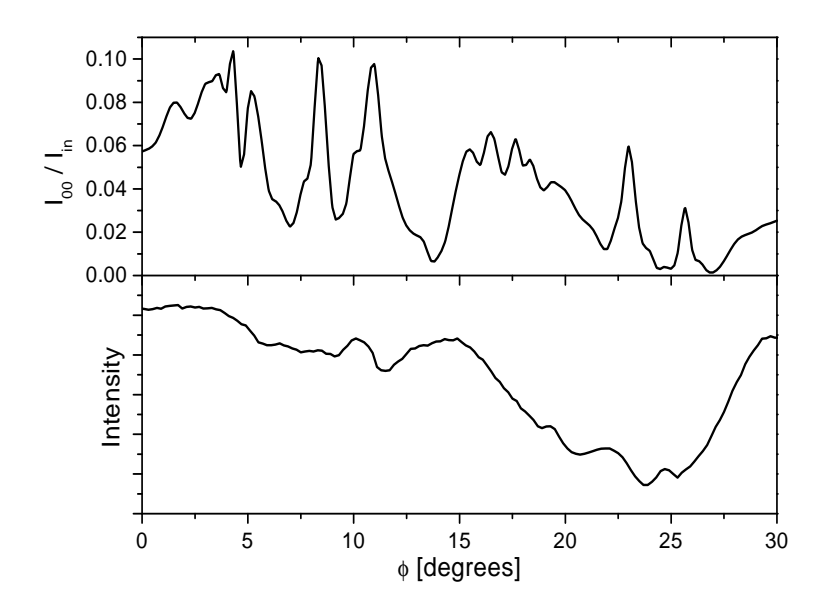


Figure 6.21: Upper and lower panel display the best fit theoretical and the experimental azimuthal scan for He - $(\sqrt{3} \times \sqrt{3})$ R30° CO/Rh(111) system. $C_6 = 9000$ meV Å⁶, $\xi = 14.6$. $E_i = 19.0$ meV, $\theta_i = 55^\circ$. $T_S = 150$ K.

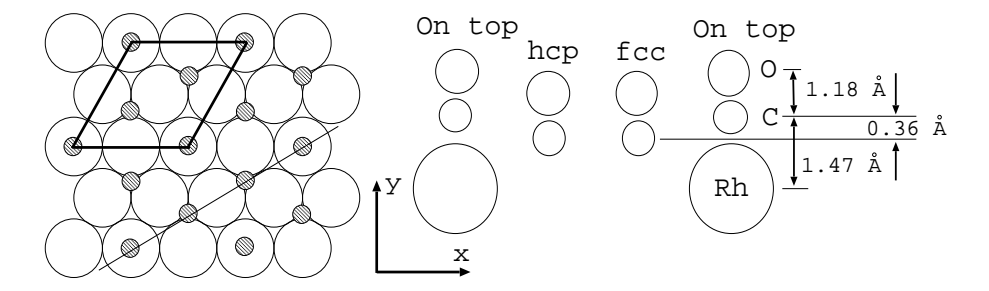


Figure 6.22: The structure of $c(2 \times 2)3CO/Rh(111)$ overlayer. The paralelogram represents the surface unit cell.

may easily influence the experimental azimuthal scans for which long acquisition times were needed.

The effective binary He-CO_{ads} potential has a well depth of 2.71 meV, and its minimum is positioned at $z_m = 3.66$ Å, as measured from the center of mass of the CO molecule.

6.5 $c(2 \times 2)3CO/Rh(111)$

The structure of the system is presented in figure 6.22. This structure is more dense than the $(\sqrt{3} \times \sqrt{3}) R30^{\circ} CO/Rh(111)$ structure. It is also more complex since there are three nonequivalent CO adsorption sites denoted by "On top", "fcc" and "hcp" in fig. 6.22. The distances were taken from ref. [92] except for the height differences between the CO molecules (0.355 Å) which was taken to be the mean value of the distances reported in references [92] and [101]. This distance is especially important for the corrugation profile of the He- $c(2 \times 2)3CO/Rh(111)$ potential. This structure could in fact be treated as a buckled surface with the formalism developed in subsection 2.6.2, however, there is no need for this since the unit cell (the paralelogram in fig. 6.22) is quite small and the potential can be easily set up using equation (2.21). The calculations are more time consuming relative to the calculations for monoatomic surface unit cells, due to an additional sum in equation

to perform the TOF/WIN measurements. After about 3-4 h the CO structure had been significantly degraded and a mixture of $\sqrt{3} \times \sqrt{3}$ and 2×2 could be observed in the angular distributions. This is clear evidence that a CO partial pressure of about 5e-10 mbar is still to high to suppress the formation of 2×2 islands on a time scale of several hours. So you might carry out some decent angular distributions but after 3-4 TOF spectra (with a gate time of 40 min each spectrum) you will measure a mixed phase except you can reduce the pressure a further order of magnitude. So it is rather an experimental problem than a physical instability of the system."

(2.21) which has to be performed when the potential (\overline{W}) matrix is set up.

The He-adsorbed CO potential was constructed as in the case of $(\sqrt{3} \times \sqrt{3}) \text{R} 30^{\circ} \text{ CO/Rh} (111)$ structure i.e. its repulsive part has been set to be equal to the He-CO/Cu(001) potential. The total He-adsorbed CO binary potential was represented by the CLMTCD form with the C_6 coefficient as a fit parameter. The ξ parameter of the CLMTCD potential was set to $\xi = 14.6$. The He-Rh(111) potential is the same as in the case of $(\sqrt{3} \times \sqrt{3}) \text{R} 30^{\circ} \text{ CO/Rh} (111)$ structure.

6.5.1 Comparison of the results of CC calculations with experimental results

In principle, there are three nonequivalent He-adsorbed CO interactions due to the fact that there are three nonequivalent CO adsorption sites. Two of these potentials (He-CO_{hcp} and He-CO_{fcc}) are expected to be very similar, but different from the third one (He-CO_{top}). However, treating all of these potentials separately, using different potential parameters is difficult. Therefore, we make an approximation that the He-CO_{ads} potentials are the same for all three nonequivalent CO adsorption sites. This leaves only the C_6 coefficient as a fit parameter, since the repulsive part of the binary He-CO_{ads} potential has been fixed and $\xi = 14.6$. The comparison of the results of CC calculations with experimental azimuthal scan reproduced from ref. [96] is presented in fig. 6.23.

The CC calculations were again performed by accounting for FWHM of the incident energy distribution of 1.1 % of the incident energy. It can be seen that the agreement is much better than in the case of He- $(\sqrt{3} \times \sqrt{3})$ R30° CO/Rh(111), which is surprising since we are dealing with a much more complex system here. This is an additional argument in favor of our assumption that the $(\sqrt{3} \times \sqrt{3})$ R30° CO/Rh(111) might be poorly ordered ¹³. The best fit C_6 constant (with $\xi = 14.6$) was $C_6 = 10650$ meV Å⁶, which is significantly larger than in He- $(\sqrt{3} \times \sqrt{3})$ R30° CO/Rh(111) system. Equipotential contours of the potential we propose are presented in fig. 6.24. The well depth of zeroth order Fourier component of the total potential is 12.91 meV and the position of the potential minimum is at $z_m = 3.1$ Å, measured from

 $^{^{13}}$ Another reason for poor agreement between the CC results and experimental data for the He- $(\sqrt{3} \times \sqrt{3})$ R30° CO/Rh(111) scattering system could be a greater importance of inelastic scattering for systems with larger corrugation (see appendix B).

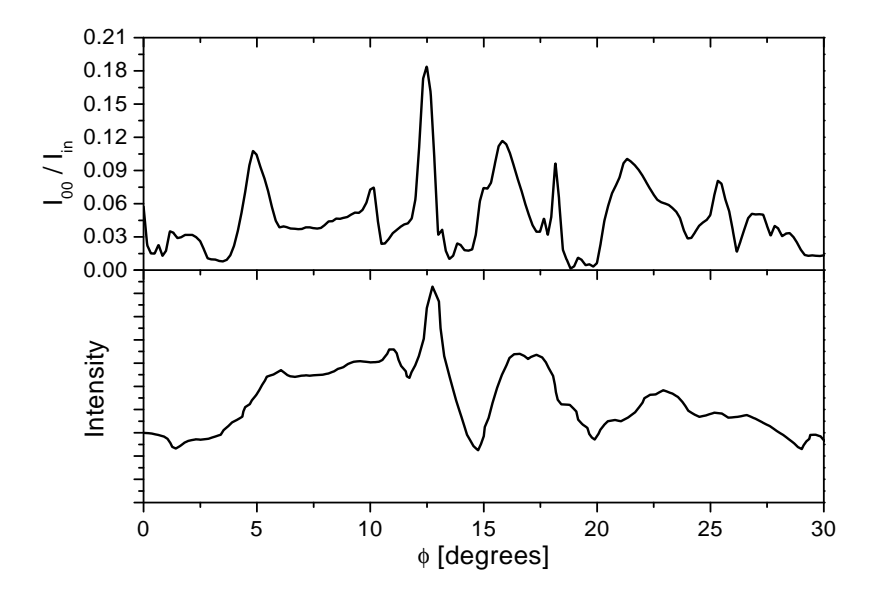


Figure 6.23: Upper and lower panels: CC azimuthal scan ($C_6 = 10650 \text{ meV Å}^6$, $\xi = 14.6$) and experimental azimuthal scan for Hec(2 × 2)3CO/Rh(111). $E_i = 19.0 \text{ meV}$, $\theta_i = 55^o$. $T_S = 150 \text{ K}$.

the center of mass of CO molecules adsorbed in on-top positions. Concerning the effective binary He-CO_{ads} potential, it has a well depth of 3.49 meV and its minimum is positioned at $z_m = 3.62$ Å. These values should be compared with the corresponding values for He-CO/Cu interaction in table 6.4.

It is tempting to try to additionally parametrise the potential by accounting for different nature of the three adsorbed CO molecules. We take the repulsive components of the interaction to be the same for all three CO molecules, but we allow for a difference in the attractive interaction. In particular, for He-CO_{top} attractive interaction we take the value of C_6 found for He - $(\sqrt{3} \times \sqrt{3})$ R30° CO/Rh(111) interaction i.e. $C_6^{top} = 9000$ meVÅ⁶, $\xi = 14.6$, and we treat the $C_6^{fcc} = C_6^{hcp}$ constants as a fit parameter. Of course, the effective C_6^{top} constant need not be the same as in the He - $(\sqrt{3} \times \sqrt{3})$ R30° CO/Rh(111) interaction, and probably is not. However, taking all the C_6 constants as fit parameters would result in a very lengthy computational procedure which, in our oppinion, would not contribute much to our understanding of the problem. The results of this investigation are presented in figure 6.25

It can be seen from this figure that the overall agreement with the experimental data cannot be much improved with respect to the model

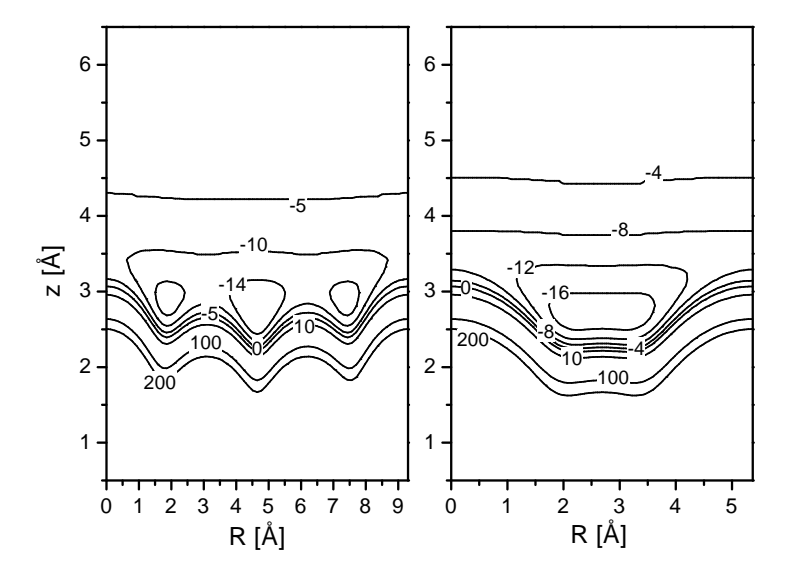


Figure 6.24: Left panel: Equipotential contours (in meV) along $\phi = 30^{\circ}$ (fig. 6.22) and between the two on-top CO molecules. Right panel: Equipotential contours (in meV) along $\phi = 0^{\circ}$ and between the two on-top CO molecules.

where C_6 constants are the same for all three differently adsorbed CO molecules.

6.5.2 Sensitivity of CC calculations to the potential details in the cases of low and high coverage overlayer structures

There may be another reason for the apparently better agreement between the CC calculations and the experimental data in the case of denser CO overlayer on Rh(111). The simple geometrical argument is shown in fig. 6.26.

It can be seen from this simple sketch that the corrugation of the *total* potential should be more sensitive to the details of the *binary* Headsorbate potential as the overlayer becomes less dense. This is due to the partial "shadowing" of the individual binary potential and its smoothing by the potentials arising from the interaction of the projectile with neighboring adsorbates. This effect is more prominent in dense overlayer structures.

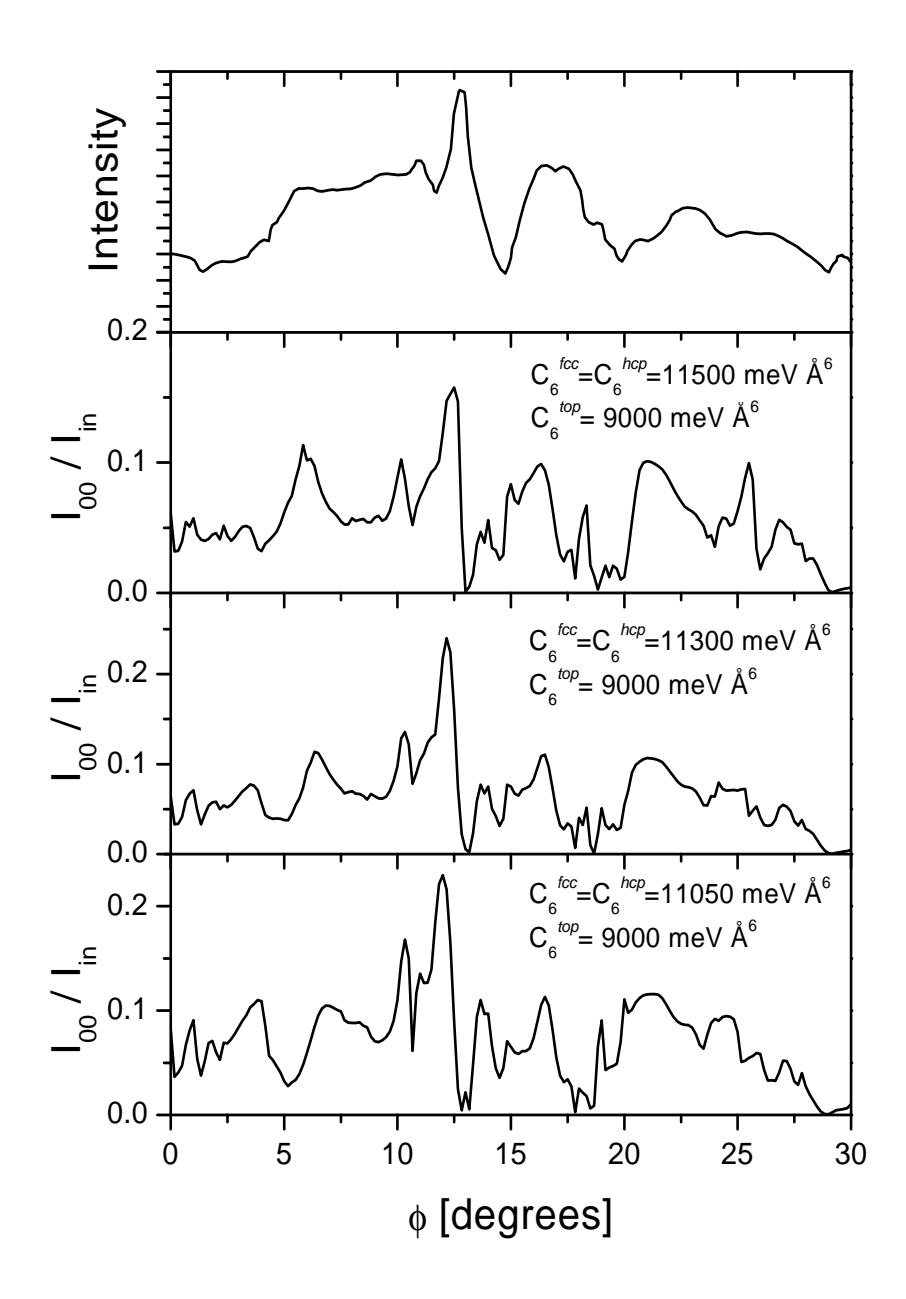


Figure 6.25: Top panel: Experimental azimuthal scan for He–c(2 × 2)3CO/Rh(111). Second, third and fourth panel: CC calculation for different values of $C_6^{fcc} = C_6^{hcp}$ constants, $C_6^{top} = 9000$ meVÅ⁶, $\xi = 14.6$. and between the two on-top CO molecules. $E_i = 19.0$ meV, $\theta_i = 55^{\circ}$.

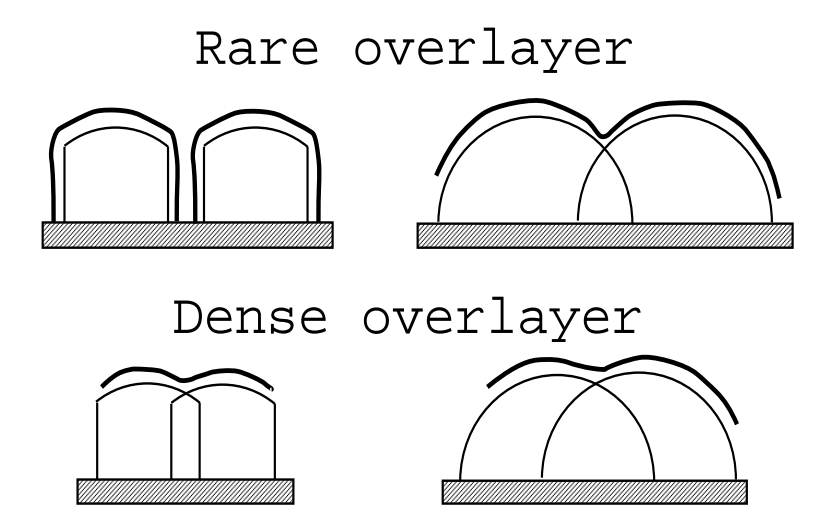


Figure 6.26: The corrugation profiles (thick lines) for two different potential models (left and right columns) in the rare (top row) and dense (bottom row) overlayer phase

6.6 Additional comments on the He - adsorbed CO potential. Comparison with the various data from literature

The studies we have presented in the previous sections suggest that the He - adsorbed CO potential is deeper than the He-CO potential in the gas phase. This effect could be related to the partial filling of the $2\pi^*$ resonance in adsorbed CO, which is a rather general effect occuring in CO adsorption on metals represented in the jellium approximation [9, 10, 11]. The depth of the potential is also partially influenced by the three-body interactions discussed in chapter 5. Both effects induce an enhancement of the He-CO attractive interaction. In particular, this enhancement has been calculated for Al, Cu, Pt, Ni and W substrates [6, 10].

However, some of the studies have reported the potentials which do not comply with the above discussed effects. In particular, for CO adsorbed on Pt(111) surface, the authors of ref. [102] report the effective He - adsorbed CO potential with a well depth of 1.38 meV and the minimum positioned at $z_m = 4.3$ Å above the CO molecule center of mass. The authors of ref. [102] discuss this decrease of the well depth as an effect arising from the shift of the repulsive part of the potential due to an increased number of electrons on the adsorbate. Although

their model of the attractive He - adsorbed CO interaction indeed predicts a larger attractive interaction with respect to the corresponding interaction in the gas phase, as our model does, the total He-adsorbed CO potential they propose is not in accord with our findings. Concerning the position of the minimum (4.3 Å), it is much too large with respect to the values we find, although for other substrates. The potential well depth is also surprisingly small. Another investigation [36] of He-adsorbed CO potential related to isolated CO molecules on Pt(111) suggested a potential with a well depth of $\approx 6~{\rm meV}$ and a minimum positioned at $\approx 3.5~{\rm Å}$. The well depth of this potential seems to be too large in comparison with the results of the present study.

Chapter 7 Summary and Conclusions

95

By a direct comparison of the results of CC calculations (Chapter 2) with the experimental data on diffractive scattering of atoms from physisorbed and chemisorbed adsorbates (discussed in Chapter 3), we have shown that a reliable projectile-target interaction potential can be constructed for several physically different adsorption systems. In Chapter 6 a variety of different adsorbate systems has been explored and a fair simulation of the experimental findings has been achieved with reasonable and physically sound potential models discussed in Chapters 4 and 5. It has also been shown that the assumption of pairwise additivity of the potentials, although of limited validity, can indeed serve as a good point of departure even for the targets consisting of strongly bound, chemisorbed adsorbates. The chemisorption induced effects on these pairwise additive pseudopotentials are discussed in chapter 5. We have also shown that the coupled channel calculations can be used to test the potentials for strongly corrugated systems where an easy identification of the selective adsorption features is not possible. A carefull investigation based on a minimum of theoretical input concerning the interaction potential can be used to precisely determine fine details of the interaction potential. As the starting point for coupled channel calculations we have considered the gas phase binary potentials which have proven to be of extreme use in the case of physisorbed adsorbates (section 6.1), the total electronic density calculation with the additional use of Esbjerg-Nørskov Ansatz (section 6.2), and the interaction potential calculation at the Hartree-Fock level which we have complemented with a realistic attractive interaction (sections 6.3 and 6.4, 6.5). As a result of our investigations, we have proposed the He - adsorbed CO potentials, which in our opinion, are the first reliable potentials of this kind in the literature.

In conclusion, it should be pointed out that the purely diffractive CC calculations can be used for a precise determination of the potential because it follows from our calculations that the diffractive transitions give rise to the majority of the structure and nonmonotonic behaviour seen in the experimental data. However, it would be highly desirable to include the inelastic channels in the CC scheme. This seems to be a very difficult task, especially in the cases where the multiphonon inelastic transitions are important. A quantitative study of inelastic effects based on the EBA formalism [2] has been presented for He \rightarrow Xe/graphite scattering system, yet a more complete approach, treating the elastic and inelastic scattering on the same footing is certainly needed.

The model potentials we propose seem to provide a fair represen-

tation of the He-adsorbate interaction, in particular the CLMTCD potential, while the gaussian representation of the lateral corrugation discussed in section 4.3 seems to be of restricted use because it does not correctly account for the fact that the equipotential curves tend to be more corrugated as the potential (energy) increases.

Though the separation of the interaction potential into the additive projectile-adsorbate and projectile-substrate components is questionable when we deal with strongly chemisorbed and dense overlayers, the *total* potential we obtain proves reliable in the studies of He atom diffraction from a number of adlayer systems.

Appendix A

Notation

Abbreviations

```
1D - One dimension(al)
```

2D - Two dimension(al)

3D - Three dimension(al)

HAS - Helium atom scattering

TOF - Time of flight

LEED - Low energy electron diffraction

EXAFS - Extended x-ray adsorption fine-structure spectroscopy

cc,CC - Coupled channel

FWHM - Full width at half maximum

CLMTCD - Cvetko, Lausi, Morgante, Tommasini, Cortona and Dondi; authors of reference [34]

amu - Atomic mass unit

Indices

i - Initial state

f - Final state

 κ - index for crystal planes parallel with the surface plane.

l - labels the crystal sites within a particular crystal plane

- j labels the crystal sites in whole semi-infinite crystal
- v labels the atoms within a 2D unit cell of the surface

Variables and functions

- x, y Cartesian coordinates in the surface plane
 - z Cartesian coordinate perpendicular to the surface plane
 - $\mathbf{R} \mathbf{R} = x\mathbf{i} + y\mathbf{j}, \ \mathbf{R} = (x, y)$
 - $\mathbf{r} \mathbf{r} = x\mathbf{i} + y\mathbf{j} + z\mathbf{k}, \ \mathbf{r} = (x, y, z)$
 - G reciprocal lattice vector in 2D
 - H any 2D vector lying in the surface plane
 - k 3D projectile particle wave vector
 - ${\bf K}\,$ projection of the projectile particle wave vector onto the surface plane
 - k_z z-component of the projectile particle wave vector
 - ψ Wave function in 1D
 - Ψ Wave function in 3D
 - ϵ_n n-the bound state of interaction potential
- L_z The dimension of the normalization box in z-direction
- L_S The dimension of the normalization box in direction parallel to the surface plane
- V Interaction potential between a projectile and a particular ensemble of atoms (only overlayer, only substrate, whole target...)
- v Binary interaction potential

Scattering parameters: masses, temperature, angles ...

- *m* Projectile atom mass
- M Target atom mass
- E_i Projectile atom energy

NOTATION 101

- T_S Temperature of the target
- $\theta_{i(f)}$ The angle between the incident (final) projectile direction and the z axis

 ϕ - Azimuthal angle

Appendix B

Classical description of atom scattering from a rigid corrugated surface

To gain an additional insight into the complexity of the problem of scattering of atoms from corrugated surfaces, we have performed a set of calculations for a simple classical representation of the problem. The target surface is "frozen" (rigid) and represented by a static potential given by

$$V(x, y, z) = D\left\{\exp\left[-2\beta(z - \xi(x, y))\right] - 2\exp\left[-\beta(z - \xi(x, y))\right]\right\},$$
(B.1)

where $\xi(x,y)$ is the corrugation function given in our case by

$$\xi(x,y) = z_0 + \eta(\cos(2\pi x/a) + \cos(2\pi y/a)).$$
 (B.2)

Is is of interest to see what happens to the classical trajectories of the projectile when the corrugation amplitude, η is varied. The classical trajectories were calculated by numerically solving the Newton equation for a particle in a potential. In figure B.1 we present the results of such a calculation.

Two top graphs represent the classical trajectories for incident energy of $E_i = 40$ meV, polar angle $\theta_i = 30^\circ$, azimuthal angle $\phi_i = 28.0^\circ$, D = 10.0 meV, $\beta = 1.0$ 1/Å, a = 2.0 Å, $z_0 = 3.0$ Å and $\eta = 0.05$ Å. The mass of the projectile atom is m = 4 amu (He). The left hand side graph represents the "side view" (x, z) plane for 100 trajectories which were started with different initial positions in the (x, y) plane, while the right hand side graph represents the same set of trajectories projected onto the (x, y) plane ("top" view). The two graphs below contain the results of the same calculation with η changed to 0.1 Å.

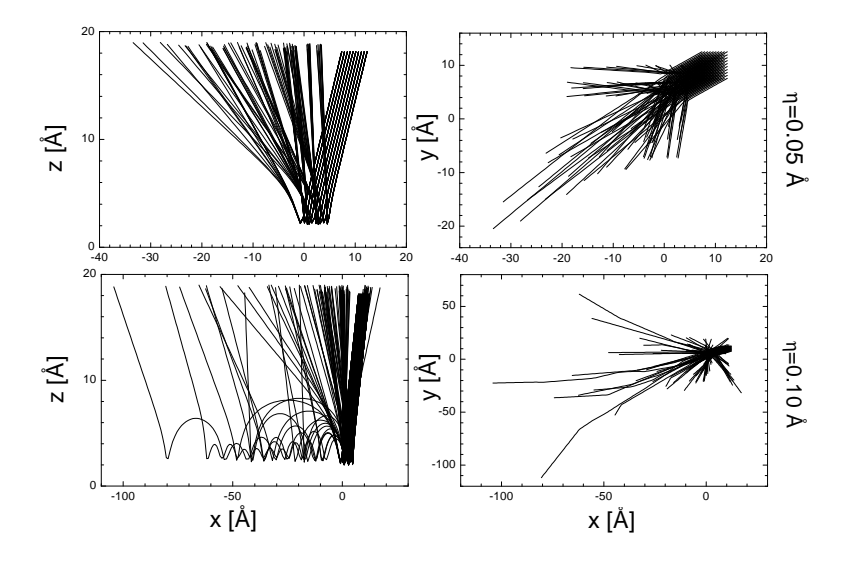


Figure B.1: Classical trajectories of projectile atom for two different corrugation amplitudes.

We observe qualitative differences between the results obtained for the two different values of the corrugation amplitude. First of all, for small corrugations, all the trajectories have only one turning point, while for larger corrugations there are some trajectories which have many turning points i.e. they "hit" the surface a number of times. Closely related to this is the time the trajectories spend in the vicinity of the surface. For very corrugated surfaces, there are trajectories for which the projectile particle spends a long time in the vicinity of the surface and, moreover, the projectile atoms travel hundreds of atomic spacings before they are "kicked away" from the surface. The distribution of times the projectile atom (He) spends in the vicinity of the surface with larger corrugation ($\eta = 0.1$) is represented in fig. B.2. Other scattering parameters are the same as in fig. B.1.

The times in fig. B.2 were calculated as the differences between the initial time (t=0), when all the incident particles were at z=19 Å, and the final time defined as the time the particle reaches any point with the z-coordinate of z=19 Å in the asymptotic region. The total of 250×250 classical trajectories with the same energies, but different initial x and y coordinates were considered in this simulation.

It can also be seen from fig. B.1 that two trajectories very closely spaced in the initial conditions may look quite different after some time.

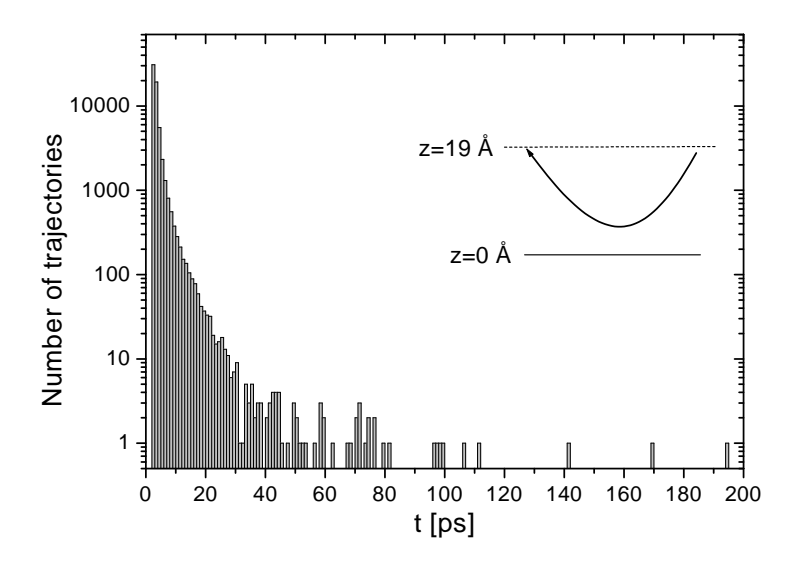


Figure B.2: Distribution of times the projectiles spend in the vicinity of the surface. Scattering parameters are the same as in fig. B.1. $\eta = 0.1$.

Whether this is a signature of orbital instability, known from the studies of nonlinear systems, or not, is not a subject of this study. However, we may expect that quantum calculations will be also very sensitive to the small changes of parameters characterizing a particular scattering system. Although there is no nonlinearity associated with the quantum representation of the problem, as the corrugation amplitude increases more and more channels must be included in the CC basis in order to get the converged results. The coupling between those numerous equations may make the quantum results very sensitive to the details of the interaction.

At this point, knowing that the systems with large surface corrugations support specific classical trajectories desribed above, we may predict that the projectile atom moving along such trajectories will strongly perturb the phonon bath since the time the projectile spends in the region of strong interaction is long ¹. Thus, one can expect that the scattering will be more inelastic in the systems with larger corrugation. To futher corroborate this statement, in fig. B.3 we select a specific trajectory and plot a force the particle moving along this

¹This description is in the spirit of the trajectory or semiclassical path approximation, see e.g. references [12, 103, 104, 105].

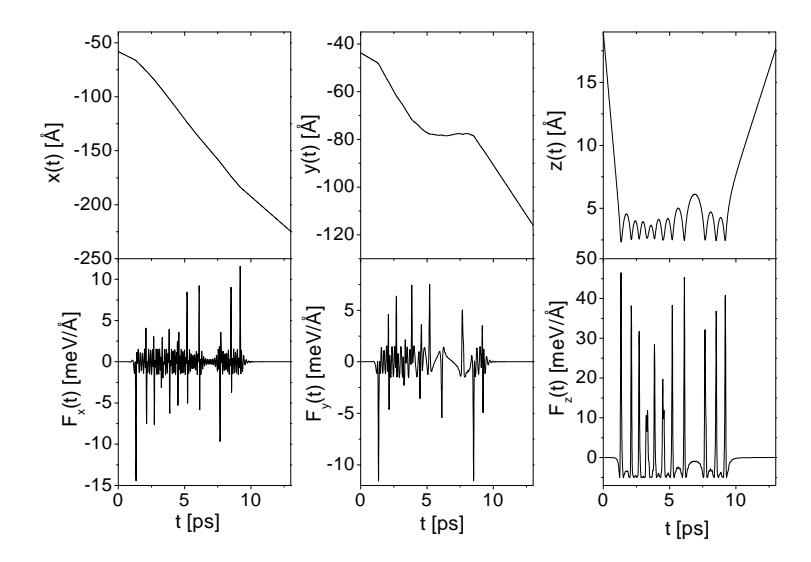


Figure B.3: Top three graphs: Trajectory of the projectile atom; x(t), y(t), z(t). Bottom three graphs: x, y and z components of the force in equation (B.3). Scattering parameters are the same as in fig. B.1.

trajectory exerts on the target. The force is defined as

$$\mathbf{F}(t) = -\nabla V(x(t), y(t), z(t)), \tag{B.3}$$

where V(x, y, z) is the same as in equation (B.1), calculated along the projectile trajectory (x(t), y(t), z(t)). It can be seen that this particular trajectory acts as an implulsive force on the target more than once 2 , which is an effect not present in the systems with low corrugation.

This relatively simple consideration may explain a long standing mystery of inelastic scattering in He- $(\sqrt{3} \times \sqrt{3})$ R30° CO/Rh(111) and He-c(2 × 2)3CO/Rh(111) scattering systems. In particular, it has been experimentally found that the scattering of He atoms is significantly more inelastic in the lower coverage overlayer phase of CO [98, 99]. According to our investigations in sections 6.4 and 6.5, the He - target interaction potential is more corrugated for the lower density CO overlayer phase. This fact alone may also explain the greater importance of inelastic events in this system.

 $^{^2}$ These impulsive moments happen at the classical turning points of the projectile.

Appendix C

Eigen-states wiht negative energy for the atoms physisorbed on a surface

The formalism of coupled channel equations can be employed to study the dynamics of atoms adsorbed on surfaces. In the formalism developed in Chapter 2 we have assumed that the total energy of the projectile atom was positive. Therefore, all the atoms impinging on the target surface scatter in continuum states with the energy equal to the incident energy. In this Appendix, we are interested in the negative total energy states of the projectile atoms which must be treated as particles permanently adsorbed on the surface. In the lowest approximation, the atom can be treated as confined in the z-direction and free in the x and y directions. The Schrödinger equation reduces to a one dimensional differential equation, and the adsorbate energies are given as

$$E_n(\mathbf{K}) = \epsilon_n + \frac{\hbar^2 \mathbf{K}^2}{2m},\tag{C.1}$$

where ϵ_n are the energies of the bound states in 1D, calculated from the lateral average of the interaction potential.

Clearly, this approach cannot be expected to provide reliable values of the bound state energies when the corrugation of the interaction potential is large. In this case, we cannot disregard the Fourier components $V_{\mathbf{G}}(z)$, $\mathbf{G} \neq 0$ of the interaction potential, and the problem of finding the bound state energies becomes much more involved since we now have to solve the Schrödinger equation in three dimensions.

The formalism of coupled channel equations can be used for this purpose as well, although we have to adapt it slightly to treat the adsorbates with negative total energy. Instead of propagating the logderivative matrix \overline{Y} from the clasically forbidden region of interaction to the asymptotic region, we propagate the \overline{Y} matrix both "forward" and "backward". Note that for negative total energy states, the regions of small and large z are classically forbidden. Thus, we propagate the \overline{Y} matrix from the region of small z to some fixed point in z coordinate, say z_f (forward propagation) and we also propagate the \overline{Y} matrix from the region of large z to the same fixed and predetermined point (backward propagation). The log-derivative matrices of the forward and backward propagation, $\overline{Y}_+(z_f)$ and $\overline{Y}_-(z_f)$, respectively, will produce a wavefunction which matches smoothly at z_f only if the total energy, E, corresponds exactly to the energy of a bound state of the hamiltonian. In this case, there is a wavefunction vector, $\psi(z_f)$, such that $\psi'_+(z_f) = \psi'_-(z_f)$. According to equation (2.11), the matching condition can be written as

$$\overline{Y}_{+}(z_f)\psi(z_f) = \overline{Y}_{-}(z_f)\psi(z_f), \tag{C.2}$$

i.e. $\overline{Y}_{match}\psi(z_f) = 0$, where $\overline{Y}_{match}(z_f) = \overline{Y}_+(z_f) - \overline{Y}_-(z_f)$. This shows that $\psi(z_f)$ is an eigenvector of the log-derivative matching matrix, $\overline{Y}_{match}(z_f)$ with eigenvalue zero.

The computational procedure consists in specifying the total (negative) energy E and the parallel wavevector of the state, \mathbf{K}_i . By varying the energy E and inspecting the eigenvalues of the log-derivative matching matrix, we can determine the energies for which the matching matrix is singular i.e. for which the bound state for a given \mathbf{K}_i exists. In this way, we can determine the adsorbate energy bands, $E_n(\mathbf{K}_i)$. Further details of the procedure can be found in references [106, 107], although the treatment presented there is related to the problem of weakly bound van der Waals molecular complexes and the Schrödinger equation is solved in the spherical rather than in the Cartesian system as in our case.

There are several points to be noted. First, the choice of the matching point, z_f is important. This point should be in the classically allowed region. A discussion concerning the choice of z_f can be found in ref. [107]. Second, it can be advantageous to revise the initial conditions for backward propagation. A recipe based on the WKB approximation is given in ref. [107]. This point is not critical. We have performed several numerical tests and found that large, diagonal log-derivative matrix can also be used as an initial condition, which is the same choice as for forward propagation. In this case, the eigenvalues corresponding to the states which are weakly bound may poorly converge. Note that all

eigenvalues are *real* due to the symmetry of the log-derivative matrices. There may occur problems related to the determination of two different eigenvalues closely spaced in energy, but these can be easily solved by a more refined search for the eigenvalues in the energy interval of interest.

For illustration of the procedure described above, we present in figure C.1 the results of calculation for the bound states of He atom adsorbed on a Xe/graphite surface. This system was studied in section 6.1 for positive total energies of the He atom. The interaction potential between He atom and Xe/graphite surface is constructed as in section 6.1. Note that the lateral corrugation of the potential strongly influences the behaviour of adsorbed atoms. In particular, the lowest energy of a He atom on Xe/graphite estimated only from the $V_{00}(z)$ component of the interaction potential is ≈ -5.2 meV, while the calculation in fig. C.1 reveals that the exact lowest energy is \approx -6.4 meV. Also, the curvatures of the bands in fig. C.1 are very different from the corresponding band curvatures when the interaction potential is flat in x and y directions. In other words, the effective mass of an adsorbed He atom is larger than the mass of a free He atom. In particular, for the band with the lowest energy we find that the effective mass of adsorbed He atom is 7.01 amu, which is a factor of 1.75 larger than the mass of free He atom. All these facts can have remarkable consequences on the heat capacity of the adsorbed overlayer [108].

In figure C.2 we plot the bands of He atom adsorbed on $c(2\times2)$ CO/Cu(001). The details of the interaction potential model can be found in section 6.3. It is interesting to note here that the effective mass of He atom in the lowest energy band is 121.8 amu (!) which means that the adsorbed He atom is essentially localized to a particular adsorption site. This is due to very large corrugation of the He - $c(2\times2)$ CO/Cu(001) interaction potential (significantly larger than for He - Xe/graphite). The potential barrier for a transition from one adsorption site to another is therefore very large.

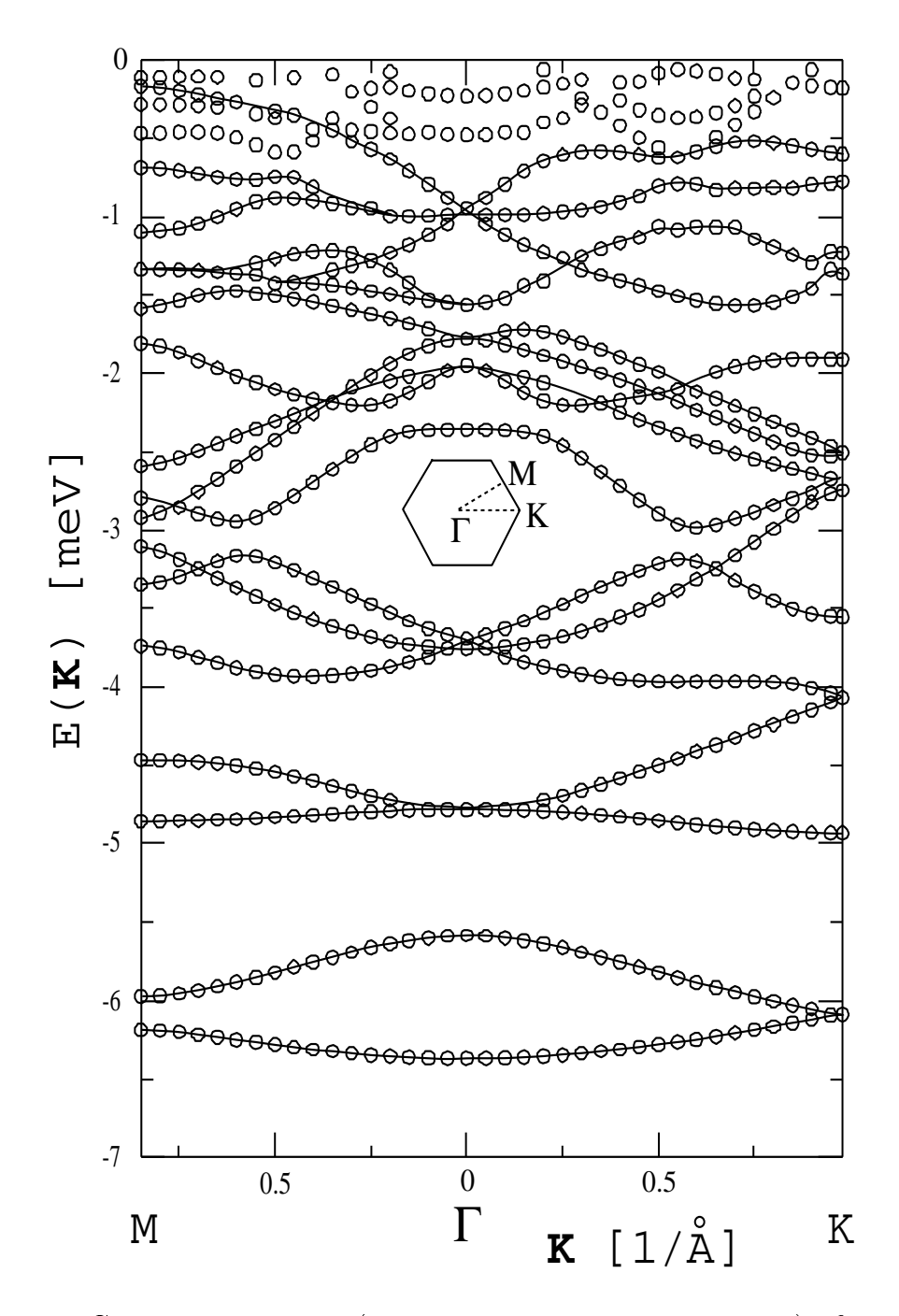


Figure C.1: Band stucture (states with negative total energy) of He atom physisorbed on Xe monolayer on graphite. The bands are drawn along Γ -K and Γ -M directions in the overlayer Brillouin zone (inset). The size of the symbols approximately corresponds to the accuracy of the calculation.

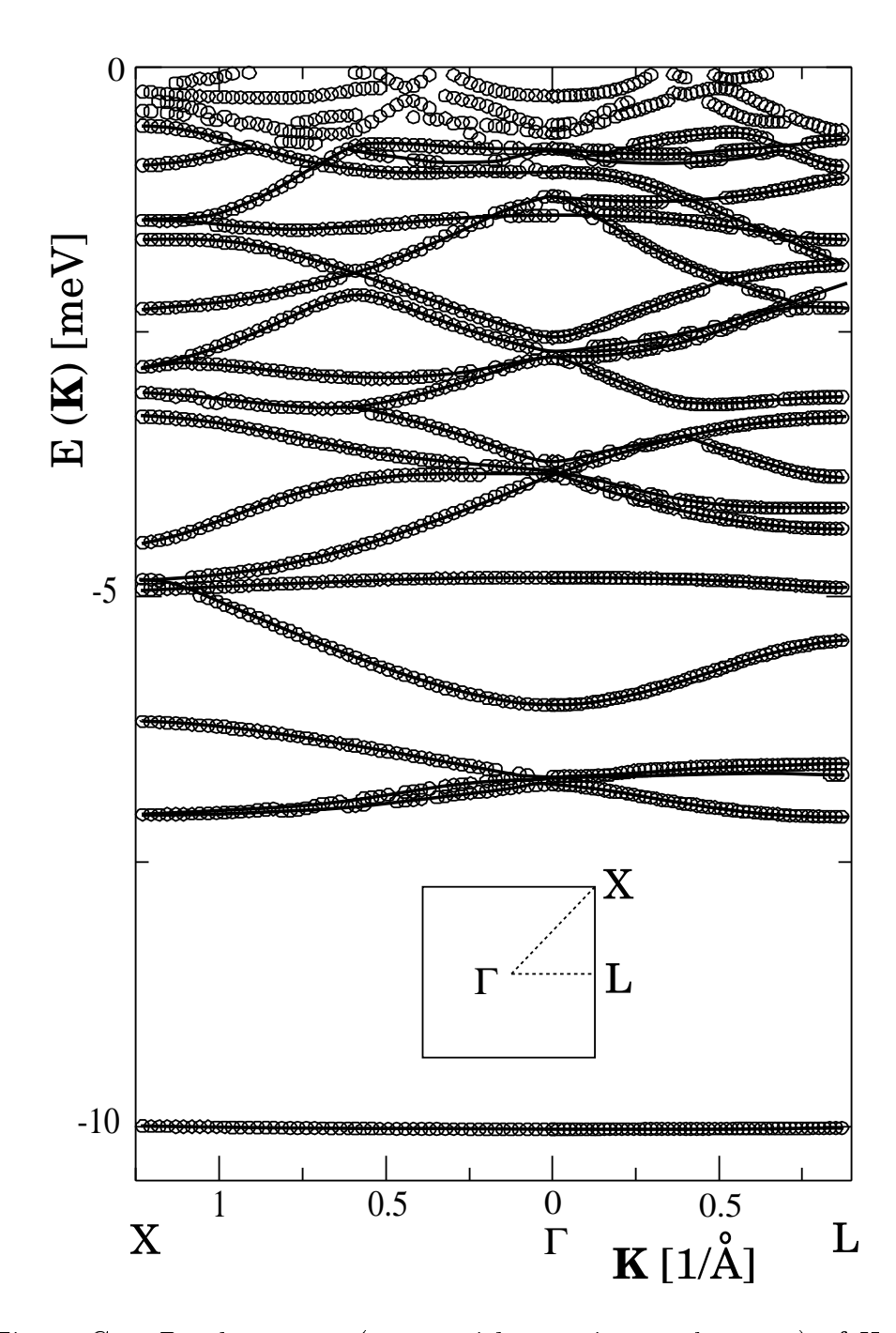


Figure C.2: Band stucture (states with negative total energy) of He atom physisorbed on $c(2\times2)$ CO/Cu(001) surface. The bands are drawn along Γ -L and Γ -X directions in the overlayer Brillouin zone (inset). The size of the symbols approximately corresponds to the accuracy of the calculation.

Bibliography

- [1] D. Farias and K.-H. Rieder, Atomic beam diffraction from solid surfaces, Rep. Prog. Phys. **61**, 1575 (1998)
- [2] B. Gumhalter, Single and multiphonon atom-surface scattering in the quantum regime, Physics Reports 351, 1 (2001)
- [3] G. Vidali, G. Ihm, H.-Y. Kim and M.W. Cole, *Potentials of physical adsorption*, Surface Science Reports 12, 133 (1991)
- [4] E. Hulpke (Ed.), *Helium Atom Scattering from Surfaces*, Springer-Verlag, 1992
- [5] B. Gumhalter and K. Wandelt, Implication of fractional occupation of adsorbate resonances on van der Waals Interactions at surfaces, Phys. Rev. Lett. 57, 2318 (1986)
- [6] D. Lovrić and B. Gumhalter, Electronic spectral properties of surfaces and adsorbates and atom-adsorbate van der Waals interactions, Phys. Rev. B 38, 10323 (1988)
- [7] F. Hofmann and J.P. Toennies, *High-resolution helium atom time-of-flight spectroscopy of low-frequency vibrations of adsorbates*, Chemical Reviews **96**, 1307 (1996)
- [8] J.E. Lennard-Jones and A.F. Devonshire, Proc. Roy. Soc. London, Ser. A 158, 242 (1937)
- [9] B. Gumhalter, K. Wandelt, P. Avouris, 2-Pi* resonance features in the electronic spectra of chemisorbed CO, Phys. Rev. B 37, 8048 (1988)
- [10] D. Lovrić, Proračun van der Waalsovog medjudjelovanja u raspršenjima atoma na molekularnim adsorbatima (A calculation of van der Waals interaction in scattering of atoms from molecular adsorbates), M.Sc. Thesis, University of Zagreb, 1988

- [11] B. Gumhalter, M. Milun and K. Wandelt, Selected Studies of Adsorption on Metal and Semiconductor Surfaces, German-Yugoslav cooperation in scientific research and technological development, 1990
- [12] A. Šiber, Theory of inelastic scattering of thermal energy atoms from surfaces, MSc Thesis, University of Zagreb, 1999
- [13] B. Poelsema and G. Comsa, Scattering of thermal energy atoms from disordered surfaces, Springer-Verlag, 1989
- [14] D.P. Clougherty and W. Kohn, Quantum theory of sticking, Phys. Rev. B 46, 4921 (1992)
- [15] Ch. Wöll, private communication
- [16] M.L. Goldberger and K.M. Watson, Collision theory, John Wiley and sons, 1964
- [17] F.A. Gianturco, The transfer of molecular energies by collision: recent quantum treatments, Springer Verlag, 1979
- [18] R.G. Gordon, New method for constructing wavefunctions for bound states and scattering, J. Chem. Phys. 51, 14 (1969)
- [19] R.G. Gordon, Quantum scattering using piecewise analytic solutions, Meth. Comput. Phys. 10, 81 (1971)
- [20] B.R. Johnson, The multichannel log-derivative method for scattering calculations, J. Comput. Phys. 13, 445 (1973)
- [21] B.R. Johnson, New numerical methods applied to solving the onedimensional eigenvalue problem, J. Chem. Phys. 67, 4086 (1977)
- [22] F. Mrugala and D. Secrest, The generalized log-derivative method for inelastic and reactive collisions, J. Chem. Phys. 78, 5954 (1983)
- [23] D.E. Manolopoulos, M.J. Jamieson and A.D. Pradhan, *Johnson's log derivative algorithm rederived*, J. Comput. Phys. **105**, 169 (1993)
- [24] D.E. Manolopoulos, The log-derivative approach to inelastic scattering, bound state and photofragmentation problem, PhD Thesis, University of Cambridge, 1988
- [25] B.H. Choi and R.T. Poe, Theory of phonon inelastic atom-surface scattering. I. Quantum mechanical treatment of collision dynamics, J. Chem. Phys. 83, 1330 (1985)

[26] B.H. Choi and R.T. Poe, Thory of phonon inelastic atom-surface scattering. II. Approximate methods and applications to resonance and adsorption, J. Chem. Phys. 83, 1344 (1985)

- [27] Ch. Boas, Th. Becker, M. Kunat, U. Burghaus and Ch. Wöll, Comment on "Effect of the structural anisotropy and lateral strain on the surface phonons of monolayer xenon on Cu(110)", Phys. Rev. B 64, 037401 (2001)
- [28] K.H. Rieder, G. Parschau and B. Burg, Experimental evidence for anticorrugating effects in He-metal interactions at surfaces, Phys. Rev. Lett. 71, 1059 (1993)
- [29] M. Petersen, S. Wilke, P. Ruggerone, B. Kohler and M. Scheffler, Scattering of rare-gas atoms at a metal surface: Evidence of Anticorrugation of the helium-atom potential energy surface and the surface electron density, Phys. Rev. Lett. 76, 995 (1996)
- [30] P. Cortona, M.G. Dondi, A. Lausi and F. Tommasini, New analysis of He scattering data from Ag(110) and Cu(110), Surf. Sci. 276, 333 (1992)
- [31] K.T. Tang and J.P. Toennies, An improved simple model for the van der Waals potential based on universal damping functions for the dispersion coefficients, J. Chem. Phys. 80, 3726 (1984)
- [32] P. Cortona, M.G. Dondi and F. Tommasini, Electron density of metal surfaces: Cu(113), Cu(115), Cu(117) and Ag(110), Surf. Sci. 261, L35 (1992)
- [33] A. Bellman, A. Morgante, M. Polli, F. Tommasini, D. Cvetko, V.R. Dhanak, A. Lausi, K.C. Prince and R. Rosei, Quantitative structure determination of (1 × 2)-Rh(110) by helium scattering, Surf. Sci. 298, 1 (1993)
- [34] D. Cvetko, A. Lausi, A. Morgante, F. Tommasini, P. Cortona and M.G. Dondi, A new model for atom-atom potentials, J. Chem. Phys. 100, 2052 (1994)
- [35] A. Franchini, G. Santoro, V. Bortolani, A. Bellman, D. Cvetko, L. Floreano, A. Morgante, M. Peloi, F. Tommasini and T. Zambelli, Role of the He atom surface potential on the Cu(001) phonon determination, Surface Review and Letters 1, 67 (1994)
- [36] B.H. Choi, A.P. Graham, K.T. Tang and J.P. Toennies, Helium atom scattering from isolated CO molecules on a Pt(111) surface: Experiment versus close-coupling calculations for a realistic He-CO potential, J. Chem. Phys. 112, 10538 (2000)

- [37] J.R. Klein, L.W. Bruch and M.W. Cole, Many-body interactions in physisorption: Nonadditividy of film and substrate contributions to the holding potential, Surf. Sci. 173, 555 (1986)
- [38] L.W. Bruch, M.W. Cole, and E. Zaremba, *Physical Adsorption: Forces and Phenomena*, Clarendon Press, Oxford, 1997
- [39] J.R. Klein and M.W. Cole, Three-body interaction between an atom and a monolayer film, Surf. Sci. 134, 722 (1983)
- [40] H. Stenschke, Effective Axilrod-Teller interaction in van der Waals gases and liquids, J. Chem. Phys. 100, 4704 (1994)
- [41] Y. Takada and W. Kohn, Interaction potential between a helium atom and metal surfaces, Phys. Rev. Lett. 54, 470 (1985)
- [42] Y. Takada and W. Kohn, Phys. Rev. B 27, 826 (1987)
- [43] V. Celli, Theory of helium scattering from surface phonons in **Surface** phonons, eds W. Kress and F.W. de Wette, Springer-Verlag, 1991
- [44] A. Zangwill, *Physics at surfaces*, Cambridge University Press, 1988
- [45] P. Nordlander and J. Harris, The interaction of helium with smooth metal surfaces, J. Phys. C 17, 1141 (1984)
- [46] N. Cabrera, V. Celli, F.O. Goodman and R. Manson, Scattering of atoms by solid surfaces I, Surf. Sci. 19, 67 (1970)
- [47] B. Gumhalter and D.C. Langreth, Unified model of diffractive and multiphonon He atom scattering from adsorbates: Holstein renormalization of the interactions and the complete Debye-Waller factor, Phys. Rev. B 60, 2789 (1999)
- [48] A.C. Levi and H. Suhl, Quantum theory of atom-surface scattering: Debye-Waller factor, Surf. Sci. 88, 221 (1979)
- [49] B. Gumhalter, Different aspects of the Debye-Waller factor in various atom-surface scattering theories, Surf. Sci. **347**, 237 (1996)
- [50] G. Armand, J. Lapujoulade and Y. Lejay, The Debye-Waller factor in helium scattering by a crystalline surface, Surf. Sci. 63, 143 (1977)
- [51] M.G. Dondi, S. Terreni, F. Tommasini and U. Linke, Electron density at the Ag(110) surface studied by He diffraction, Phys. Rev. B 37, 8034 (1988)

[52] J.M. Hutson and C. Schwartz, Selective adsorption resonances in the scattering of helium atoms from xenon coated graphite: Close-coupling calculations and potential dependence, J. Chem. Phys. **79**, 5179 (1983)

- [53] R.A. Aziz, U. Buck, H.Jónsson, J.-C. Ruiz-Suárez, B. Schmidt, G. Scoles, M.J. Slaman and J. Xu, Two and three-body forces in the interaction of He atoms with Xe overlayers adsorbed on (0001) graphite, J. Chem. Phys. 91, 6477 (1989)
- [54] S. Chung, N. Holter and M.W. Cole, He interaction with Xe and Kr adsorbed on graphite or Ag surfaces, Phys. Rev. B 31, 6660 (1985)
- [55] G. Vidali and M.W. Cole, Effective interaction between He atoms on a graphite surface, Phys. Rev. B 22, 4661 (1980)
- [56] G. Bracco, P. Cantini, A. Glachant and R. Tatarek, Diffraction of He atoms from a Xe overlayer adsorbed on graphite (0001), Surf. Sci. 125, L81 (1983)
- [57] G. Bracco, P. Cantini, E. Cavanna, R. Tatarek and A. Glachant, Selective adsorption and interaction potential of He/Xe-graphite, Surf. Sci. 136, 169 (1984)
- [58] J.P. Toennies and R. Vollmer, Helium atom scattering studies of the dynamics of a xenon-monolayer-covered graphite single-crystal surface, Phys. Rev. B 40, 3495 (1989)
- [59] R. Vollmer, Phasenübergänge und Dynamik von Festkörperoberflächen und physisorbierten Schichten, PhD Thesis, Georg-August-Universität, Göttingen (1991)
- [60] A. Šiber, B. Gumhalter, A.P. Graham and J.P. Toennies, He atom scattering and theoretical study of the surface phonons of a simple benchmark system: Xe(111), Phys. Rev. B 63, 115411 (2001)
- [61] A. Šiber and B. Gumhalter, Zone edge focused two-phonon processes in He atom scattering from a simple prototype system: Xe(111), Surf. Sci. 502-503, 422 (2002)
- [62] A. Siber and B. Gumhalter, to be published
- [63] M. Manninen, J.K. Nørskov, M.J. Puska and C. Umrigar, Phys. Rev. B 29, 2314 (1984)
- [64] M.W. Cole and T.T. Tsong, Phys. Rev. B **31**, 727 (1985)
- [65] N.D. Lang and J.K. Norskov, Phys. Rev. B 27, 4612 (1983)

- [66] I.P. Batra, Helium-surface interaction potential: Determination and applications, Surf. Sci. 148, 1 (1984)
- [67] W.A. Harrison, Pseudopotentials in the theory of metals, Benjamin, New York, 1966
- [68] M.J. Cardillo, G.E. Becker, D.R. Hamann, J.A. Serri, L. Whitman and L.F. Mettheiss, Geometry of the Ag(001)-c(2×2)Cl structure as determined by He diffraction, Phys. Rev. B 28, 494 (1983)
- [69] T. Kramar, D. Vogtenhuber, R. Podloucky and A. Neckel, Electronic structure calculations for a c(2×2)-Cl overlayer on a Ag(001) surface, Electrochimica Acta 40, 43 (1995)
- [70] E. Zanazzi, F. Jona, D.W. Jepsen and P.M. Maracus, Atomic arrangement in the $c(2\times2)$ structure of Cl on Ag(100), Phys. Rev. B **14**, 432 (1976)
- [71] G.E. Becker, M.J. Cardillo, J.A. Serri and D.R. Hamann, He-Ag(001)- $c(2\times2)Cl$ attractive potential from resonance scattering, Phys. Rev. B **28**, 504 (1983)
- [72] G.M. Lamble, R.S. Brooks, J.-C. Campuzano, D.A. King and D. Norman, Structure of the c(2×2) coverage of Cl on Ag(100): A controversy resolved by surface extended x-ray-adsorption fine-structure spectroscopy, Phys. Rev. B 36, 1796 (1987)
- [73] A. Neckel, private communication
- [74] M.J. Frisch et al, Gaussian 98, Gaussian Inc., Pittsburgh, PA, 1999
- [75] Ch. Wöll, K. Weiss and P.S. Bagus, Saturated hydrocarbons on a Cu surface: a new type of chemical interaction?, Chem. Phys. Lett. **332**, 553 (2000)
- [76] F. Hofmann, PhD Thesis
- [77] J.P. Toennies, private communication
- [78] K. Lenarčić-Poljanec, M. Hodošček, D. Lovrić and B. Gumhalter, Interaction of He atoms with (111) and (100) surfaces of Cu and Ni, Surf. Sci. 251-252, 706 (1991)
- [79] C. Boas, private communication
- [80] J. Ellis, J.P. Toennies and G. Witte, Helium atom scattering study of the frustrated translation mode of CO adsorbed onto the Cu(001) surface, J. Chem. Phys. 102, 5059 (1994)

[81] J. Ellis, K. Hermann, F. Hofmann and J.P. Toennies, Experimental determination of the turning point of thermal energy helium atoms above a Cu(001) surface, Phys. Rev. Lett. 75, 886 (1995)

- [82] S. Green and P. Thaddeus, Rotational excitation of CO by collisions with He, H and H₂ under conditions in interstellar clouds, The Astrophysical Journal **205**, 766 (1976)
- [83] L.D. Thomas, W.P. Kraemer and G.H.F. Diercksen, *Rotational excitation of CO by He impact*, Chem. Phys. **51**, 131 (1980)
- [84] C.E. Chuaqui, R.J. Le Roy and A.R.W. McKellar, *Infrared spectrum* and potential energy surface of He-CO, J. Chem. Phys. **101**, 39 (1994)
- [85] F.-M. Tao, S. Drucker, R.C. Cohen and W. Klemperer, Ab initio energy surface and dynamics of He-CO, J. Chem. Phys. 101, 8680 (1994)
- [86] B.H. Choi, K.T. Tang and J.P. Toennies, Interpretation of helium atom scattering from isolated CO molecules on copper (001) based on exact quantum mechanical model, J. Chem. Phys. 107, 1631 (1997)
- [87] A.P. Graham, F. Hofmann, J.P. Toennies and J.R. Manson, Helium atom scattering from isolated CO molecules on copper (001), J. Chem. Phys. 105, 2093 (1996)
- [88] C. Hättig and B.A. Hess, TDMP2 calculation of dynamic multipole polarizabilities and dispersion coefficients of triplebonded molecules CO, N₂, CN⁻ and NO⁺, J. Chem. Phys. 105, 9948 (1996)
- [89] W.-K. Liu and B. Gumhalter, Scattering of helium atoms from adsorbates - van der Waals potentials and scattering formalism, Surf. Sci. 148, 371 (1984)
- [90] W.-K. Liu and B. Gumhalter, Potentials and scattering cross sections for collisions of He atoms with adsorbed CO, Surf. Sci. 180, 169 (1987)
- [91] M.-N. Carré and D. Lemoine, Fully quantum study of the 3D diffractive scattering of He from isolated CO adsorbates on Pt(111), J. Chem. Phys. 101, 5305 (1994)
- [92] M. Gierer, A. Barbieri, M.A. Van Hove and G.A. Somorjai, Structural reanalysis og the $Rh(111)+(\sqrt{3}\times\sqrt{3})R30^{\circ}$ -CO and $Rh(111)+(2\times2)-3CO$ phases using automated tensor LEED, Surf. Sci. **391**, 176 (1997)
- [93] A.F. Bellman, D. Cvetko, A. Morgante, M. Polli, F. Tommasini, V.R. Dhanak, A. Lausi, K.C. Prince, R. Rosei, P. Cortona and M.G. Dondi, He scattering from Rh(110), Surf. Sci. 282, 273 (1993)

- [94] E. Kirsten, G. Parschau and K.H. Rieder, Resonant scattering of Heatoms from missing-row reconstructed Pt(110)1×2: comparison of theory and experiment, Surf. Sci. 236, L365 (1990)
- [95] D. Lovrić, private communication
- [96] H. Over, S. Schwegmann, G. Ertl, D. Cvetko, V. Derenzi, L. Floreano, R. Gotter, A. Morgante, M. Peloi, F. Tommasini and S. Zennaro, Temperature behavior of the (√3×√3)R30°-1CO and the (2 × 2)-3CO overlayers on Rh(111) A combined HAS and LEED investigation, Surf. Sci. 376, 177 (1997)
- [97] G. Witte, private communication
- [98] G. Witte, Low-energy dynamics of CO and NO chemisorbed on Rh(111), J. Chem. Phys. 115, 2757 (2001)
- [99] G. Witte, Untersuchung der Dynamik und Struktur von sauberen und adsorbatbedeckten Oxid- und Metalloberflächen, PhD Thesis (1995)
- [100] D. Cvetko, V. De Renzi, L. Floreano, A. Lausi, A. Morgante, M. Peloi, F. Tommasini, E. Kirsten and K.H. Rieder, Electron density of (1 × 2)Pt(110) from He reflectivity measurements, Phys. Rev. B 51, 11055 (1995)
- [101] E. Lundgren, X. Torrelles, J. Alvarez, S. Ferrer, H. Over, A. Beutler and J.N. Andersen, Surface x-ray-diffraction study of the $Rh(111)+(2\times 2)-3CO$ structure, Phys. Rev. B **59**, 5876, 1999
- [102] H. Jónsson, J.H. Weare and A.C. Levi, Structure and molecular properties of adsorbates at low coverage: Light-atom scattering from adsorbed Xe and CO, Phys. Rev. B 30, 2241 (1984)
- [103] K. Burke and W. Kohn, Finite Debye-Waller factor for "classical" atom-surface scattering, Phys. Rev. B 43, 2477 (1991)
- [104] A. Šiber and B. Gumhalter, Comment on "Quantum scattering of heavy particles from a 10 K Cu(111) surface", Phys. Rev. Lett. 81, 1742 (1998)
- [105] T. Andersson, F. Althoff, P. Linde, S. Andersson and K. Burke, Probing a cold surface with slow heavy-atom scattering: Experimental results and theoretical calculations, Phys. Rev. B 6504, 5409 (2002)
- [106] A.E. Thornley and J.M. Hutson, Bound-state wave functions from coupled channel calculations using log-derivative propagators: Application to spectroscopic intensities in Ar-HF, J. Chem. Phys. 107, 5578 (1994)

[107] J.M. Hutson, Coupled channel methods for solving the bound-state Schrödinger equation, Computer Physics Communications 84, 1 (1994)

[108] M.W. Cole, D.R. Frankl and D.L. Goodstein, *Probing the helium-graphite interaction*, Rev. Mod. Phys. **53**, 199 (1981)

SAŽETAK

U ovom se radu istražuje medjudjelovanje (interakcija) atoma He (projektila) sa površinama materijala (supstrata) pokrivenim uredjenim slojevima atoma ili molekula (adsorbata) različitih gustoća (pokrivenosti). Kao osnovna teorijska metoda koristi se metoda vezanih kanala (coupled channel) koja je razvijena koristeći tzv log-derivative način traženja valne funkcije problema i prilagodjena geometriji raspršenja atoma i molekula na čistim ili adsorbatima pokrivenim površinama. Metoda predstavlja egzaktno rješenje Schrödingerove jednadžbe i daje S-matricu problema tj. sve amplitude prijelaza iz početnog stanja projektila u skup finalnih stanja projektila. Za rješavanje problema raspršenja atoma na površinama nužna je informacija o interakciji projektila i mete.

Razmotren je niz pogodnih modela interakcijskog potencijala koji sadrže sve bitne karakteristike fizikalne interakcije atoma termalne energije sa navedenim površinama. Posebno su razmotreni modeli potencijala koji imaju analitičke rastave u diskretni Fourierov red (vezano uz diskretnu dvodimenzionalnu periodičnost meta). Takvi potencijali su od interesa jer omogućuju jednostavno prilagodjavanje modelnih parametara tako da što bolje reproduciraju eksperimentalne rezultate. Ovo se pokazuje posebno važnim u slučajevima kad potencijal interakcije nije poznat ili nije poznat u potpunosti.

Razradjen je način konstrukcije interakcijskog potencijala izmedju projektila i meta koje se sastoje od

- (i) adsorbata vezanih za metu slabim van der Waalsovim silama (fizisorbirani adsorbati) i
- (ii) adsorbata vezanih za metu jakim silama kemijskog porijekla nastalih preraspodjelom naboja u adsorbatu i meti (kemisorbirani adsorbati).

Za mete koje sadrže sloj fizisorbiranih adsorbata, interakcijski potencijal može se vrlo precizno odrediti znajući interakciju projektila s adsorbatom u plinovitoj fazi. U najgrubljoj aproksimaciji ukupna projektilmeta interakcija dana je sumom projektil-adsorbat interakcija poznatih iz eksperimenata raspršenja u plinskoj fazi i projektil-supstrat interakcijom koja je u prostoru gibanja projektila uglavnom dana samo svojom privlačnom van der Waals komponentom. Ovakva aproksimacija

 $SA\check{Z}ETAK$ 123

daje za većinu sistema poznatih u literaturi potencijal točan unutar 5 %. Dodatne korekcije interakciji mogu se izračunati tretirajući interakcije tri tijela (projektil-adsorbat-adsorbat i projektil-adsorbat-supstrat) koje postaju bitne kad su adsorbati kondenzirani na površinu supstrata a koje su zanemarivo male u raspršenjima u plinskoj fazi ukoliko je gustoća plina mala.

Za razliku od ovakvih, relativno jednostavnih sistema, sistemi koji sadrže slojeve kemisorbiranih adsorbata predstavljaju znatno kompliciraniji problem jer dolazi do promjene u elektronskoj strukturi supstrata i adsorbata pa tako efektivna projektil-adsorbat interakcija postaje bitno drukčija od iste interakcije kad su projektil i adsorbat u plinskoj fazi. Za dovoljno guste slojeve adsorbata, znatno se mijenja i elektronska struktura supstrata tako da i efektivna projektil-supstrat interakcija predstavlja nepoznanicu i može se a priori pretpostaviti da se ta interakcija mijenja sa gustoćom sloja adsorbata. Bez obzira na gore navedene probleme, može se pretpostaviti da je ukupna interakcija projektila s metom i dalje (kao i u slučaju fizisorbiranih adsorbata) dana sumom efektivnih projektil-adsorbat i projektil-substrat interakcija koje treba odrediti usporedbom teorijskih predvidjanja sa eksperimentalnim rezultatima. U ovom slučaju govorimo o efektivnim potencijalima ili pseudopotencijalima.

Metoda je primijenjena na difraktivno (elastično) raspršenje projektila na prototipnim sistemima koji ilustriraju slučajeve fizisorbiranih i kemisorbiranih adsorbata. Razmotreni su sistemi monosloja Xe atoma na grafitu (fizisorbirani adsorbati), Cl atoma na (001) površini srebra i CO molekula na kristalnim površinama bakra i rodija (kemisorbirani adsorbati). Opsežnim usporedbama predvidjanja teorije s eksperimentalnim rezultatima odredjeni su potencijali interakcije He atoma s navedenim metama.

Za raspršenje He atoma na monosloju Xe na grafitu potencijal je konstruiran na osnovi informacije of He-Xe interakciji u plinskoj fazi i He-grafit interakcije poznate kako iz eksperimentalnih, tako i iz teorijskih izvora. Nadjeno je da potencijal reproducira sve bitne značajke eksperimenata. Takodjer je odredjena važnost neelastičnih procesa i njihov utjecaj na eksperimentalne podatke. Primjenom metode eksponencirane Bornove aproksimacije u kombinaciji sa informacijom o fononima u Xe/grafit sistemu, izračunato je da za relativno visoke energije He atoma (64 meV) broj neelastično raspršenih čestica može dosegnuti 90 % ukupnog broja raspršenih He atoma, bez obzira na nisku temperaturu mete (17 K). Takodjer je nadjeno da neelastični procesi ne utječu bitno na glavne značajke eksperimentalnih spektara i da se

svo nejednoliko ponašanje raspršenog intenziteta ovisno o parametrima raspršenja, može pripisati elastičnim efektima i to uglavnom rezonancijama selektivne adsorpcije (selective adsorption resonances).

Za raspršenje He atoma na Ag(001) površini prekrivenoj uredjenim slojem Cl atoma $c(2 \times 2)$ simetrije, nadjeno je da prethodni potencijali poznati iz literature ne odgovaraju eksperimentalnim rezultatima, te je predložen novi potencijal koji je za više od faktora 2 plići (manje privlačan). Kao polazna točka u konstrukciji potencijala poslužili su proračuni elektronske gustoće mete u kombinaciji sa tzv Esbjerg-Nørskovom pretpostavkom (ansatz). Pokazano je da se odbojni dio interakcije He atoma s metom može konstruirati na osnovu elektronske gustoće mete. Usporedbom predvidjanja proračuna vezanih kanala sa eksperimentalnim rezultatima pokazano je da predloženi potencijal dobro reproducira značajke eksperimenata. Takodjer su diskutirani mogući efekti anizotropije interakcijskog potencijala vezani uz diskretnu strukturu mete.

Kao polazna točka u konstrukciji interakcijskog potencijala izmedju He atoma i (001) površine bakra prekrivene slojem adsorbiranih CO molekula $c(2\times 2)$ simetrije, poslužio je proračun ukupne energije na Hartree-Fock nivou. Ovako dobiven potencijal nadopunjen je realističnom privlačnom interakcijom koja se ne može reproducirati proračunima Hartree-Fock tipa, pa čak niti danas aktualnim, vrlo razradjenim proračunima koji se baziraju na metodi funkcionala elektronske Funkcionalni oblik i veličina dodana privlačne interakcije odredjeni su usporedbama s postojećim eksperimentalnim podacima. Nadjeno je da se efektivni He-CO potencijal znatno razlikuje s obzirom na potencijal interakcije kad su He atom i CO molekula u plinskoj fazi, te da je od njega dublji za $\sim 0.7 \text{ meV}$. Usporedbom sa potencijalima predloženima u postojećoj literaturi, nadjeno je da većina tih potencijala nije dovoljno precizna. Slična studija provedena je za adsorbirane slojeve CO molekula na (111) površinu rodija. Razmotrene su dvije različite pokrivenosti CO molekula koje proizvode uredjene CO slojeve različite simetrije. Usporedbom s eksperimentalnim podacima, nadjen je efektivni He-CO potencijal. Nadjeno je da faza u kojoj je pokrivenost CO molekula manja ima veću "valovitost" (korugaciju) ekvipotencijalnih ploha, te da ta činjenica može objasniti veću važnost neelastičnih efekata u ovom sistemu (dodatak B).

Uporaba metode vezanih kanala za proračun energija vezanih stanja diskutirana je u dodatku C.

Životopis

Rodjen sam 27. studenog 1972. godine u Zagrebu. Prirodoslovno matematički fakultet u Zagrebu, smjer inž. fizike, završio sam u srpnju 1996. godine. Diplomski rad naslova "Utjecaj karakteristika potencijala na Debye-Wallerov faktor u raspršenjima atoma na površinama" izradio sam pod vodstvom dr. Branka Gumhaltera na Institutu za fiziku u Zagrebu. Od veljače 1997. godine radim kao asistent na Institutu za fiziku u Zagrebu. Magistarski rad naslova "Theory of thermal energy atom scattering from surface vibrations" obranio sam u listopadu 1999. godine.

Objavio sam slijedeće radove koji se pojavljuju u *Current Contents* bazi podataka:

- 1. A. Šiber and B. Gumhalter, Debye-Waller factor in $He \to Cu(001)$ collisions revisited: the role of the interaction potentials, Surf.Sci. 385, 270-280 (1997)
- 2. J. Braun, D. Fuhrmann, A. Šiber, B. Gumhalter, and Ch. Wöll, Observation of a zone-center gap in the longitudinal mode of an adsorbate overlayer: Xenon on Cu(111), Phys. Rev. Lett. 80, 125-128 (1998)
- 3. A.Šiber and B. Gumhalter, Comment on "Quantum scattering of heavy particles from a 10 K Cu(111) surface", Phys. Rev. Lett. 81, 1742 (1998)
- 4. A. Šiber, B. Gumhalter, J. Braun, A.P. Graham, M. Bertino, J.P. Toennies, D. Fuhrmann and Ch. Wöll, Combined He-atom scattering and theoretical study of the low-energy vibrations of physisorbed monolayers of Xe on Cu(111) and Cu(001), Phys. Rev. B 59, 5898 (1999)
- 5. A. Siber, B. Gumhalter and J.P. Toennies, Study of energy transfer in helium atom scattering from surfaces, Vacuum **54**, 315 (1999)
- 6. B. Gumhalter, A. Šiber and J.P. Toennies, Recovery temperature for nonclassical energy transfer in atom-surface scattering, Phys. Rev. Lett. 83, 1375 (1999)
- 7. T. Valla, M. Kralj, A. Šiber, M. Milun, P. Pervan, P.D. Johnson and D.P. Woodruff, Oscillatory electron-phonon coupling in ultrathin silver films on V(100), J. Phys.: Condens. Matter 12, L477 (2000)

- 8. Antonio Šiber, Branko Gumhalter, Andrew. P. Graham and J. Peter Toennies, He atom scattering and theoretical study of the surface phonons of a simple benchmark system: Xe(111), Phys. Rev. B 63, 115411 (2001)
- 9. M. Kralj, A. Šiber, P. Pervan, M. Milun, T. Valla, P. D. Johnson, and D. P. Woodruff, Temperature dependence of photoemission from quantum-well states in Ag/V(100): Moving surface-vacuum barrier effect, Phys. Rev. B 64, 085411 (2001)
- 10. Antonio Siber and Branko Gumhalter, Zone edge focused twophonon processes in He atom scattering from a simple prototype system: Xe(111), Surf. Sci. **502-503**, 422 (2002)
- 11. Antonio Šiber, Branko Gumhalter and Christof Wöll, Kinematic effects in the Debye-Waller factor and sticking probabilities in low-energy atom-surface scattering, J. Phys.: Condens. Matter, 14, 5913 (2002)
- 12. Antonio Šiber and Hrvoje Buljan, Quantum states and specific heat of low-density He gas adsorbed within the carbon nanotube interstitial channels: Band structure effects and potential dependence, Phys. Rev. B, prihvaćeno za objavljivanje (2002), code BS8268

Index

band, 22, 40, 108–111 charge transfer, 39, 40, 43, 57, classical, 16, 34, 76, 103, 105, 106 density, 6, 14, 15, 36, 37, 39, 40, 42-44, 48, 56-58, 61, 63, 66, 67, 71, 74, 90, 96, 97, 106 effective mass, 109 exclamation mark, 109 gas phase, 3, 9, 28–30, 36, 39, 42, 43, 48, 49, 54, 67, 71,76, 77, 92, 93, 96 gaussian, 34, 51, 58, 69, 80, 97 inelastic, 2, 6, 8, 21, 44, 45, 54, 55, 61, 88, 96, 105, 106 interference, 4, 23–26, 72 Jacobian, 79 multiphonon, 54, 96 multipole, 29, 30, 41, 44 neighbor, 61, 63, 90 quantum number, 6, 12 redistribution, 3, 39

sensitivity, 2, 3, 25, 55, 63, 72,

90, 105

sticking, 8 time, 6, 8, 9, 26, 36, 44, 51, 83, 87, 104, 105 trajectory, 103–106 turning point, 16, 23, 34, 76, 104, 106 unitarity, 8, 21, 79